NAG1-343

CCMS-87-17
VPI-E-87-32

IN-39-CR
190060
P-193

VIRGINIA TECH

CENTER FOR COMPOSITE MATERIALS AND STRUCTURES

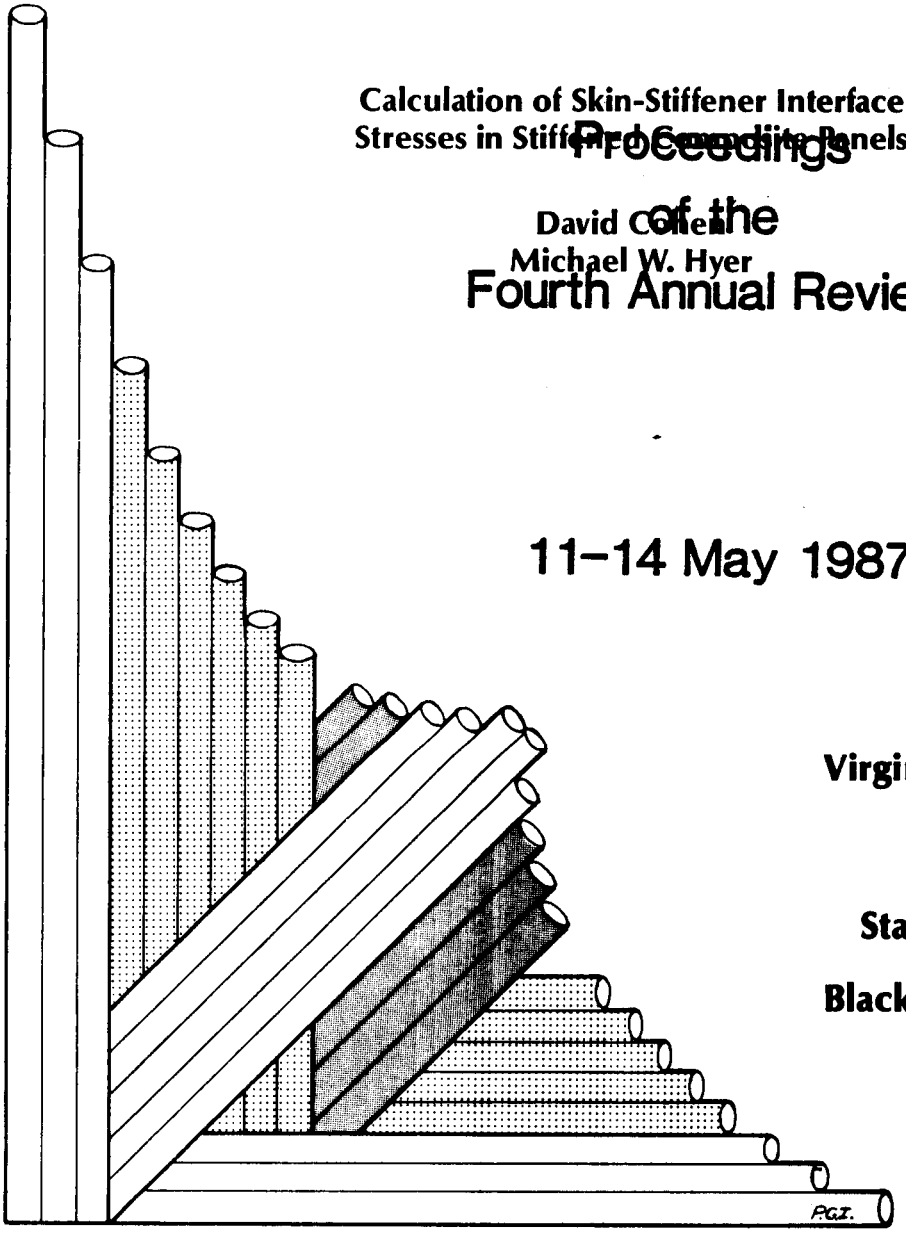

Calculation of Skin-Stiffener Interface Stresses in Stiffened Composite Panels

Proceedings

of the

Fourth Annual Review

David Cohen
Michael W. Hyer

11–14 May 1987

Virginia Polytechnic Institute and State University

Blacksburg, Virginia 24061

(NASA-CR-184682) CALCULATION OF SKIN-STIFFENER INTERFACE STRESSES IN STIFFENED COMPOSITE PANELS Interim Report (Virginia Polytechnic Inst. and State Univ.) 193 p

N89-17899

Unclas
CSCL 20K G3/39 0190060

College of Engineering
Virginia Polytechnic Institute and State University
Blacksburg, Virginia 24061

December 1987

CCMS-87-17
VPI-E-87-32

Calculation of Skin-Stiffener Interface Stresses in Stiffened Composite Panels

David Cohen[1]
Michael W. Hyer[2]

Department of Engineering Science and Mechanics

Interim Report 68
The NASA-Virginia Tech Composites Program
NASA Grant NAG-1-343

Prepared for: Structural Mechanics Branch
National Aeronautics and Space Administration
Langley Research Center
Hampton, Virginia 23665

---

[1] Graduate Student, Department of Engineering Science and Mechanics, Virginia Polytechnic Institute and State University

[2] Professor, Department of Engineering Science and Mechanics, Virginia Polytechnic Institute and State University

CALCULATION OF SKIN-STIFFENER INTERFACE STRESSES IN STIFFENED COMPOSITE PANELS

(ABSTRACT)

A method for computing the skin-stiffener interface stresses in stiffened composite panels is developed. Both geometrically linear and nonlinear analyses are considered. Particular attention is given to the flange termination region where stresses are expected to exhibit unbounded characteristics. The method is based on a finite-element analysis and an elasticity solution. The finite-element analysis is standard, while the elasticity solution is based on an eigenvalue expansion of the stress functions. The eigenvalue expansion is assumed to be valid in the local flange termination region and is coupled with the finite-element analysis using collocation of stresses on the local region boundaries. In the first part of the investigation the accuracy and convergence of the local elasticity solution are assessed using a geometrically linear analysis. It is found that the finite-element/local elasticity solution scheme produces a very accurate interface stress representation in the local flange termination region. The use of 10 to 15 eigenvalues, in the eigenvalue expansion series, and 100 collocation points results in a converged local elasticity solution. In the second part of the investigation, the local elasticity solution is extended to include geometric nonlinearities. Using this analysis procedure, the influence of geometric nonlinearities on skin-stiffener interface stresses is evaluated. It is found that in flexible stiffened skin structures, which exhibit out-of-plane deformation on the order of 2 to 4 times the skin thickness, inclusion of geometrically nonlinear effects in the calculation of interface stresses is very important. Thus, the use of a geometrically linear analysis, rather than a nonlinear analysis, can lead to considerable error in the computation of the interface stresses. Finally, using the analytical tool developed in this investigation, it is possible to study the influence of stiffener parameters on the state of interface stresses.

Acknowledgements

This study was supported by the NASA-Virginia Tech Composites Program under the NASA Contract Grant NAG 1-343. We would like to acknowledge, in particular, Drs. J. H. Starnes, Jr. and M. P. Nemeth for their useful contributions and support of this project.

Table of Contents

List of Illustrations

List of Tables

1. Introduction

In recent years there has been a dramatic increase in the use of composite materials in aircraft structures. Compared to metallic structures, the cost benefits, performance increase, and weight reductions which can be realized are substantial. As with metallic structures, one of the primary components in aircraft structures is the skin-stiffener combination. In traditional metallic structures the stiffener is attached to the skin by rivets. In severe loading conditions, such as those that occur during postbuckling, the rivets provide a site for yielding of the metal. As a result, failure in the form of local yielding may occur but the failure does not necessarily cripple the structure as a whole. On the other hand, composite materials are brittle and do not yield. Holes and other geometric discontinuities are sites for high stresses that ultimately cause the failure of the structure as a whole. Therefore, the use of rivets as the method of stiffener attachment is less attractive with composites than it has been with metals. A more common method of stiffener-to-skin attachment in composite structures is by an adhesive secondary bonding or by the cocuring of the stiffener and skin.

Because of the differences in material properties and the lack of riveting, the failure characteristics observed with bonded or cocured stiffened composite skins are quite different from the failures encountered in riveted metallic structures. Failure in stiffened composite skins occurs in a much more catastrophic manner, being initiated by skin-stiffener separation [1].

Further, it has been shown [2] that stiffened composite panels can fail prematurely, below the design load, due to skin-stiffener separation. One such mode of failure has been observed to initiate at the flange termination region. Figure 1 illustrates an example of this type of failure. Because of observations such as shown in Figure 1, it is believed that the stresses in the flange termination region are high. High skin-stiffener interface stresses can be attributed to a number of factors. First, there is the structural incompatibility associated with the deformation of the skin and deformation of the stiffener when the skin-stiffener combination is subjected to applied loads. This incompatibility is particularly acute in the postbuckling state. In addition, if the stiffener is bonded to the skin, the flange termination region leads to a geometric discontinuity in the structure. This region tends to serve as an area of increased stress. Finally, in stiffened composite skins the problem is compounded by an additional complication. In order to gain full advantage of the tailoribility of composite materials, generally the stiffener and the skin are constructed of different material layups. Such material discontinuity at the interface can lead to significant skin-stiffener interface stresses. It is the primary purpose of the present study to develop a method by which the stresses in this region can be accurately determined, and to use the method to investigate the influence of various stiffener parameters on the stresses in this region. Though the flange termination region is of primary concern, stresses at all locations along the interface are computed.

To predict the skin-stiffener interface stresses, different levels of analytic complexity can be used. However, it is generally acknowledged that the analytical model should incorporate a few key features. First, the model should accurately represent the geometric and material discontinuities associated with the flange termination. As with free edge stresses, these geometric and material discontinuities can cause the stresses in the flange termination region to be unbounded. When present, these unbounded stresses can be responsible for the initiation of skin-stiffener separation and should be accounted for. Secondly, since stiffened panels are most commonly designed to operate at the postbuckling range, the analysis must incorporate geometrically nonlinear effects. Third, for the analytic tool to be useful in the design

ORIGINAL PAGE
BLACK AND WHITE PHOTOGRAPH

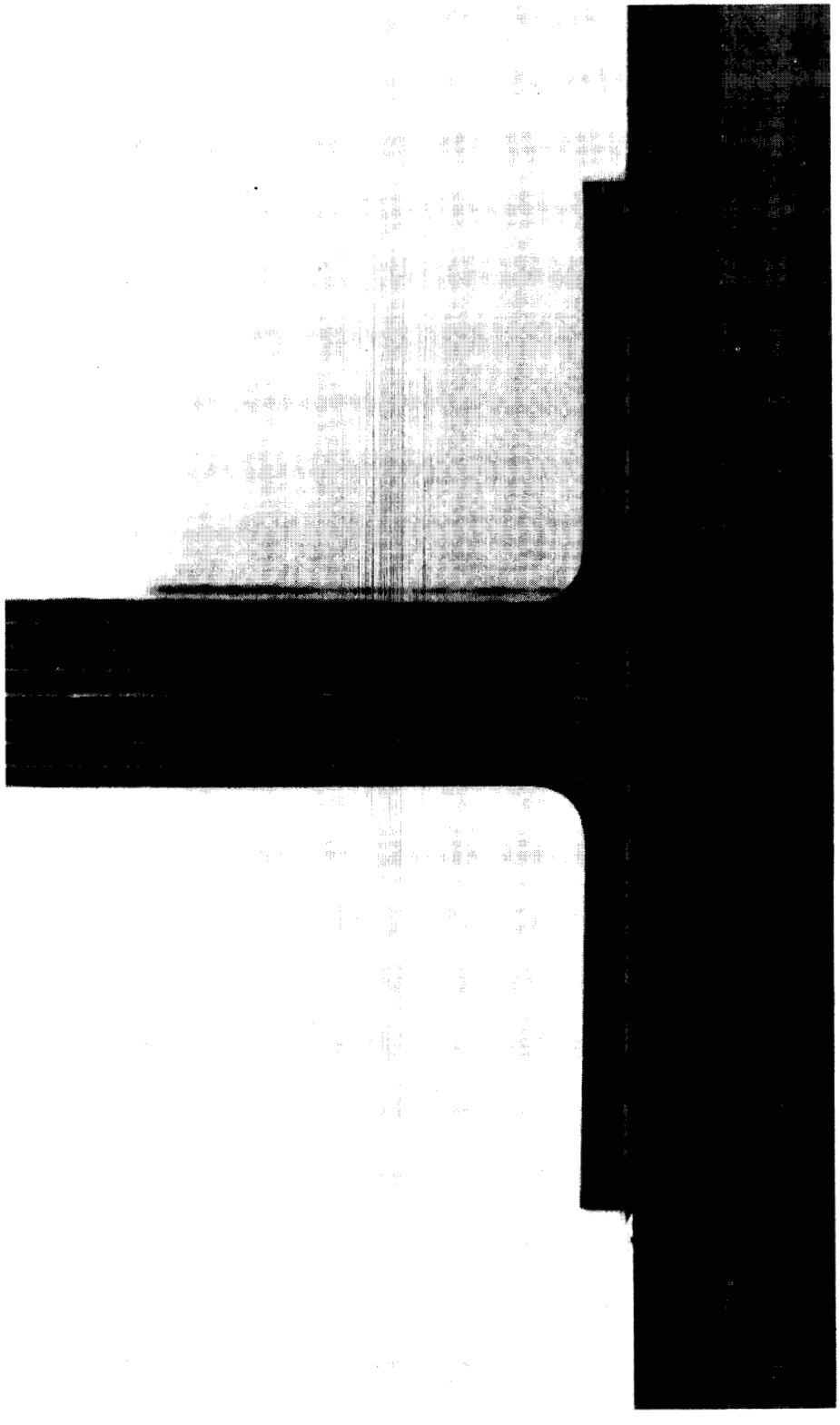

Figure 1. Skin-Stiffener Separation Initiation at the Flange Termination Region.

process, it must be sensitive enough to various design parameters, e.g., stiffener geometry and skin/stiffener material architecture. In addition to these three key factors, there is the issue of computational efficiency or cost. The computational cost should not be so large as to prohibit its use as a tool for parametric studies or for the design of a stiffened structure. And finally, the analysis should be such that it can be integrated into any proposed computational schemes or testbeds [3,4].

Considering the severity of the problem, there have been few studies of skin-stiffener interface stresses. One of the more notable ones is discussed in [5]. In this investigation the skin and flange were treated as separate orthotropic plate elements. These elements were held together via interface forces, the forces being taken as unknowns. The stiffness of the other stiffener elements, such as the web and the cap, were treated as extensional and rotational springs. The solution to the problem was formulated using the principle of virtual work and the theorem of minimum potential energy. Although in the postbuckling range the skin will actually experience moderate to large rotations, the analysis assumed only geometric linear deformation theory. Other studies [6-9] have considered similar problems, namely the adhesively bonded lap joints. In these studies the two adherents were treated as plates under cylindrical bending and/or inplane loads. In [6-8] the adhesive was modeled as shear spring only or tension-shear spring combination, and in [9] it was treated as an elastic layer in which the stresses did not vary across the adhesive thickness. In all of these studies a solution for the variation of shearing and peeling stresses in the adhesive was obtained. In [9] the derived solution was also applied to a simplified stiffened composite plate geometry. These investigations looked at simplified geometries and loading conditions. Hence, although these studies are important in furthering the understanding of adhesively bonded components, they cannot be applied in their present form to the study of stiffened composite aircraft structures. This is due to the fact that such structures tend to have complex geometries and loading conditions. In addition, the above studies did not address the issue of geometric nonlinearities.

Due to the problems in the previous analytical models discussed above, a more detailed analysis was undertaken. As stated above, and reiterated here, the following key requirements were imposed: a) The model should accurately represent the state of stress near the point of geometric and material discontinuity; b) The model should be applicable to the geometric nonlinear range; and c) The model should be sensitive in its stress prediction to various design parameters, such as stiffener geometry and stiffener/skin material architecture. To meet these requirements, an analysis is developed in which the stress predictions are based on a generalized plane deformation elasticity solution in combination with standard finite-element calculations. The elasticity solution is valid in the localized region near the termination of the stiffener flange. The finite-element calculations are valid for the structure as a whole, except near the flange termination region. The elasticity solution uses an eigenvalue expansion of the stress function to predict the stresses. The expansion is applicable in the flange termination region and satisfies exactly the boundary conditions there. The eigenvalue expansion is known to within arbitrary, but unknown, coefficients which are associated with each eigenvalue. The stresses from the finite-element solution and collocation scheme are used for determining the constants and thus uniquely determining the stresses in the localized region.

In the next chapters various aspects of the investigation will be discussed. In chapter 2 the development of the analytical method and its verification are delineated. The derivations in this chapter are for geometrically linear analysis only. In chapter 3 it is shown how the methodology developed in chapter 2 may be extended to include geometric nonlinearities (i.e., moderate rotations). This is followed by a discussion of the application of this extension to the study of interface stresses in stiffened composite plates. In chapter 4, numerical results are presented. These results highlight the effect of including geometric nonlinearities in the analysis on skin-stiffener interface stresses. In addition, the effect of various stiffener geometric and material parameters are evaluated. The study ends with some concluding remarks and recommendations for future research.

2. Analytical Method Development

2.1 Analysis Overview and Relevant Literature

To facilitate the following discussion, a skin-stiffener cross-section being studied is shown in Figure 2. Note the location of the coordinate system in the figure and the nomenclature associated with the cross-section. Several coordinate systems will be used hereafter and it will be important to differentiate between them. Interest focuses on the computation of interface stresses at the skin-stiffener interface, along the line $y=0$. The type of stiffener shown, a blade stiffener, is only to serve as an example. Other stiffener types such as hat, I, and J can be studied with the type of analysis being developed. It should be noted that the flange can terminate at various angles, α_1 (see Figure 2), relative to the skin. The shaded area, shown in the exploded view, is referred to as the local region. This is the region where the elasticity solution is valid. The region outside of the shaded area, referred to as the global region, is the region where the finite-element solution is valid. It will be assumed that Figure 2 represents a cross-section of a stiffened panel that is long enough that the stress state does not vary in the stiffener direction in the region of interest. That is, in the nomenclature of the figure, the stresses do not vary with the z coordinate.

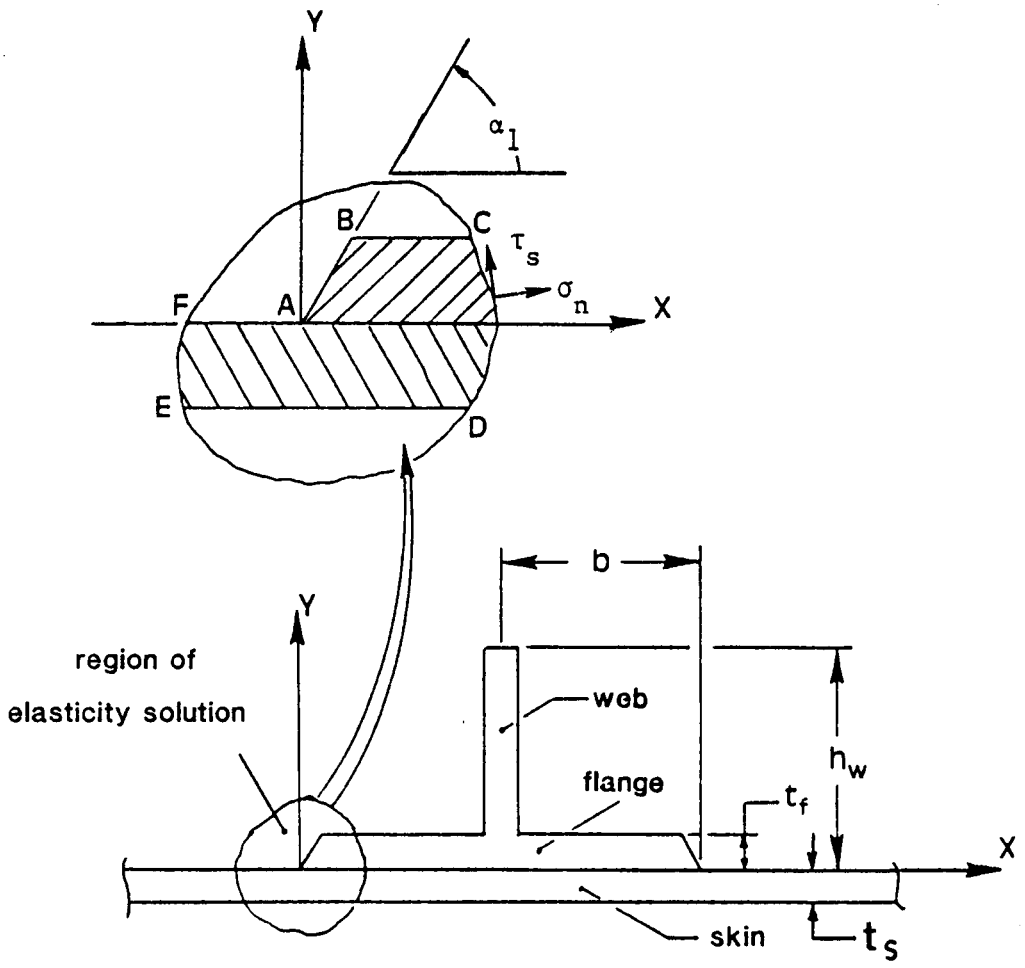

+z axis out of page

Figure 2. Skin-Stiffener Cross-Section Geometry.

A linear analysis of the local region, as depicted in Figure 3, consists of finding the solution to the equations of elasticity valid in a region enclosed by an arbitrary corner opening created by two dissimilar orthotropic materials bonded along $y=0$, and subjected to known boundary conditions. The literature regarding this problem is extensive and no attempt is made to cover all of it, instead some of the more important studies directly relevant to our investigation will be discussed. Williams [11] was the first to investigate the solution to an arbitrary corner in an isotropic plate in the form of an eigenfunction expansion. His solution was used extensively by Gross et al [12-16] in the numerical computations of stress intensity factors of various fracture toughness specimens. Carpenter [17] used Muskhelishvili's [18] complex potential approach to solve the same problem. He applied his solution to the investigation of interface stresses in lap joints. Williams, in a later paper [19], extended his solution to wedges composed of two dissimilar isotropic materials. Bogy [20] solved the same problem using Mellin transforms and obtained similar results. The extension of the above problem to wedges composed of two dissimilar anisotropic materials was first conducted by Wang and Choi [21]. In their work they used the complex eigenfunction expansion of the Lekhnitskii [22] stress functions. Later they applied their solution to laminate free-edge problems [23] and composite lap joints [24]. Other investigators solved the same problem using slightly different approaches. Delale [25] transformed Lekhnitskii stress functions into polar coordinates and used a polar eigenfunction expansion, in real variables, to solve the problem. Ting and Chou [26] and Bogy [27] used the Green and Zerna complex function representation to solve the same problems.

In the present study the solution method outlined by Lekhnitskii [22] and the specific eigenfunction expansion solution proposed by Wang and Choi [21] is employed. Inherent in this solution method is the need to determine a set of coefficients, one coefficient being associated with each eigenfunction, from the boundary conditions. Among the many methods available by which the unknown coefficients may be determined, a collocation technique was chosen here. The method involves the use of n boundary conditions, of known magnitude,

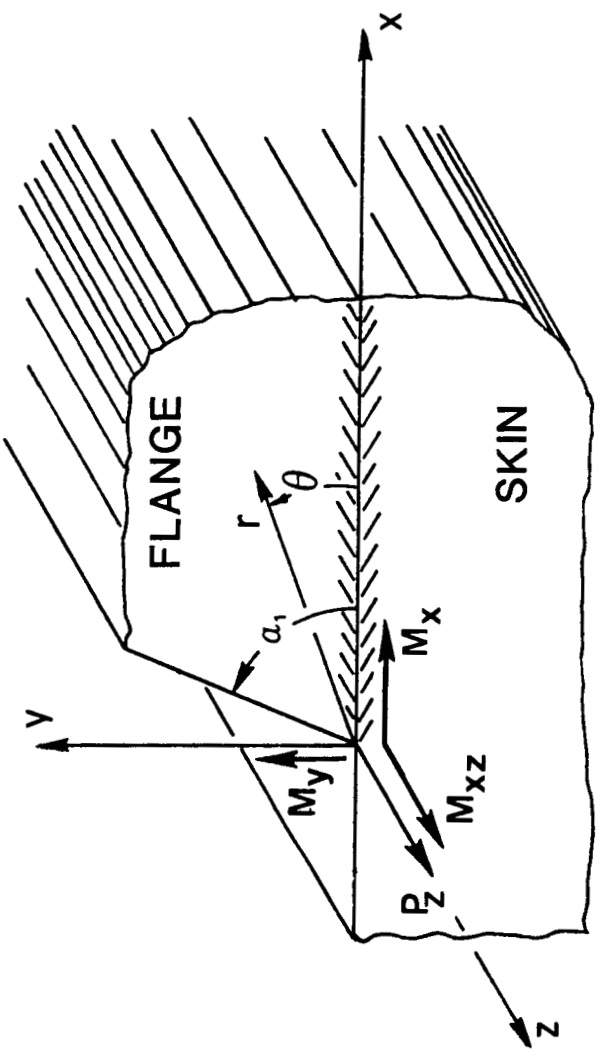

Figure 3. Elasticity Solution Body Geometry.

matched along prescribed boundaries with the same boundary quantities written in terms of the unknown coefficients. This leads to a system of n simultaneous equations from which the n unknown coefficients can be determined. The above procedure is sometime referred to as the point-matching method. Since there is no rigorous proof for convergence of the collocation method, it is typically studied by increasing the number of terms in the assumed function and the number of boundary collocation points. To increase accuracy and decrease dependency in the manner in which the positions of the collocation points are chosen, it is common practice to use more boundary collocation points than unknown coefficients [28,29]. This approach is known as the overdetermined collocation procedure. Since it leads to an overdetermined set of equations by which the unknown coefficients are evaluated, the coefficients are determined in a least-squares sense. Once it is clear that the number of terms in the assumed function and the number and location of the known boundary points have little influence on the numerical results, it is assumed that the procedure has converged. The converged functions are then assumed to be close to a true representation of the exact solution within this region.

A number of investigators have made extensive use of the above described collocation procedure. Gross et al [12-16] used boundary collocation in the determination of K_I for various edge crack specimen geometries. In their investigation the first coefficient (which is related to K_I) of the Williams stress function, χ, was determined by collocating boundary vales of χ and $\frac{\partial \chi}{\partial n}$ (n being the normal to the boundary) along prescribed boundaries. Carpenter [28] applied boundary collocation in the determination of various fracture parameters. The unknown coefficients of the truncated function expansion were evaluated from the collocation of all three stress components (σ_x, σ_y and τ_{xy}) obtained from finite-element analysis. In another paper [30] Carpenter investigated accuracy issues related to the boundary collocation of stresses and/or displacements. Wang and Choi [23] used collocation to study the laminate free-edge problem.

Other procedures which involve the use of eigenfunction expansion of the stress function in a localized region include the reciprocal work contour integral (RWCI) method, and the use

of special singular elements. The RWCI is based on Betti's theorem of elastic bodies. Two sets of forces (S_j and S'_j) and displacements (u_j and u'_j) of the same direction but not the same magnitude acting at selected points along the body boundary are in reciprocal equilibrium. Use of the theorem provides a scheme by which the boundary value problem discussed previously may be solved. In addition, the RWCI leads to a path-independent procedure. The above technique have been used in the computation of K_I and/or K_{II} by Carpenter [17] and Sinclair et al [31]. In the singular or hybrid element formulation, a special element is developed which comprises a portion of the localized region where geometric and material discontinuities occur. The displacements and stresses within the element boundary are governed by the exact elasticity solution. The surrounding standard elements of the mesh are then connected at n nodal points along the boundary of the special element. The coefficients of the truncated stress function are then determined so as to render continuity (or compatibility) of the nodal displacements at the special element's boundary in an exact or approximate manner. There are numerous studies which have utilized the above concept. Some of the more relevant ones include work by Wang and Yuan [32] and Jones and Callinan [33].

Clearly, the issue here is determining the conditions on the boundary of the local region. In general, it is not important how the boundary conditions are obtained, as long as the information is accurate. For complex geometries, such as the skin-stiffener cross-section, the only reasonable method to obtain boundary conditions is with finite-element analysis. Thus the method here will utilized a finite-element analysis of the cross-section to provide stress information on the boundary of the localized region. Furthermore, the finite-element analysis of the cross-section itself will be coupled to a finite-element analysis of the entire plate. The total analysis will be of the form of a structure-substructure-local analysis. The remainder of this chapter will be devoted to the local analysis. The governing equations of elasticity, the eigenvalue expansion solution, and the application of the collocation procedure will be presented. In addition, the accuracy and convergence of the method are discussed by application to specific problems.

2.2 Material model

The analysis here is implemented on the laminate rather than a lamina level. That is, the skin and stiffener are treated as having homogeneous integrated material properties. The reason behind this is as follows: It is felt that the interaction between the skin and the stiffener are controlled more by the overall stiffnesses of the skin and the stiffener than by the stiffness of the individual lamina at the skin-stiffener interface. For this reason the integrated material properties are used in the present analysis. Furthermore, only symmetric balance laminates are considered. In obtaining integrated material properties, the lamina principal material co-ordinates, denoted as the 1-2-3 coordinates, correspond to the transverse, thickness, and fiber directions, respectively. The x-y-z coordinates correspond to directions transverse, normal, and colinear to the stiffener, respectively (see Figure 2). The fiber angle, φ, measures the angle between the 3 and z axis, a positive rotation corresponding to rotation of the fiber from the z axis toward the x axis.

The well known laminate constitutive relations in the 1-2-3 system are written symbolically as,

$$\vec{\varepsilon}_1 = S\,\vec{\sigma}_1 \quad , \qquad [1]$$

$\vec{\varepsilon}_1$ and $\vec{\sigma}_1$ being the strain and stress vectors in the 1-2-3 system and S being the compliance matrix in the same system. The transformation of stress and strain from the 1-2-3 system to the x-y-z system leads to,

$$\vec{\sigma}_1 = T_1\,\vec{\sigma}_x \quad , \qquad [2.a]$$

$$\vec{\varepsilon}_1 = T_2\,\vec{\varepsilon}_x \quad , \qquad [2.b]$$

where T_1 and T_2 are the transformation matrices for stress and strain respectively. For a discussion of these transformations see Appendix A. Substitution of eqs. 2 into eq. 1 leads to the lamina constitutive relations in the x-y-z system, namely;

$$\vec{\varepsilon}_x = \bar{S}\,\vec{\sigma}_x \quad , \qquad [3.a]$$

where,

$$[\bar{S}] = T_2^{-1}[S]T_1 = \begin{bmatrix} \bar{S}_{11} & \bar{S}_{12} & \bar{S}_{13} & 0 & \bar{S}_{15} & 0 \\ \bar{S}_{21} & \bar{S}_{22} & \bar{S}_{23} & 0 & \bar{S}_{25} & 0 \\ \bar{S}_{31} & \bar{S}_{32} & \bar{S}_{33} & 0 & \bar{S}_{35} & 0 \\ 0 & 0 & 0 & \bar{S}_{44} & 0 & \bar{S}_{46} \\ \bar{S}_{51} & \bar{S}_{52} & \bar{S}_{53} & 0 & \bar{S}_{55} & 0 \\ 0 & 0 & 0 & \bar{S}_{64} & 0 & \bar{S}_{66} \end{bmatrix} , \qquad [3.b]$$

and $\bar{S}_{ji} = \bar{S}_{ij}$. In inverted form eq. 3.a is written as,

$$\vec{\sigma}_x = \bar{C}\,\vec{\varepsilon}_x \quad . \qquad [4]$$

The integrated laminate properties are obtained by smearing the individual lamina properties throughout the thickness of the laminate. This is achieved by defining an average stress through the laminate thickness, h, i.e.,

$$\vec{\bar{\sigma}}_x = \frac{1}{h}\int_{-1/h}^{1/h} \vec{\sigma}_x \, dy \quad . \qquad [5]$$

Substitution of eq. 4 into eq. 5 leads to the laminate constitutive relations:

$$\begin{Bmatrix} \sigma_x \\ \sigma_y \\ \sigma_z \\ \tau_{yz} \\ \tau_{xz} \\ \tau_{xy} \end{Bmatrix} = \begin{bmatrix} A_{11} & A_{12} & A_{13} & 0 & 0 & 0 \\ A_{12} & A_{22} & A_{23} & 0 & 0 & 0 \\ A_{13} & A_{23} & A_{33} & 0 & 0 & 0 \\ 0 & 0 & 0 & A_{44} & 0 & 0 \\ 0 & 0 & 0 & 0 & A_{55} & 0 \\ 0 & 0 & 0 & 0 & 0 & A_{66} \end{bmatrix} \begin{Bmatrix} \varepsilon_x \\ \varepsilon_y \\ \varepsilon_z \\ \gamma_{yz} \\ \gamma_{xz} \\ \gamma_{xy} \end{Bmatrix} , \qquad [6.a]$$

where the overbar is dropped from the stresses for convenience. The laminate stiffness components A_{ij} are given by,

$$A_{ij} = \frac{1}{h} \sum_{k=1}^{n} \bar{C}_{ij} \, (y_k - y_{k-1}) \ , \qquad [6.b]$$

n being the number of laminae and y_k and y_{k-1} being defined as the through-the-thickness locations of the laminae interfaces. In inverted form;

$$\vec{\varepsilon}_x = [a] \, \vec{\sigma}_x \ . \qquad [7]$$

It should be noted that although each lamina is considered to be anisotropic in the x-y-z system, the laminate constitutive law is that of an orthotropic material, i.e., the smeared laminate properties are orthotropic.

2.3 Elasticity Solution

As mentioned at the outset, the analysis will be developed for the linear case and then extended to the geometrically nonlinear analysis case. What follows is the linear analysis development.

2.3.1 Development of the Stress Functions

Consider an arbitrary semi-infinite corner composed of two dissimilar orthotropic materials bonded along $y=0$ (or $\theta = 0$), as depicted in Figure 3. If the body in question obeys the following restrictions: a) The dimension in the z direction is much larger than the cross-sectional dimensions; and b) The external loads on the lateral surface do not vary with z, it is possible that the stresses, and hence the strains, are independent of the z-coordinate. Such a condition is referred to as a generalized plane deformation. The ends of the body may be subjected to axial force, P_z, twist M_{xz}, and moments, both about the x and y axes (i.e., M_x and M_y). If such end loads are present, the state of plane deformation will exist at some distance from the ends in a manner consistent with St. Vernant's principle. Under the above conditions the stress equilibrium equations become,

$$\frac{\partial \sigma_x}{\partial x} + \frac{\partial \tau_{xy}}{\partial y} = 0 , \qquad [8.a]$$

$$\frac{\partial \tau_{xy}}{\partial x} + \frac{\partial \sigma_y}{\partial y} = 0 , \qquad [8.b]$$

$$\frac{\partial \tau_{xz}}{\partial x} + \frac{\partial \tau_{yz}}{\partial y} = 0 . \qquad [8.c]$$

The strain-displacement relations are given by,

$$\varepsilon_x = \frac{\partial u}{\partial x} , \qquad \gamma_{yz} = \frac{\partial w}{\partial y} + \frac{\partial v}{\partial z} , \qquad [9.a,b]$$

$$\varepsilon_y = \frac{\partial v}{\partial y} , \qquad \gamma_{xz} = \frac{\partial w}{\partial x} + \frac{\partial u}{\partial z} , \qquad [9.c,d]$$

$$\varepsilon_z = \frac{\partial w}{\partial z} , \qquad \gamma_{xy} = \frac{\partial u}{\partial y} + \frac{\partial v}{\partial x} , \qquad [9.e,f]$$

where the strains are a function of x and y only. The constitutive relations of eq. 7 for a homogenous orthotropic body under consideration can be written in full as,

$$\begin{Bmatrix} \varepsilon_x \\ \varepsilon_y \\ \varepsilon_z \\ \gamma_{yz} \\ \gamma_{xz} \\ \gamma_{xy} \end{Bmatrix} = \begin{bmatrix} a_{11} & a_{12} & a_{13} & 0 & 0 & 0 \\ a_{12} & a_{22} & a_{23} & 0 & 0 & 0 \\ a_{13} & a_{23} & a_{33} & 0 & 0 & 0 \\ 0 & 0 & 0 & a_{44} & 0 & 0 \\ 0 & 0 & 0 & 0 & a_{55} & 0 \\ 0 & 0 & 0 & 0 & 0 & a_{66} \end{bmatrix} \begin{Bmatrix} \sigma_x \\ \sigma_y \\ \sigma_z \\ \tau_{yz} \\ \tau_{xz} \\ \tau_{xy} \end{Bmatrix} . \qquad [10]$$

The general expressions for the displacement functions are obtained by a series of integrations and differentiations of eqs. 8, 9, and 10. The step-by-step details are given in [22]. In general, the constitutive relations are written in terms of the displacements using eqs. 9. The integration of three of these equations, (keeping in mind that $\vec{\sigma}_x$ is independent of z) and the satisfaction of the remaining three equations leads to the displacement functions in the general form,

$$u = -\frac{B_1 a_{33}}{2} z^2 - B_4 y z + U(x,y) + \omega_2 z - \omega_3 y + u_o , \qquad [11.a]$$

$$v = -\frac{B_2 a_{33}}{2} z^2 + B_4 x z + V(x,y) + \omega_3 x - \omega_1 z + v_o , \qquad [11.b]$$

$$w = (B_1 x + B_2 y + B_3) a_{33} z + W(x,y) + \omega_1 y - \omega_2 x + w_o , \qquad [11.c]$$

where B_i, $(i = 1,2,3,4)$, are arbitrary constants of integration, ω_i, $(i = 1,2,3)$ are rigid body rotations, and u_o, v_o and w_o are rigid body translations. The unknown functions U(x,y), V(x,y) and W(x,y) must satisfy the following conditions:

$$\frac{\partial U}{\partial x} = \beta_{11}\sigma_x + \beta_{12}\sigma_y + a_{13}(B_1 x + B_2 y + B_3) , \qquad [12.a]$$

$$\frac{\partial V}{\partial y} = \beta_{21}\sigma_x + \beta_{22}\sigma_y + a_{23}(B_1 x + B_2 y + B_3) , \qquad [12.b]$$

$$\frac{\partial U}{\partial y} + \frac{\partial V}{\partial x} = \beta_{66}\tau_{xy} , \qquad [12.c]$$

$$\frac{\partial W}{\partial x} = \beta_{55}\tau_{xz} + B_4 y , \qquad [12.d]$$

$$\frac{\partial W}{\partial y} = \beta_{44}\tau_{yz} - B_4 x , \qquad [12.e]$$

where β_{ij} are the reduced stiffness coefficients and are given by,

$$\beta_{ij} = a_{ij} - \frac{a_{i3}\,a_{j3}}{a_{33}} , \quad i,j = 1, 2, 4, 5, 6 . \qquad [13]$$

The compatibility equations are satisfied identically for the above displacement field since it is derived from the strain-displacement relations. In addition it can be shown [22] that,

$$\sigma_z = B_1 x + B_2 y + B_3 - \frac{1}{a_{33}}(a_{13}\sigma_x + a_{23}\sigma_y) . \qquad [14]$$

The stresses which satisfy all the aforementioned assumptions can be derived from two stress functions, F(x,y) and Ψ(x,y) . If the stresses are written in terms of these functions as,

$$\sigma_x = \frac{\partial^2 F}{\partial y^2} , \quad \sigma_y = \frac{\partial^2 F}{\partial x^2} , \quad \tau_{xy} = - \frac{\partial^2 F}{\partial x \partial y} , \qquad [15.a,b,c]$$

$$\tau_{yz} = - \frac{\partial^2 \Psi}{\partial x^2} , \quad \tau_{xz} = \frac{\partial^2 \Psi}{\partial y^2} , \qquad [15.d,e]$$

then the stress equilibrium eqs. 8.a through 8.c are satisfied identically. The equations governing F(x,y) and Ψ(x,y) are obtained by substitution of the above stress relations into eqs. 12.a through 12.e and the elimination of U, V, and W by differentiation. For an orthotropic material these equations become,

$$\beta_{22}\frac{\partial^4 F}{\partial x^4} + (2\beta_{12} + \beta_{66})\frac{\partial^4 F}{\partial x^2 \partial y^2} + \beta_{11}\frac{\partial^4 F}{\partial y^4} = 0 , \qquad [16.a]$$

$$\beta_{44}\frac{\partial^2 \Psi}{\partial x^2} + \beta_{55}\frac{\partial^2 \Psi}{\partial y^2} = -2B_4 . \qquad [16.b]$$

The decoupling of the two equations is a distinct characteristic of orthotropic materials (i.e., the equations are not uncoupled for anisotropic material). The equation governing F is homogeneous while the equation for Ψ involves a particular solution. The solution for F and the homogeneous equation for Ψ have the form [22],

$$F = F(x + \mu y) , \qquad [17.a]$$

$$\Psi = \Psi(x + \upsilon y) , \qquad [17.b]$$

where μ and υ are parameters to be determined. For the local region near the vertex of the bimaterial corner the solutions for F(x,y) and Ψ(x,y) are approximated in [21] as,

$$F(Z) = C\frac{Z^{\lambda+2}}{(\lambda+1)(\lambda+2)} , \qquad [18.a]$$

$$\Psi(\tilde{Z}) = D\frac{\tilde{Z}^{(\delta+1)}}{(\delta+1)} , \qquad [18.b]$$

where,

$$Z = x + \mu y , \qquad [19.a]$$

$$\tilde{Z} = x + \upsilon y , \qquad [19.b]$$

and C and D are arbitrary constants. The substitution of F(x,y) and Ψ (x,y) into eqs. 16.a and 16.b leads to,

$$C\,\lambda\,(\lambda-1)\,Z^{\lambda-2}\,[\,\beta_{22}\;+\;(2\,\beta_{12}\;+\;\beta_{66})\,\mu^2\;+\;\beta_{11}\,\mu^4\,]\;=\;0\;, \qquad [20.a]$$

$$D\,\delta\,\bar{Z}^{\delta-1}\,(\beta_{44}\;+\;\beta_{55}\,\upsilon^2)\;=\;0\;. \qquad [20.b]$$

The first equation is satisfied under the following conditions:

a) μ has one of four unique values given by the characteristic equation

$$\beta_{22}\;+\;(2\,\beta_{12}\;+\;\beta_{66})\,\mu^2\;+\;\beta_{11}\,\mu^4\;=\;0\;. \qquad [21]$$

Such roots do exist and they are always complex or imaginary (for detailed discussion see ref. 22). Considering these four values of μ , F(x,y) is given by,

$$F^{(e)}(x,y)\;=\;\sum_{k=1}^{4}\,C_k\,\frac{Z_k^{\lambda+2}}{(\lambda+2)(\lambda+1)}\;, \qquad [22]$$

b) μ is arbitrary and,

$$\lambda\;=\;0\;,\;1$$

This leads to

$$F^{(a)}(x,y)\;=\;b_1\,x^3\;+\;b_2\,x^2\,y\;+\;b_3\,x\,y^2\;+\;b_4\,y^3$$

$$+\;b_5\,x^2\;+\;b_6\,x\,y\;+\;b_7\,y^2\;. \qquad [23]$$

The superscripts (e) and (a) designates the eigenvalue expansion and auxiliary solutions, respectively.

The second of eq. 20 is satisfied under the conditions:

a) υ has one of two unique values given by the characteristic equation,

$$\beta_{44} + \upsilon^2 \beta_{55} = 0 . \qquad [24.a]$$

This leads to,

$$\upsilon_{1,2} = \pm i \sqrt{\frac{\beta_{44}}{\beta_{55}}} , \qquad [24.b]$$

from which $\Psi(x,y)$ becomes,

$$\Psi^{(e)}(x,y) = \sum_{k=1}^{2} D_k \frac{\bar{z}_k^{\delta+1}}{(\delta+1)} . \qquad [25]$$

b) υ has an arbitrary value and,

$$\delta = 0 ,$$

leading to,

$$\Psi^{(a)}(x,y) = b_8 x + b_9 y . \qquad [26]$$

Finally the particular solution of eq 16.b is taken as,

$$\Psi^{(p)}(x,y) = b_{10} x^2 + b_{11} y^2 . \qquad [27.a]$$

In the above the C_k and D_k are arbitrary complex constants and b_i, i = 1,...,9 are arbitrary real constants. The constants b_{10} and b_{11} are not completely arbitrary, namely

$$\beta_{44} b_{10} + \beta_{55} b_{11} = -2 B_4 . \qquad [27.b]$$

In addition, λ and δ are unknown parameters at this point. The total solution for the two stress functions is then written as the sum of the component solutions, i.e.,

$$F(x,y) = F^{(e)}(x,y) + F^{(a)}(x,y) , \qquad [28.a]$$

$$\Psi(x,y) = \Psi^{(e)}(x,y) + \Psi^{(a)}(x,y) + \Psi^{(p)}(x,y) \quad . \qquad [28.b]$$

2.3.2 Expressions for the Stresses and Displacements

The Cartesian components of stress are derived from eqs. 15.a through 15.e as,

$$\sigma_x = \sum_{k=1}^{4} C_k \mu_k^2 Z_k^{\lambda} + \sigma_x^{(a)} \quad , \qquad [29.a]$$

$$\sigma_y = \sum_{k=1}^{4} C_k Z_k^{\lambda} + \sigma_y^{(a)} \quad , \qquad [29.b]$$

$$\tau_{xy} = - \sum_{k=1}^{4} C_k \mu_k Z_k^{\lambda} + \tau_{xy}^{(a)} \quad , \qquad [29.c]$$

$$\tau_{yz} = - \sum_{k=1}^{2} D_k \tilde{Z}_k^{\delta} + \tau_{yz}^{(a)} \quad , \qquad [29.d]$$

$$\tau_{xz} = \sum_{k=1}^{2} D_k \upsilon_k \tilde{Z}_k^{\delta} + \tau_{xz}^{(a)} \quad , \qquad [29.e]$$

where the auxiliary stresses are given by:

$$\sigma_x^{(a)} = 2 b_3 x + 6 b_4 y + 2 b_7 \quad , \qquad [30.a]$$

$$\sigma_y^{(a)} = 6 b_1 x + 2 b_2 y + 2 b_5 \quad , \qquad [30.b]$$

$$\tau_{xy}^{(a)} = - 2 b_2 x - 2 b_3 y - b_6 \quad , \qquad [30.c]$$

$$\tau_{yz}^{(a)} = - b_8 - 2 b_{10} x \quad , \qquad [30.d]$$

$$\tau_{xz}^{(a)} = b_9 + 2 b_{11} y \quad . \qquad [30.e]$$

It turns out that it is more convenient to impose conditions on the boundary of the localized region using the polar cylindrical stresses. Using the cylindrical coordinates $r - \theta - z$ (Figure 3), the stress components become,

$$\sigma_r = \sum_{k=1}^{4} C_k r^{\lambda} (m \mu_k - n)^2 (m + n \mu_k)^{\lambda} + \sigma_r^{(a)} , \qquad [31.a]$$

$$\sigma_\theta = \sum_{k=1}^{4} C_k r^{\lambda} (m + n \mu_k)^{(\lambda+2)} + \sigma_\theta^{(a)} , \qquad [31.b]$$

$$\tau_{r\theta} = \sum_{k=1}^{4} C_k r^{\lambda} (m \mu_k - n) (m + n \mu_k)^{(\lambda+1)} + \tau_{r\theta}^{(a)} , \qquad [31.c]$$

$$\tau_{z\theta} = - \sum_{k=1}^{2} D_k r^{\delta} (m + n \upsilon_k)^{(\delta+1)} + \tau_{z\theta}^{(a)} , \qquad [31.d]$$

$$\tau_{rz} = \sum_{k=1}^{2} D_k r^{\delta} (m \upsilon_k - n) (m + n \upsilon_k)^{\delta} + \tau_{rz}^{(a)} . \qquad [31.e]$$

where,

$$\sigma_r^{(a)} = m^2 \sigma_x^{(a)} + 2 m n \tau_{xy}^{(a)} + n^2 \sigma_y^{(a)} , \qquad [32.a]$$

$$\sigma_\theta^{(a)} = n^2 \sigma_x^{(a)} - 2 m n \tau_{xy}^{(a)} + m^2 \sigma_y^{(a)} , \qquad [32.b]$$

$$\tau_{r\theta}^{(a)} = n m (\sigma_y^{(a)} - \sigma_x^{(a)}) + (m^2 - n^2) \tau_{xy}^{(a)} , \qquad [32.c]$$

$$\tau_{z\theta}^{(a)} = - n \tau_{xz}^{(a)} + m \tau_{yz}^{(a)} , \qquad [32.d]$$

$$\tau_{rz}^{(a)} = m \tau_{xz}^{(a)} + n \tau_{yz}^{(a)} . \qquad [32.e]$$

with $m = \cos\theta$ and $n = \sin\theta$.

The general displacement functions u, v and w are given by eqs. 11.a through 11.c. The unknown functions U(x,y), V(x,y) and W(x,y) can now be determined by substitution of the

stresses eqs. 29.a through 29.e into eqs. 12.a through 12.e. Integration of of eqs. 12.a, 12.b and 12.e leads to,

$$U(x,y) = \sum_{k=1}^{4} C_k p_k \frac{Z_k^{\lambda+1}}{(\lambda+1)} + U^{(a)}(x,y) + U_o \ , \qquad [33.a]$$

$$V(x,y) = \sum_{k=1}^{4} C_k q_k \frac{Z_k^{\lambda+1}}{(\lambda+1)} + V^{(a)}(x,y) + V_o \ , \qquad [33.b]$$

$$W(x,y) = \sum_{k=1}^{2} D_k r_k \frac{Z_k^{\delta+1}}{(\delta+1)} + W^{(a)}(x,y) + W_o \ , \qquad [33.c]$$

where,

$$p_k = \beta_{11}\mu_k^2 + \beta_{12} \ , \qquad [34.a]$$

$$q_k = \beta_{12}\mu_k + \frac{\beta_{22}}{\mu_k} \ , \qquad [34.b]$$

$$r_k = -\frac{\beta_{44}}{\upsilon_k} \ , \qquad [34.c]$$

and,

$$U^{(a)}(x,y) = \beta_{11}(b_3 x + 6 b_4 y + 2 b_7) + \beta_{12}(3 b_1 x + 2 b_2 y + 2 b_5)$$

$$+ \frac{a_{13}}{2}(B_1 x + 2 B_2 y + 2 B_3)\, x + g(y) \ , \qquad [35.a]$$

$$V^{(a)}(x,y) = \beta_{12}(2 b_3 x + 3 b_4 y + 2 b_7) + \beta_{22}(6 b_1 x + 2 b_2 y + 2 b_5)$$

$$+ \frac{a_{23}}{2}(2 B_1 x + B_2 y + 2 B_3)\, y + f(x) \ , \qquad [35.b]$$

$$W^{(a)}(x,y) = -[\beta_{44}(b_8 + 2 b_{10} x) + B_4 x]\, y + h(x) \ . \qquad [35.c]$$

In addition, U and V must satisfy eqs. 12.c and W eq. 12.d. This leads to

$$g(y) = [(\beta_{66} - \beta_{12})\, b_3 + 3\,\beta_{22}\, b_1 - \frac{a_{23}}{2} B_1]\, y^2 + U_o \quad , \qquad [35.d]$$

$$f(x) = [(\beta_{66} - \beta_{12})\, b_2 + 3\,\beta_{11}\, b_4 - \frac{a_{13}}{2} B_2]\, x^2 + \beta_{66}\, b_6\, x + V_o \quad , \qquad [35.e]$$

$$h(x) = \beta_{55}\, b_9\, x + W_o \quad . \qquad [35.f]$$

The constants U_o, V_o and W_o may be dropped since they represents rigid body motion, terms which were already included in the general formulation of the displacement functions (see eq. 11).

2.3.3 Application of the Boundary and Interface Conditions

2.3.3.a The Eigenvalue Solution

An examination of Figures 2 and 3 illustrate the conditions that must be applied to the solutions to have the solutions satisfy the conditions of the skin-stiffener interface problems. Specifically referring to Figure 3, the surface represented by $\theta = \alpha_1$ and $\theta = -\pi$ are generally free of any tractions. If pressure-loaded panels are being considered, these surfaces could be exposed to the normal pressure traction. However, the magnitude of this traction relative to the magnitude of the stresses generated within the material is negligible and can be considered zero. Hence, one condition on the analysis is that the surfaces at $\theta = \alpha_1$ and $\theta = -\pi$ are traction free. In addition along the line $\theta = 0$, the stiffener and skin are joined. It is the intent of the joining to provide a condition of no slippage along this line, i.e., the displacements are continuous across the interface. Finally, from stress equilibrium arguments, the stresses σ_y, τ_{xy}, and τ_{yz}, are continuous across the interface. These conditions provide the

necessary equations for determining some of the constants, and hence the characteristic of, $F(Z)$ and $\Psi(\bar{Z})$.

The conditions of traction-free boundaries are represented by (see Figure 3),

$$\sigma_\theta^{(1)}(r, \alpha_1) = \tau_{r\theta}^{(1)}(r, \alpha_1) = \tau_{z\theta}^{(1)}(r, \alpha_1) = 0 \quad , \qquad [36.a]$$

$$\sigma_\theta^{(2)}(r, -\pi) = \tau_{r\theta}^{(2)}(r, -\pi) = \tau_{z\theta}^{(2)}(r, -\pi) = 0 \quad , \qquad [36.b]$$

where the superscripts 1 and 2 designate material 1 (flange) and material 2 (skin) respectively. For a perfect skin-to-flange bond the interface conditions along $\theta = 0$ require,

$$\sigma_\theta^{(1)}(r, 0) = \sigma_\theta^{(2)}(r, 0) \quad , \qquad [37.a]$$

$$\tau_{r\theta}^{(1)}(r, 0) = \tau_{r\theta}^{(2)}(r, 0) \quad , \qquad [37.b]$$

$$\tau_{z\theta}^{(1)}(r, 0) = \tau_{z\theta}^{(2)}(r, 0) \quad , \qquad [37.c]$$

$$u^{(1)}(x, 0) = u^{(2)}(x, 0) \quad , \qquad [37.d]$$

$$v^{(1)}(x, 0) = v^{(2)}(x, 0) \quad , \qquad [37.e]$$

$$w^{(1)}(x, 0) = w^{(2)}(x, 0) \quad . \qquad [37.f]$$

Finally, at the ends of the cross-section (see Figure 3) the following integral conditions are required to be satisfied,

$$\int\int_A \tau_{xz}\, dx\, dy = 0 \quad , \quad \int\int_A \tau_{yz}\, dx\, dy = 0 \quad , \qquad [38.a,b]$$

$$\int\int_A \sigma_z\, dx\, dy = P_z \quad , \quad \int\int_A \sigma_z\, y\, dx\, dy = M_x \quad , \qquad [38.c,d]$$

$$\int\int_A \sigma_z\, x\, dx\, dy = M_y \quad , \quad \int\int_A (\tau_{yz}\, x - \tau_{xz}\, y)\, dx\, dy = M_{xz} \quad . \qquad [38.e,f]$$

It should be noted that as far as the above end conditions are concerned, it is possible to impose kinematic boundary conditions rather than force conditions, or it is possible to impose a mixture of the two. For example, rather than impose the area integral of σ_z over the body's ends to equal P_z, it can be required that $w = e_o z$, e_o being an applied axial strain.

The substitution of stresses, eqs. 31.a through 32.e, and displacements, eqs. 33.a through 35.f, into the traction-free boundary conditions, eqs. 36.a and 36.b, and stress and displacement continuity conditions, eqs. 37.a through 37.f, places certain conditions on the stress functions, F(x,y) and Ψ(x,y). However, following the substitution of stresses and displacements into eqs. 36.a through 37.f and the application of variable separation to the resulting expressions, it is evident that the conditions on the eigenvalue expansion part of the solution separate from the conditions on the auxiliary and particular parts of the solution. Therefore, the conditions on the eigenvalue expansion part of the solution (i.e., $F^{(e)}(x,y)$ and $\psi^{(e)}(x,y)$) are treated separately from the conditions related to the particular and auxiliary part of the total solution (i.e., $F^{(a)}(x,y)$, $\psi^{(a)}(x,y)$ and $\psi^{(p)}(x,y)$). The imposition of traction-free and traction and displacement continuity conditions on $F^{(e)}(x,y)$ and $\psi^{(e)}(x,y)$ leads to the eigenvalue problem associated with δ and λ. Hence these parameters are determined uniquely for each problem. The conditions on $F^{(a)}(x,y)$, $\psi^{(a)}(x,y)$, and $\psi^{(p)}(x,y)$ for the specific skin-stiffener configuration are discussed later, while the conditions on the eigenvalue expansion are discussed next.

The traction-free boundary conditions associated with Ψ(x,y) are given by eqs. 36 as,

$$\tau_{z\theta}^{(1)}(r, \alpha_1) = \tau_{z\theta}^{(2)}(r, -\pi) = 0 \quad , \qquad [39.a]$$

and the traction and displacement continuity conditions by eqs. 37 as,

$$\tau_{z\theta}^{(1)}(r,0) = \tau_{z\theta}^{(2)}(r,0) \quad , \qquad [39.b]$$

$$w^{(1)}(x,0) = w^{(2)}(x,0) \quad . \qquad [39.c]$$

Equations 39.a through 39.c lead to the following relations associated with $\psi^{(e)}(x,y)$:

$$\sum_{k=1}^{2} D_k^{(1)} r^{\delta} (\cos \alpha_1 + \upsilon_k^{(1)} \sin \alpha_1)^{(\delta+1)} = 0 \quad , \qquad [40.a]$$

$$\sum_{k=1}^{2} D_k^{(2)} r^{\delta} (-1)^{(\delta+1)} = 0 \quad , \qquad [40.b]$$

$$\sum_{k=1}^{2} D_k^{(1)} r^{\delta} (1)^{(\delta+1)} = \sum_{k=1}^{2} D_k^{(2)} r^{\delta} (1)^{(\delta+1)} \quad , \qquad [40.c]$$

$$\sum_{k=1}^{2} D_k^{(1)} r_k \frac{x^{(\delta+1)}}{(\delta+1)} = \sum_{k=1}^{2} D_k^{(2)} r_k \frac{x^{(\delta+1)}}{(\delta+1)} \quad , \qquad [40.d]$$

where r_k is defined by eq. 34.c. The above 4 simultaneous set of equations forms the eigenvalue problem for δ. This set of equations can be written symbolically as,

$$[Q (\alpha_1 , \delta)] \vec{D} = 0 \quad . \qquad [41.a]$$

For a nontrivial solution the values of δ are given by,

$$| Q (\alpha_1 , \delta) | = 0 \quad . \qquad [41.b]$$

The eigenvector, $\vec{D}$, consists of the two eigenvectors, $\vec{D}^{(1)}$ and $\vec{D}^{(2)}$, related to materials 1 and 2, respectively, i.e.,

$$\vec{D} = \begin{Bmatrix} \vec{D}^{(1)} \\ \vec{D}^{(2)} \end{Bmatrix} \quad , \qquad [41.c]$$

where both $\vec{D}^{(1)}$ and $\vec{D}^{(2)}$ consist of two constants each.

If δ is complex, solutions occur in complex conjugate pairs of the form,

$$\delta = \gamma \pm i\beta \quad . \qquad [41.d]$$

However, in order that w(x,y) be finite at the origin,

$$-1 < \gamma \quad . \qquad [41.e]$$

The eigenvalue problem for δ is described in greater detail in Appendix B.

The boundary conditions associated with F (x,y) are given by eqs. 36 as

$$\sigma_\theta^{(1)}(r, \alpha_1) = \tau_{r\theta}^{(1)}(r, \alpha_1) = 0 \quad , \qquad [42.a]$$

$$\sigma_\theta^{(2)}(r, -\pi) = \tau_{r\theta}^{(2)}(r, -\pi) = 0 \quad . \qquad [42.b]$$

The traction and displacement continuity conditions associated with F(x,y) at the interface ($\theta = 0$) are given by eqs. 37,

$$\sigma_\theta^{(1)}(r,0) = \sigma_\theta^{(2)}(r,0) \quad , \qquad [43.a]$$

$$\tau_{r\theta}^{(1)}(r,0) = \tau_{r\theta}^{(2)}(r,0) \quad , \qquad [43.b]$$

$$u^{(1)}(x,0) = u^{(2)}(x,0) \quad , \qquad [43.c]$$

$$v^{(1)}(x,0) = v^{(2)}(x,0) \quad . \qquad [43.d]$$

Equations 42.a through 43.d lead to the following 8 simultaneous equations associated with $F^{(\bullet)}(x,y)$:

$$\sum_{k=1}^{4} C_k^{(1)} r^\lambda (\cos \alpha_1 + \mu_k^{(1)} \sin \alpha_1)^{(\lambda+2)} = 0 \quad , \qquad [44.a]$$

$$\sum_{k=1}^{4} C_k^{(1)} r^\lambda (\mu_k^{(1)} \cos \alpha_1 - \sin \alpha_1)(\cos \alpha_1 + \mu_k^{(1)} \sin \alpha_1)^{(\lambda+1)} = 0 \quad , \qquad [44.b]$$

$$\sum_{k=1}^{4} C_k^{(2)} r^\lambda (-1)^{(\lambda+2)} = 0 \quad , \qquad [44.c]$$

$$\sum_{k=1}^{4} C_k^{(2)} r^\lambda \mu_k^{(2)} (-1)^{(\lambda+1)} = 0 \quad , \qquad [44.d]$$

$$\sum_{k=1}^{4} C_k^{(1)} r^{\lambda} (1)^{(\lambda+2)} = \sum_{k=1}^{4} C_k^{(2)} r^{\lambda} (1)^{(\lambda+2)} \quad , \qquad [44.e]$$

$$\sum_{k=1}^{4} C_k^{(1)} r^{\lambda} \mu_k^{(1)} (1)^{(\lambda+2)} = \sum_{k=1}^{4} C_k^{(2)} r^{\lambda} \mu_k^{(2)} (1)^{(\lambda+2)} \quad , \qquad [44.f]$$

$$\sum_{k=1}^{4} C_k^{(1)} p_k^{(1)} \frac{x^{(\lambda+1)}}{(\lambda+1)} = \sum_{k=1}^{4} C_k^{(2)} p_k^{(2)} \frac{x^{(\lambda+1)}}{(\lambda+1)} \quad , \qquad [44.g]$$

$$\sum_{k=1}^{4} C_k^{(1)} q_k^{(1)} \frac{x^{(\lambda+1)}}{(\lambda+1)} = \sum_{k=1}^{4} C_k^{(2)} q_k^{(2)} \frac{x^{(\lambda+1)}}{(\lambda+1)} \quad . \qquad [44.h]$$

The above set of equations form the eigenvalue problem for λ which is written symbolically as,

$$[\, A(\alpha_1, \lambda) \,] \vec{C} = 0 \quad . \qquad [45.a]$$

For a nontrivial solution the values of λ are given by,

$$| A(\alpha_1, \lambda) | = 0 \, . \qquad [45.b]$$

The vector $\vec{C}$ is composed of $\vec{C}^{(1)}$ and $\vec{C}^{(2)}$ associated with materials 1 and 2, respectively,

$$\vec{C} = \begin{Bmatrix} \vec{C}^{(1)} \\ \vec{C}^{(2)} \end{Bmatrix} \quad . \qquad [45.c]$$

The eigenvectors $\vec{C}^{(1)}$ and $\vec{C}^{(2)}$ consist of four constants each. If λ is complex, solutions occur in complex conjugate pairs of the form

$$\lambda = \eta \pm i\xi \quad . \qquad [45.d]$$

However, in order for the displacements u(x,y) and v(x,y) to stay finite at the origin,

$$-1 < \eta \quad . \qquad [45.e]$$

A detailed description of the eigenvalue problem for λ is given in Appendix B.

The eigenvalue problems associated with λ and δ do not occur in a standard form and hence require special procedures in order to determine the eigenvalues. Two methods were used in the present investigation, both methods involve the computation of the characteristic expressions (in closed-form or numerically) which is equal to the determinant of the particular matrix of interest, i.e., Q of eq. 41.b or A of eq. 45.b. The first method, Muller [34,35], operates on a complex characteristic equation to find the roots. Once a root is found it is eliminated (or deflated) from the characteristic expression. This method is particularly well suited for complex root computation (see ref. 35). The second method is based on the secant technique for simultaneous nonlinear equations [36]. Here the real and imaginary parts of the determinant are treated as a set of two simultaneous equations, with the two unknowns being η and ξ or γ and β.

Using the relations between the stresses and the stress functions, eqs. 15.a through 15.e, the eigenfunction expansion of the stresses can be written [23]. For the n^{th} real eigenvalue δ_n and λ_n, these stresses take the form,

$$\sigma_x^{(i)} = \sum_{n=1}^{\infty} c_n \left[\sum_{k=1}^{2} \mathrm{Re}\left(c_{nk}^{(i)} (\mu_k^{(i)})^2 Z_k^{\lambda_n} \right) + \mathrm{Im}\left(c_{n(k+2)}^{(i)} (\mu_k^{(i)})^2 Z_k^{\lambda_n} \right) \right] + \sigma_x^{(a_i)} \quad , \qquad [46.a]$$

$$\sigma_y^{(i)} = \sum_{n=1}^{\infty} c_n \left[\sum_{k=1}^{2} \mathrm{Re}\left(c_{nk}^{(i)} Z_k^{\lambda_n} \right) + \mathrm{Im}\left(c_{n(k+2)}^{(i)} Z_k^{\lambda_n} \right) \right] + \sigma_y^{(a_i)} \quad , \qquad [46.b]$$

$$\tau_{xy}^{(i)} = - \sum_{n=1}^{\infty} c_n \left[\sum_{k=1}^{2} \mathrm{Re}\left(c_{nk}^{(i)} \mu_k^{(i)} Z_k^{\lambda_n} \right) + \mathrm{Im}\left(c_{n(k+2)}^{(i)} \mu_k^{(i)} Z_k^{\lambda_n} \right) \right] + \tau_{xy}^{(a_i)} \quad , \qquad [46.c]$$

$$\tau_{yz}^{(i)} = - \sum_{n=1}^{\infty} d_n \left[\mathrm{Re}\left(d_{n1}^{(i)} \tilde{Z}_1^{\delta_n} \right) + \mathrm{Im}\left(d_{n2}^{(i)} \tilde{Z}_k^{\delta_n} \right) \right] + \tau_{yz}^{(a_i)} \quad , \qquad [46.d]$$

$$\tau_{xz}^{(i)} = - \sum_{n=1}^{\infty} d_n \left[\mathrm{Re}\left(d_{n1}^{(i)} \upsilon_1^{(i)} \tilde{Z}_1^{\delta_n} \right) + \mathrm{Im}\left(d_{2n}^{(i)} \upsilon_1^{(i)} \tilde{Z}_k^{\delta_n} \right) \right] + \tau_{xz}^{(a_i)} \quad . \qquad [46.e]$$

Whereas, for the n^{th} complex eigenvalues δ_n and λ_n the stresses take the following form:

$$\sigma_x^{(i)} = \sum_{n=1}^{\infty} \{ c_n \mathrm{Re}[\sum_{k=1}^{4} c_{nk}^{(i)} (\mu_k^{(i)})^2 Z_k^{\lambda_n}] + c'_n \mathrm{Im}[\sum_{k=1}^{4} c_{nk}^{(i)} (\mu_k^{(i)})^2 Z_k^{\lambda_n}] \} + \sigma_x^{(a_i)} \quad , \qquad [47.a]$$

$$\sigma_y^{(i)} = \sum_{n=1}^{\infty} \{ c_n \mathrm{Re}[\sum_{k=1}^{4} c_{nk}^{(i)} Z_k^{\lambda_n}] + c'_n \mathrm{Im}[\sum_{k=1}^{4} c_{nk}^{(i)} Z_k^{\lambda_n}] \} + \sigma_y^{(a_i)} \quad , \qquad [47.b]$$

$$\tau_{xy}^{(i)} = - \sum_{n=1}^{\infty} \{ c_n \mathrm{Re}[\sum_{k=1}^{4} c_{nk}^{(i)} \mu_k^{(i)} Z_k^{\lambda_n}] + c'_n \mathrm{Im}[\sum_{k=1}^{4} c_{nk}^{(i)} \mu_k^{(i)} Z_k^{\lambda_n}] \} + \tau_{xy}^{(a_i)} \quad , \qquad [47.c]$$

$$\tau_{yz}^{(i)} = - \sum_{n=1}^{\infty} \{ d_n \mathrm{Re}[\sum_{k=1}^{2} d_{nk}^{(i)} \tilde{Z}_k^{\delta_n}] + d'_n \mathrm{Im}[\sum_{k=1}^{2} d_{nk}^{(i)} \tilde{Z}_k^{\delta_n}] \} + \tau_{yz}^{(a_i)} \quad , \qquad [47.d]$$

$$\tau_{xz}^{(i)} = \sum_{n=1}^{\infty} \{ d_n \mathrm{Re}[\sum_{k=1}^{2} d_{nk}^{(i)} \upsilon_k^{(i)} \tilde{Z}_k^{\delta_n}] + d'_n \mathrm{Im}[\sum_{k=1}^{2} d_{nk}^{(i)} \upsilon_k^{(i)} \tilde{Z}_k^{\delta_n}] \} + \tau_{xz}^{(a_i)} \quad , \qquad [47.e]$$

where, $i = 1,2$ corresponding to material 1 (flange) and material 2 (skin). In addition, c_n, c'_n, d_n and d'_n are unknown real coefficients, whereas, $c_{nk}^{(i)}$ and $d_{nk}^{(i)}$, $i = 1,2$, are known quantities of the normalized n^{th} eigenvector associated with materials 1 and 2 respectively. The reader is referred to Appendix B for a detailed discussion of the appropriate eigenfunction representation for a real and complex eigenvalue. Next the application of the boundary and interface conditions on the auxiliary and particular portions of the solution is discussed.

2.3.3.b The Remaining Part of the Solution

In previous sections we saw that the imposition of traction-free boundary and interface conditions on the eigenvalue expansion part of the solution for $F(x,y)$ and $\Psi(x,y)$ led to the eigenvalue problems for λ and δ, respectively. In this section these conditions are enforced on the other parts of these solutions (i.e. $F^{(a)}(x,y)$, $\Psi^{(a)}$ and $\Psi^{(p)}(x,y)$). The imposition of the boundary and interface conditions are implemented in the context of the skin-stiffener geom-

etry as discussed in section 2.3.2. The traction and displacement continuity conditions are given by eqs. 37. These conditions require that,

$$u^{(1)}(x,0) = u^{(2)}(x,0) \quad , \qquad [48.a]$$

$$v^{(1)}(x,0) = v^{(2)}(x,0) \quad , \qquad [48.b]$$

$$\tau_{xy}^{(1)}(x,0) = \tau_{xy}^{(2)}(x,0) \quad , \qquad [48.c]$$

$$\tau_{yz}^{(1)}(x,0) = \tau_{yz}^{(2)}(x,0) \quad , \qquad [48.d]$$

$$\sigma_{y}^{(1)}(x,0) = \sigma_{y}^{(2)}(x,0) \quad . \qquad [48.e]$$

Here we chose to use the Cartesian components of stress. Considering eqs. 11.a through 11.c and 29.a through 30.e the above relations become:

$$-\frac{B_1^{(1)} a_{33}^{(1)}}{2} z^2 + U^{(a_1)}(x,0) + \omega_2^{(1)} z + u_o^{(1)} = \qquad [49.a]$$

$$-\frac{B_1^{(2)} a_{33}^{(2)}}{2} z^2 + U^{(a_2)}(x,0) + \omega_2^{(2)} z + u_o^{(2)} \quad ,$$

$$\frac{B_2^{(1)} a_{33}^{(1)}}{2} z^2 + B_4^{(1)} x z + V^{(a_1)}(x,0) + \omega_3^{(1)} x - \omega_1^{(1)} z + v_o^{(1)} = \qquad [49.b]$$

$$-\frac{B_2^{(2)} a_{33}^{(2)}}{2} z^2 + B_4^{(2)} x z + V^{(a_2)}(x,0) + \omega_3^{(2)} x - \omega_1^{(2)} z + v_o^{(2)} \quad ,$$

$$(B_1^{(1)} x + B_3^{(1)}) a_{33}^{(1)} z + W^{(a_1)}(x,0) - \omega_2^{(1)} x + w_o^{(1)} = \qquad [49.c]$$

$$(B_1^{(2)} x + B_3^{(2)}) a_{33}^{(2)} z + W^{(a_2)}(x,0) - \omega_2^{(2)} x + w_o^{(2)} \quad ,$$

$$-2 b_2^{(1)} x + b_6^{(1)} = -2 b_2^{(2)} x + b_6^{(2)} \quad , \qquad [49.d]$$

$$2\,b_{10}^{(1)}\,x \;+\; b_{8}^{(1)} \;=\; 2\,b_{10}^{(2)}\,x \;+\; b_{8}^{(2)} \quad , \qquad [49.e]$$

$$6\,b_{1}^{(1)}\,x \;+\; 2\,b_{5}^{(1)} \;=\; 6\,b_{1}^{(2)}\,x \;+\; 2\,b_{5}^{(2)} \quad . \qquad [49.f]$$

Matching coefficients of the same power of x,y, and z we arrive at the following relations:

$$B_i^{(1)}\,a_{33}^{(1)} \;=\; B_i^{(2)}\,a_{33}^{(2)} \quad , \quad i \;=\; 1,2,3 \quad , \qquad [50.a]$$

$$B_4^{(1)} \;=\; B_4^{(2)} \quad , \qquad [50.b]$$

$$\omega_i^{(1)} \;=\; \omega_i^{(2)} \quad , \quad i \;=\; 1,2 \quad , \qquad [50.c]$$

$$b_i^{(1)} \;=\; b_i^{(2)} \quad , \quad i \;=\; 1,2,5,6,8,10 \qquad [50.d]$$

$$U^{(a_1)}(x,0) + u_o^{(1)} \;=\; U^{(a_2)}(x,0) + u_o^{(2)} \quad , \qquad [50.e]$$

$$V^{(a_1)}(x,0) + \omega_3^{(1)}\,x + v_o^{(1)} \;=\; V^{(a_2)}(x,0) + \omega_3^{(2)}\,x + v_o^{(2)} \quad , \qquad [50.f]$$

$$W^{(a_1)}(x,0) + w_o^{(1)} \;=\; W^{(a_2)}(x,0) + w_o^{(2)} \quad , \qquad [50.g]$$

where the superscripts 1 and 2 correspond to material 1 (flange) and material 2 (skin). Next the traction-free conditions are applied to the skin and flange free surfaces. These conditions for the skin, eq. 36.b, require that,

$$\sigma_\theta^{(2)}(r, -\pi) \;=\; 0 \quad , \qquad [51.a]$$

$$\tau_{r\theta}^{(2)}(r, -\pi) \;=\; 0 \quad , \qquad [51.b]$$

$$\tau_{z\theta}^{(2)}(r, -\pi) \;=\; 0 \quad . \qquad [51.c]$$

Consideration of eqs. 29 through 32 in conjunction with the above conditions leads to the following relations:

$$- 6\, b_1^{(2)}\, r + 2\, b_5^{(2)} = 0 \quad , \qquad [52.a]$$

$$2\, b_2^{(2)}\, r - b_6^{(2)} = 0 \quad , \qquad [52.b]$$

$$b_8^{(2)} - 2\, b_{10}^{(2)}\, r = 0 \quad . \qquad [52.c]$$

Equating coefficients of the same power of r yields

$$b_i^{(2)} = 0 \quad , \quad i = 1,2,5,6,8,10 \quad . \qquad [53]$$

Finally, considering eq. 50.d together with eq. 53 leads to

$$b_i^{(1)} = b_i^{(2)} = 0 \quad , \quad i = 1,2,5,6,8,10 \quad . \qquad [54]$$

Based on the above results, the auxiliary stress components, eqs. 30, reduce to

$$\sigma_x^{(a)} = 2\, b_3\, x + 6\, b_4\, y + 2\, b_7 \quad , \qquad [55.a]$$

$$\sigma_y^{(a)} = 0 \quad , \qquad [55.b]$$

$$\tau_{xy}^{(a)} = - 2\, b_3\, y \quad , \qquad [55.c]$$

$$\tau_{yz}^{(a)} = 0 \quad , \qquad [55.d]$$

$$\tau_{xz}^{(a)} = b_9 + 2\, b_{11}\, y \quad . \qquad [55.e]$$

Further information can be obtained by considering the traction-free conditions for the flange (material 1). These conditions are

$$\sigma_\theta^{(1)}(r, \alpha_1) = 0 \quad , \qquad [56.a]$$

$$\tau_{r\theta}^{(1)}(r, \alpha_1) = 0 \quad , \qquad [56.b]$$

$$\tau_{z\theta}^{(1)}(r,\alpha_1) = 0 \quad . \qquad [56.c]$$

The use of these conditions, together with eqs. 32 and 55, leads to the following relations:

$$6\,r\,n^2\,[\,m\,b_3^{(1)} + n\,b_4^{(1)}\,] + 2\,b_7^{(1)}\,n^2 = 0 \quad , \qquad [57.a]$$

$$-\,2\,r\,n\,[\,b_3^{(1)}\,(2\,m^2 - n^2) + 3\,b_4^{(1)}\,m\,n\,] - 2\,m\,n\,b_7^{(1)} = 0 \quad , \qquad [57.b]$$

$$-\,n\,b_9^{(1)} - 2\,b_{11}^{(1)}\,r\,n^2 = 0 \quad , \qquad [57.c]$$

where, $m = \cos(\alpha_1)$, $n = \sin(\alpha_1)$. Equating coefficients of the same power of r leads to

$$b_i^{(1)} = 0 \quad , \quad i = 3,4,7,9,11 \quad . \qquad [58]$$

Finally, considering eqs. 50.e through 50.g in conjunction with eqs. 27.b, 35, 54 and 58 leads to

$$\beta_{11}^{(2)}\,b_3^{(2)} = \frac{a_{13}^{(1)}}{2}\,B_1^{(1)} - \frac{a_{13}^{(2)}}{2}\,B_1^{(2)} \quad , \qquad [59.a]$$

$$2\,\beta_{11}^{(2)}\,b_7^{(2)} = a_{13}^{(1)}\,B_3^{(1)} - a_{13}^{(2)}\,B_3^{(2)} \quad , \qquad [59.b]$$

$$3\,\beta_{11}^{(2)}\,b_4^{(2)} = \frac{a_{13}^{(1)}}{2}\,B_2^{(1)} - \frac{a_{13}^{(2)}}{2}\,B_2^{(2)} \quad , \qquad [59.c]$$

$$b_9^{(2)} = 0 \quad , \qquad [59.d]$$

$$b_{11}^{(2)} = -\,\frac{2\,B_4^{(2)}}{\beta_{55}^{(2)}} \quad . \qquad [59.e]$$

Applying relation 50.a produces

$$b_3^{(2)} = K\,B_1^{(2)} \quad , \quad b_4^{(2)} = \frac{K}{3}\,B_2^{(2)} \quad , \quad b_7^{(2)} = K\,B_3^{(2)} \quad , \qquad [60.a,b,c]$$

where,

$$K = \frac{1}{2}\left[\frac{a_{13}^{(1)} a_{33}^{(2)} - a_{13}^{(2)} a_{33}^{(1)}}{\beta_{11}^{(2)} a_{33}^{(1)}}\right] . \qquad [60.d]$$

Finally, considering all the relations derived in this section, the auxiliary stresses for the skin and stiffener are as follows:

Flange (material 1)

$$\sigma_x^{(a_1)} = \sigma_y^{(a_1)} = \tau_{xy}^{(a_1)} = \tau_{yz}^{(a_1)} = \tau_{xz}^{(a_1)} = 0 . \qquad [61.a]$$

Skin (material 2)

$$\sigma_x^{(a_2)} = 2K(B_1^{(2)} x + B_2^{(2)} y + B_3^{(2)}) , \qquad [61.b]$$

$$\sigma_y^{(a_2)} = 0 , \quad \tau_{yz}^{(a_2)} = 0 , \qquad [61.c,d]$$

$$\tau_{xy}^{(a_2)} = -2K B_1^{(2)} y , \quad \tau_{xz}^{(a_2)} = -\frac{2 B_4^{(2)}}{\beta_{55}^{(2)}} y . \qquad [61.e,f]$$

The stresses in material 1 (flange) and material 2 (skin) are given by eqs. 46.a through 47.e. These stresses are given in terms of the unknown coefficients c_n, c'_n, d_n, d'_n, and B_i, i = 1,2,3,4. For the specific skin-stiffener problem these coefficients are determined by a collocation procedure. This is discussed next.

2.4 Collocation Procedure

The eigenfunction expansion elasticity solution is valid for a semi-infinite domain. The particular boundary value problem associated with the skin-stiffener geometry is solved by assuming that the solution is valid in the finite domain represented by the localized flange termination region. Furthermore, the solution is assumed to be represented by a finite number of terms in the series. The unknown coefficients c_n and c'_n in eqs. 46.a through 46.c and 47.a through 47.c are determined using the boundary collocation technique. Referring to Figure 2, the boundary of the local region is bounded by contour ABCDEFA. In the actual structure analysed, boundaries AF, AB, BC, and ED are traction free, whereas boundaries CD and EF are subjected to both normal, σ_n, and tangential, τ_s tractions. Obviously in the nomenclature of the problem, $\sigma_n = \sigma_x$ and $\tau_s = \tau_{xy}$ on CD and EF, and $\sigma_n = \sigma_y$ and $\tau_s = \tau_{xy}$ on BC and DE. By the development of the elasticity solution, the traction-free conditions on FA and AB are already satisfied. The collocation procedure is used to satisfy the traction-free conditions on boundaries BC and DE, and to match the normal and tangential tractions on boundaries CD and EF as determined by the global finite-element analysis. It should be noted that in the boundary collocation procedure, the normal and shear stresses, σ_n and τ_s , along the contour BCDEF are written in terms of the unknown coefficients, c_n and c'_n in a truncated eigenfunction expansion. These stresses are matched with the same stress components calculated by the finite-element analysis on the contour. Although it is possible to collocate other responses, such as three components of stress, the strains, the displacements, etc., it is felt that matching the normal and shear stresses on the boundary is the best choice. The main reason for this is the fact that enforcement of the force equilibrium conditions on the local region as a finite body involves only the normal and shear traction on the boundary of the body.

For the specific problem here, the collocation at m points around boundary BCDEF leads to 2m simultaneous equations from which the 2n unknown coefficients are determined. The

use of more collocations points (i.e., m > n) leads to an overdetermined set of equations. Solution of these equations produces the 2n unknown coefficients c_n and c'_n which satisfy all boundary conditions in a least-squares sense. If the original set of equations is represented by,

$$\vec{S} = A\,\vec{C} \quad , \qquad [62.a]$$

then the least squares solution for $\vec{C}$ is [37],

$$\vec{C} = (A^T A)^{-1} A^T \vec{S} \quad . \qquad [62.b]$$

In the above, A is a 2m x 2n known matrix (for which m > n), $\vec{S}$ is a vector of length 2m consisting of a 2m known boundary stress quantities, and $\vec{C}$ is a vector of length 2n consisting of 2n unknown coefficients, c_n and c'_n , of the truncated eigenfunction. The elements of matrix A involve material properties and the coordinates of the collocation points. Once these coefficients are determined, the stresses in the localized region can be written. For a converged eigenfunction, these stresses are assumed to represent the true stress field in this region. In a later section convergence is studied by varying the number of terms (or eigenvalues) in the truncated function expansion and by varying the number of collocation points.

2.5 Global Finite-Element Analysis

To facilitate the application of the local elasticity solution to the skin-stiffener problem, a finite-element program was implemented which incorporated the generalized plane deformation assumption. This finite-element formulation is consistent with the elasticity solution developed earlier. The finite-element program was developed for two reasons. The primary reason was to provide boundary conditions for the eigenvalue expansion local elasticity sol-

ution. The second reason was to check the results of the eigenvalue expansion. As indicated in the introduction, the methodology was developed for geometrically linear problems, and then extended to geometrically nonlinear problems. Thus the finite-element program implementation was very important in the first step of the solution strategy development.

A body which conforms to the generalized plane deformation assumption may be analysed using a two-dimensional finite-element model. In this section a short description of the finite-element program (PE2D) is given. The PE2D program developed is based on the FEM2D finite-element program, [38], with the appropriate modifications to meet the need of the present investigation. For a more detailed discussion the reader is referred to Appendix C.

The generalized plane deformation elasticity finite-element model is based on the displacement field given by eqs. 11.a through 11.c for homogeneous anisotropic bodies for which stresses do not vary along the generator (i.e., the z axis). This displacement field can be written in vectorial form as,

$$\vec{u} = \vec{u}_o + \vec{U} \quad , \qquad [63]$$

where;

$$\vec{U}^T = \{U(x,y) \; ; \; V(x,y) \; ; \; W(x,y)\} \quad ,$$

$$\vec{u}_o^T = \{u_o(x,y,z) \; ; \; v_o(x,y,z) \; ; \; w_o(x,y,z)\} \quad ,$$

and,

$$u_o(x,y,z) = -\frac{B_1 a_{33}}{2} z^2 - B_4 yz \quad ,$$

$$v_o(x,y,z) = -\frac{B_2 a_{33}}{2} z^2 + B_4 xz \quad ,$$

$$w_o(x,y,z) = (B_1x + B_2y + B_3)a_{33}z \quad .$$

Here the terms associated with the rigid body rotation and translation are omitted. The unknown functions U(x,y), V(x,y) and W(x,y), are approximated according to the finite-element method. Further, it may be shown that the unknown constants B_i, (i = 1,2,3,4) are related to the body's kinematic end conditions, that is:

$$B_3 = \frac{e_o}{a_{33}} \quad , \quad B_2 = \frac{\kappa_z}{a_{33}} \quad , \quad B_4 = -\frac{\kappa_{xz}}{2} \quad . \qquad [64]$$

In the stiffened skin structural context, e_o and κ_z are the axial extension and curvature in the z direction, and κ_{xz} is the twist curvature about the z axis. The coefficient B_1 is related to the inplane twist about the y-axis and is of no consequence in the structure considered here and is therefore set to zero. The strain vector, $\vec{\varepsilon}_x$, is given by,

$$\vec{\varepsilon}_x = \vec{E} + \vec{\varepsilon}_o \quad , \qquad [65]$$

where;

$$\vec{\varepsilon}_x^T = \{\varepsilon_x \; ; \; \varepsilon_y \; ; \; \varepsilon_z \; ; \; \gamma_{yz} \; ; \; \gamma_{xz} \; ; \; \gamma_{xy}\} \quad ,$$

$$\vec{E}^T = \{\frac{\partial U}{\partial x} \; ; \; \frac{\partial V}{\partial y} \; ; \; 0 \; ; \; \frac{\partial W}{\partial y} \; ; \; \frac{\partial W}{\partial x} \; ; \; \frac{\partial U}{\partial y} + \frac{\partial V}{\partial x}\} \quad ,$$

$$\vec{\varepsilon}_o^T = \{0 \; ; \; 0 \; ; \; (e_o + \kappa_z \, y) \; ; \; -\frac{\kappa_{xz}}{2}x \; ; \; \frac{\kappa_{xz}}{2}y \; ; \; 0\} \quad .$$

Since only orthotropic media are being considered, the constitutive relation is as given before (see eq, 6.a) as

$$\vec{\sigma}_x = [A]\vec{\varepsilon}_x \quad .$$

Considering eqs. 6.a and 65, it may be concluded that the problem of determining V(x,y) and U(x,y) decouples from the problem of determining W(x,y). In addition, since U,V and W are functions which depend on x and y alone, only a two-dimensional finite-element model is required. The finite-element model is derived via the variation formulation in a standard manner. The conditions for this model consist of specified overall kinematic conditions (i.e., e_o, κ_z, and κ_{xz} specified) and force and/or kinematic conditions on the boundary in the x-y plane. It should be pointed out that because of the generalized plane deformation assumption, the specified overall kinematic conditions e_o, κ_z and κ_{xz} do not vary along the the z-axis of the body.

2.6 Verification of the Analytical Model

In this section attention is given to a results relevant to the verification of the linear analysis model. In addition, the fidelity of the local-global elasticity-finite-element analysis is demonstrated. By fidelity is meant the accurate representation of stresses by the elasticity solution within the localized region and the smooth transition to the global region. Whereas the convergence of the finite-element method has been discussed in [39], there is no rigorous proof for the convergence of the collocation method and its application to the present problem. For the problem here the accuracy of such a procedure will depend on a number of factors such as: a) the accuracy of the boundary conditions; b) the number of eigenvalues used in the eigenfunction expansion; and c) the number of collocation data points. In the following section these issues will be addressed.

In order to study convergence and accuracy of the current model, the elasticity results are compared with results from a finite-element analysis in which the mesh was refined twice in the localized region. The results are compared for a particular problem. The use of a finite-

element analysis for comparison is due to the lack of another analysis of this particular problem. Two flange geometries are considered in this phase of the study, a 90° and a 45° flange termination angle, i.e., $\alpha_1 = 90°$ and $\alpha_1 = 45°$ in Figures 2 and 3. Two angles were considered at this stage so as to make conclusions regarding model verification more general. The flange and the skin are constructed of an 8-ply quasi-isotropic $(\pm 45/0/90)_s$ laminate, and an 8-ply orthotropic $(\pm 45/90_2)_s$ laminate, respectively. Material properties are given in Appendix D. The finite-element discretization for 90° and 45° flange angle skin-stiffener geometries are shown in Figures 4a and 5a, respectively, for what is referred to as the coarse mesh. Subsequent mesh refinements of the localized region are shown in Figures 4b,c and 5b,c. Due to the geometric and material symmetry, only one-half of the structure cross-section is modeled. The particular problem considered for the verification study is shown Figures 4.a and 5.a, namely the stiffened plate subjected to a pure bending moment M. The particular loading was chosen to illustrate the computational method because this loading produce peeling and shearing stresses at the skin-stiffener interface that are approximately the same order of magnitude. It should be mentioned that for this problem τ_{zx} and τ_{zy} are identically zero. Therefore, attention is focused on σ_x, σ_y, and τ_{xy}. The exact nature of the skin-stiffener interface stresses near the flange terminus depends on the the value of η_1, the real part of the first eigenvalue (see eq. 45.d). These stresses are unbounded if $-1 < \eta_1$.

In the collocation procedure, the normal, σ_n, and tangential, τ_s, stresses are collocated along the closed contour ABCDEFA shown in Figures 4 and 5 by the heavy line. The stresses as computed by the finite-element analysis of the entire cross section are used to provide collocation data on the contour. In reality, collocation takes place only along boundaries BC, CD, DE, and EF, since the conditions of stress-free boundaries along AB and FA are satisfied exactly by the elasticity solution. Boundaries BC and DE were taken as stress-free faces of the skin and flange, respectively, whereas the stresses along the internal boundaries CD and EF are those determined by the finite-element analysis. These stresses on the boundary are calculated exactly within the finite-element context by postprocessing the finite-element dis-

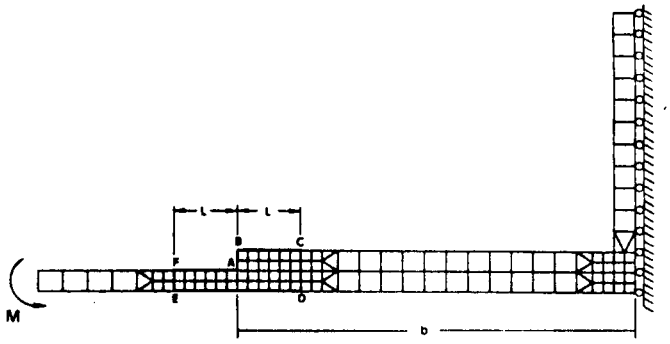

(a) Coarse Mesh

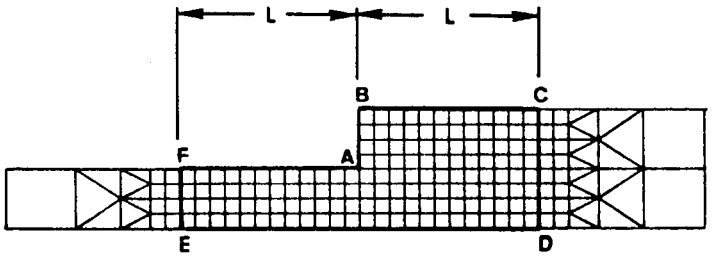

(b) Refined Mesh

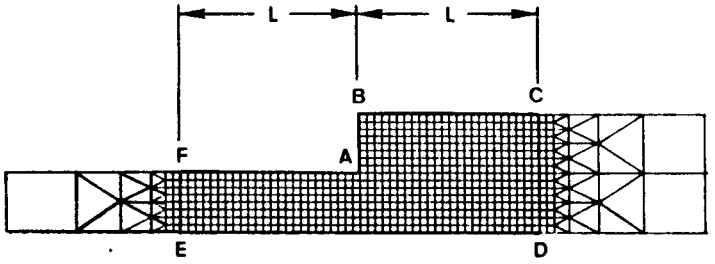

(c) Fine Mesh

Figure 4. Loading and Finite-Element Discretizations of Skin-Stiffener 90° Flange Termination Angle.

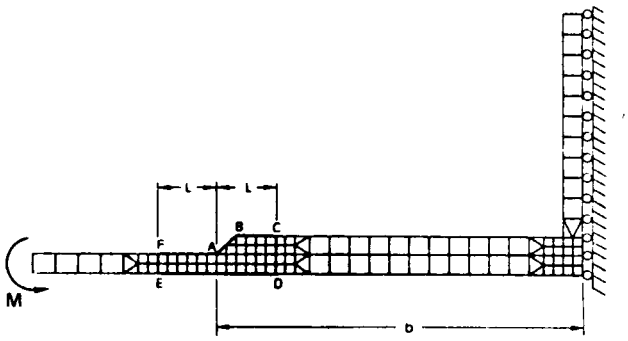

(a) Coarse Mesh

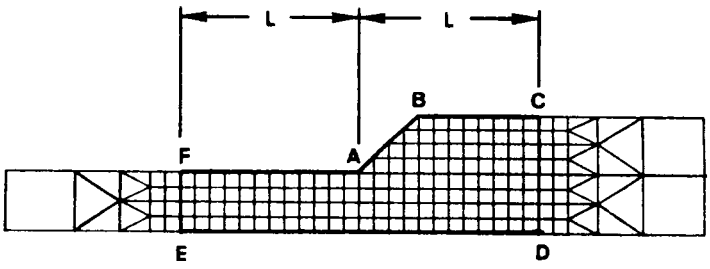

(b) Refined Mesh

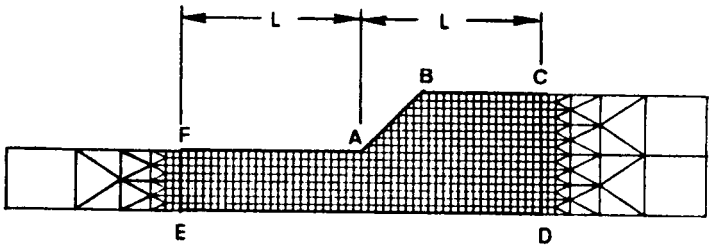

(c) Fine Mesh

Figure 5. Loading and Finite-Element Discretizations of Skin-Stiffener 45° Flange Termination Angle.

placement data. The collocation points are uniformly spaced along the contour. The boundaries CD and EF are placed at distance L from point A. This distance, shown in Figures 4 and 5, was chosen according to the condition that σ_y and τ_{xy} as computed by the finite-element analysis must be continuous across the skin-flange interface. That is, the stresses σ_y and τ_{xy} computed by the elements on either side of the interface in the skin and flange must yield the same value to within 5%. The theory of elasticity stipulates that these two components of stress are exactly continuous across the interface. This 5% condition assures that the skin-stiffener interlaminar stresses computed by the finite-element satisfy this condition to with a small tolerance and thus are accurate in the global region. Based on this 5% condition, it was determined that for the coarse mesh, L should be about 1.5 times the combined thickness of the skin and flange. This value of L was kept constant for all subsequent mesh refinements in order to eliminate variation in the results which may depend on L. In the subsequent figures the stresses are plotted as a function of the normalized distance, $\bar{x} = x/t_s$, from the flange termination vertex (point A in Figures 4 and 5), where t_s denotes the skin thickness. In all figures, whenever σ_x stress data is presented, values computed both in the skin and in the flange are given. This dual computation is done because the stress component σ_x is discontinuous at the interface and will have different values in the skin and flange. However, if interface stress data for σ_y and τ_{xy}, as computed by the elasticity solution, are given, only one value is provided, since as stated above, these stress components are continuous across the interface. On the other hand, for the finite-element computation of these two stress components, both the stresses in the skin and the stresses in the flange are given. Plotting both the flange and skin finite-element components will illustrate the degree to which the continuity condition on these stresses is violated as the stress gradient becomes severe near the flange termination region. Finally, all stress components are normalized by $\frac{M t_s}{2 I}$, where M is the applied moment, $\frac{t_s}{2}$ is the distance from the neutral axis of the skin to the outer surface of the skin, and I is the moment of inertia of a section of skin of unit depth into the paper. This strength-of-materials view of normalizing the stresses is meant only as aid to not having to become involved in discussing the actual magnitude of the numbers. The normalized stresses are

denoted as $\bar{\sigma}_x$, $\bar{\sigma}_y$, and $\bar{\tau}_{xy}$. Throughout the study, the stresses, and infact, distances, have been normalized in a manner relevant to the particular problem.

Figures 6 through 11 show the variation of the skin-stiffener interlaminar stresses, σ_x, σ_y, and τ_{xy} as a function of distance along the interface for the 90° and 45° flange termination angles. Both stresses determined by the finite-element analysis and those calculated using the truncated eigenfunctions, eqs. 46 and 47, are shown. The elasticity results shown in the figures were generated using 15 eigenvalues and 100 collocation points. The eigenvalues for both geometries are given in Appendix D. Each figure illustrates calculated values of a particular stress component for each of the three different meshes (i.e., coarse, refined, and fine). The data point closest to the vertex for which finite-element stress data is plotted is at $\bar{x} = 0.025$. It should be noted that $\bar{x}$ goes from 0 to 3 because the skin and flange are of equal thickness, t_s , and the length of the local region, L, is 1.5 times the combined thickness of the flange and skin, $2t_s$. The scale of the vertical axes was taken to account for the value of the normalized stress at $\bar{x} = 0.025$.

A number of interesting observations can be made from these figures. In general, for both flange termination angles, at sufficient distances from the flange termination vertex, the finite-element and the elasticity solutions show excellent agreement for all three components of stress. The point at which this agreement can be categorized as being excellent moves closer and closer to the vertex with increases in the mesh refinement. As will be discussed shortly, there is very little difference between the elasticity solution resulting from collocating data from a coarse mesh and the elasticity solution resulting from collocating data from the fine mesh. In essence, for either flange termination angle, the elasticity solution does not change from one mesh to the next and hence the use of the coarse mesh is sufficient. What the figures are showing is that the elasticity solution coincides with the solution the finite-element analysis is appearing to converge to. It should also be noted that σ_y and τ_{xy} computed by the finite-elements adjacent to the interface are discontinuous across the interface in some region near the vertex. The situation is worst for τ_{xy} than for σ_y. This discontinuity relates to

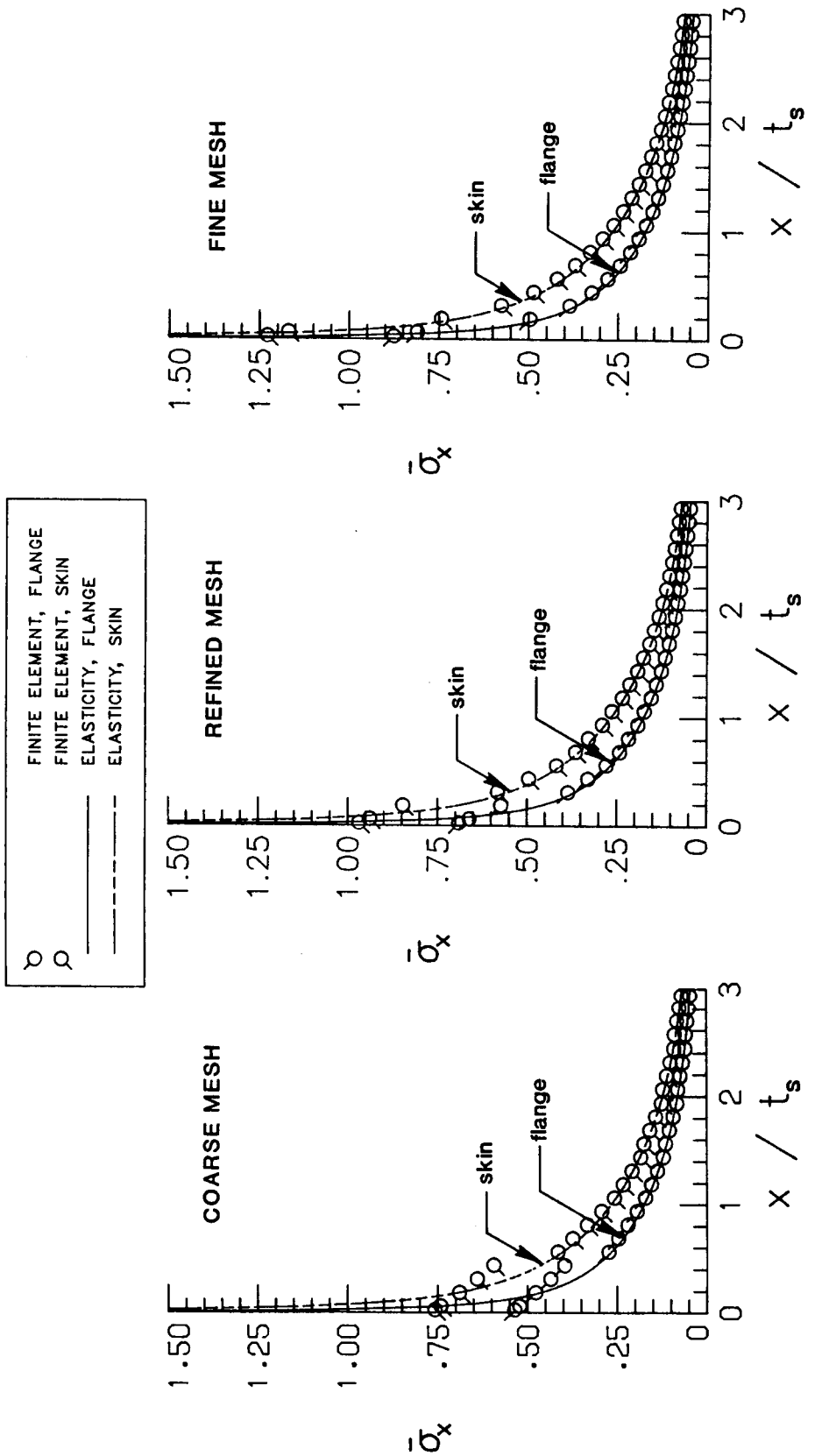

Figure 6. Skin-Stiffener Stress σ_x for 90° Flange Termination Angle, Finite-Element and Elasticity Results Using 15 Eigenvalues and 100 Collocation points.

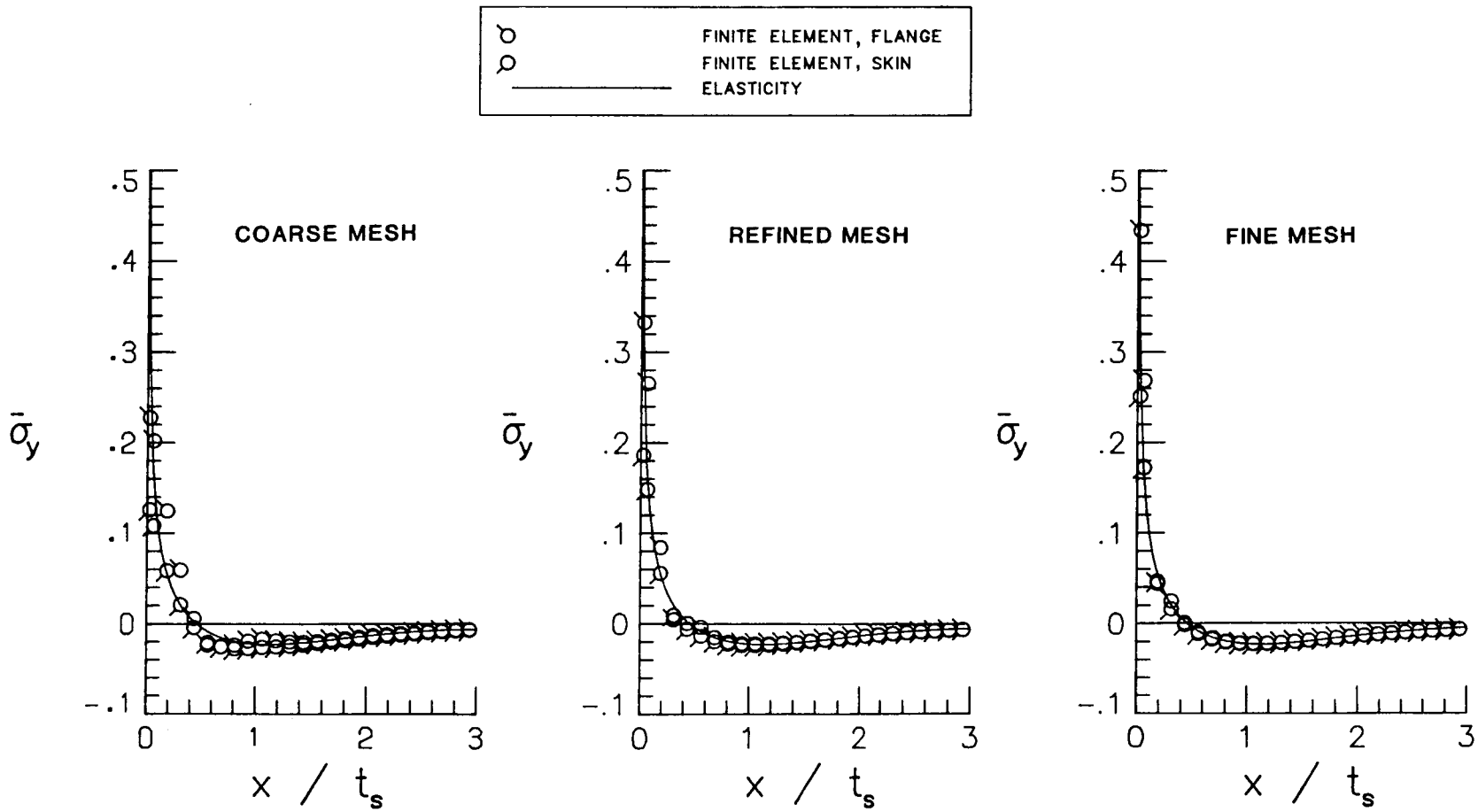

Figure 7. Skin-Stiffener Stress σ_y for 90° Flange Termination Angle, Finite-Element and Elasticity Results Using 15 Eigenvalues and 100 Collocation points.

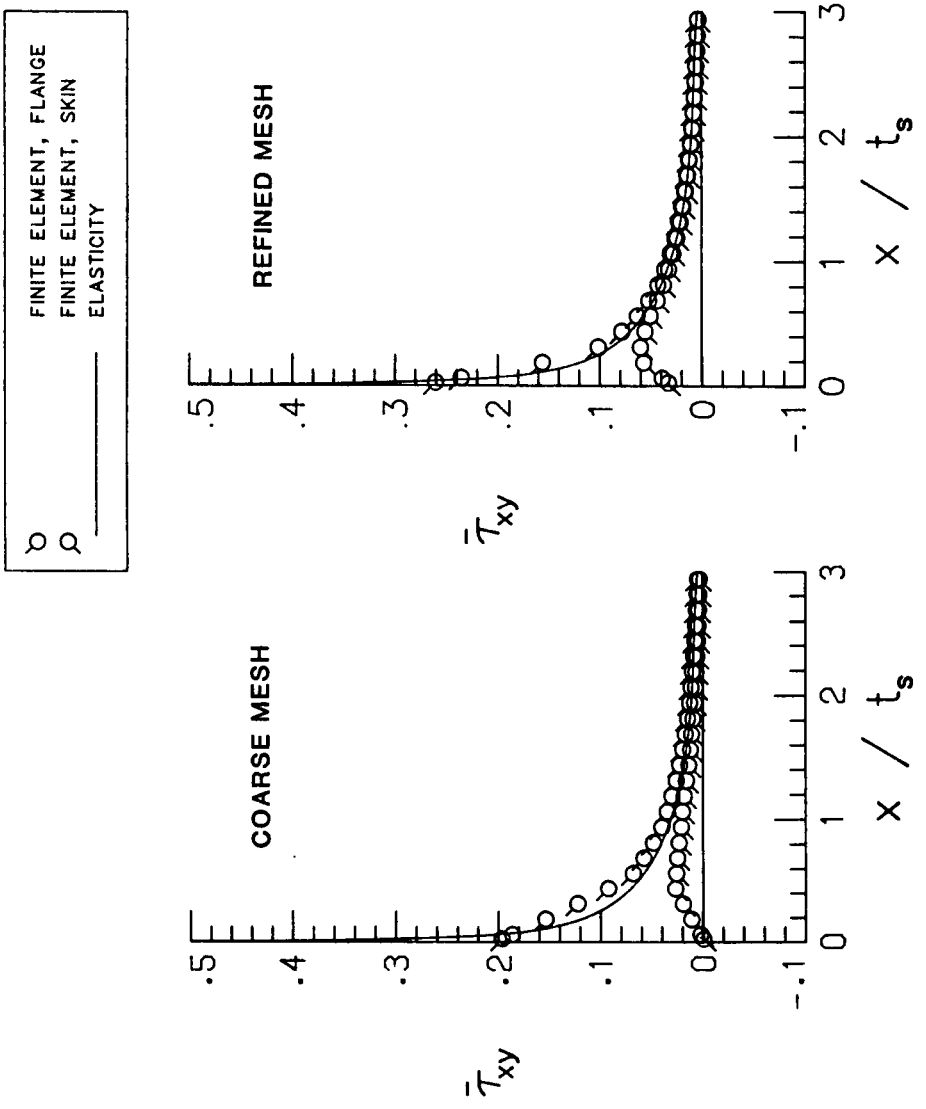

Figure 8. Skin-Stiffener Stress τ_{xy} for 90° Flange Termination Angle, Finite-Element and Elasticity Results Using 15 EigenValues and 100 Collocation points.

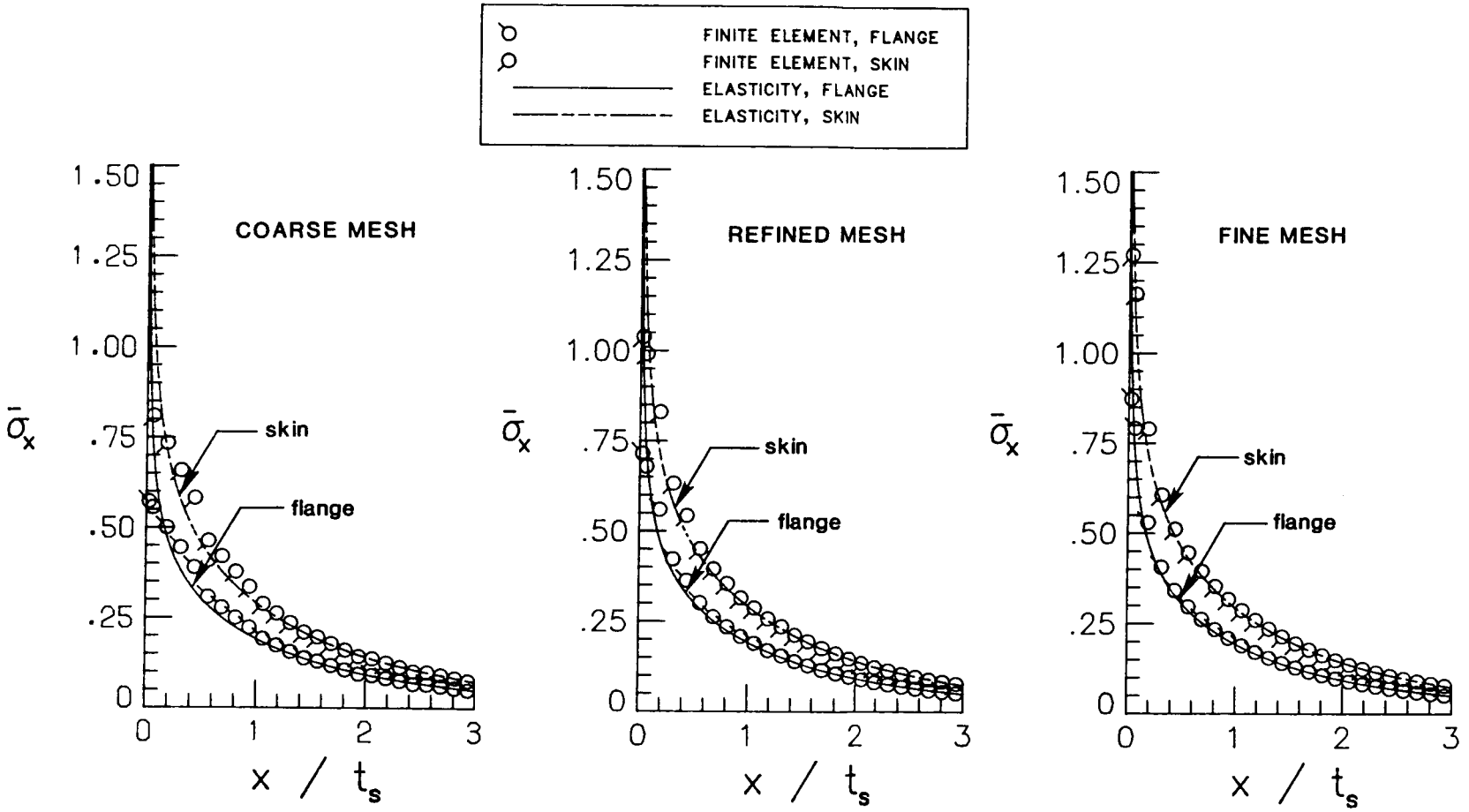

Figure 9. Skin-Stiffener Stress σ_x for 45° Flange Termination Angle, Finite-Element and Elasticity Results Using 15 Eigenvalues and 100 Collocation points.

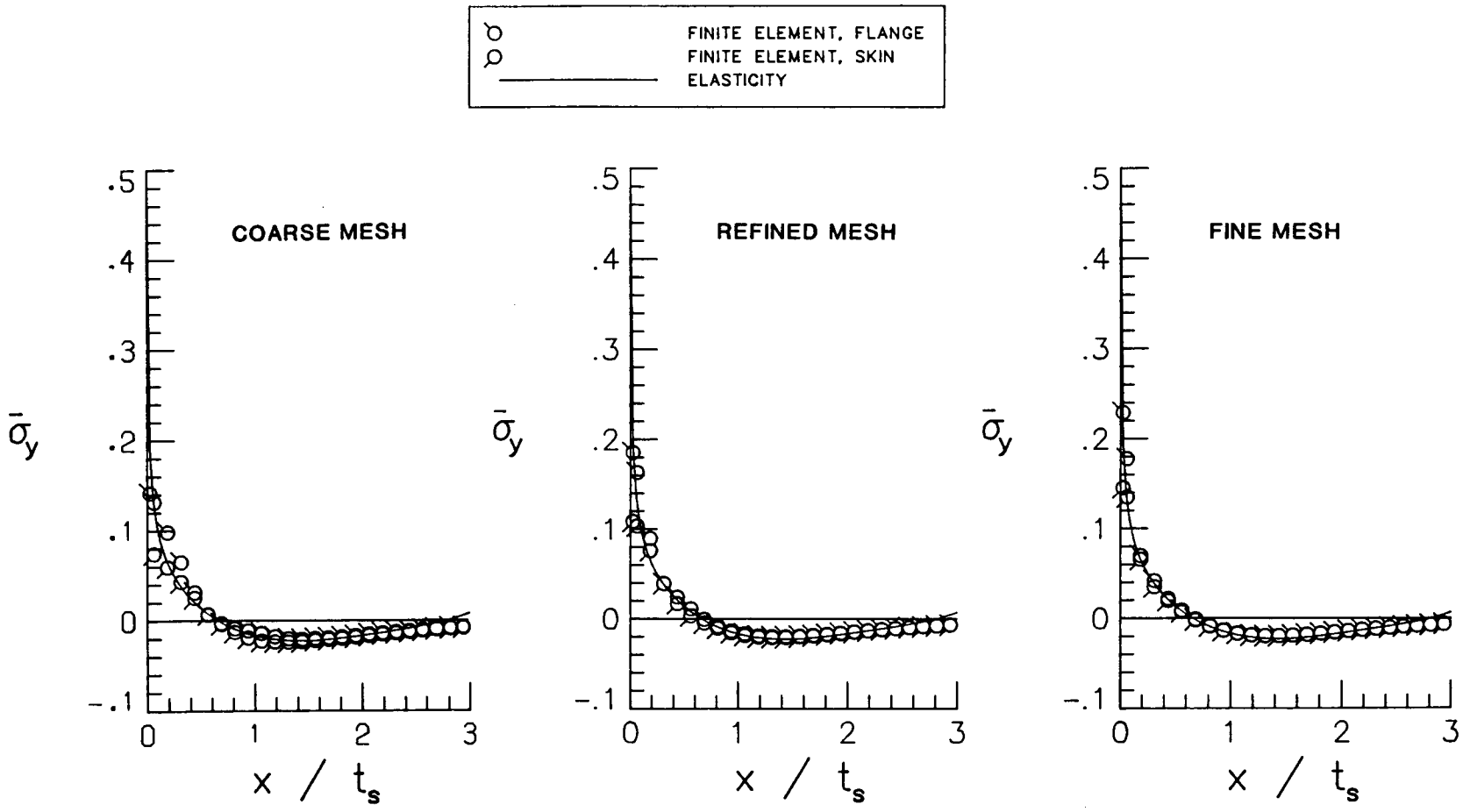

Figure 10. Skin-Stiffener Stress σ_y for 45° Flange Termination Angle, Finite-Element and Elasticity Results Using 15 Eigenvalues and 100 Collocation points.

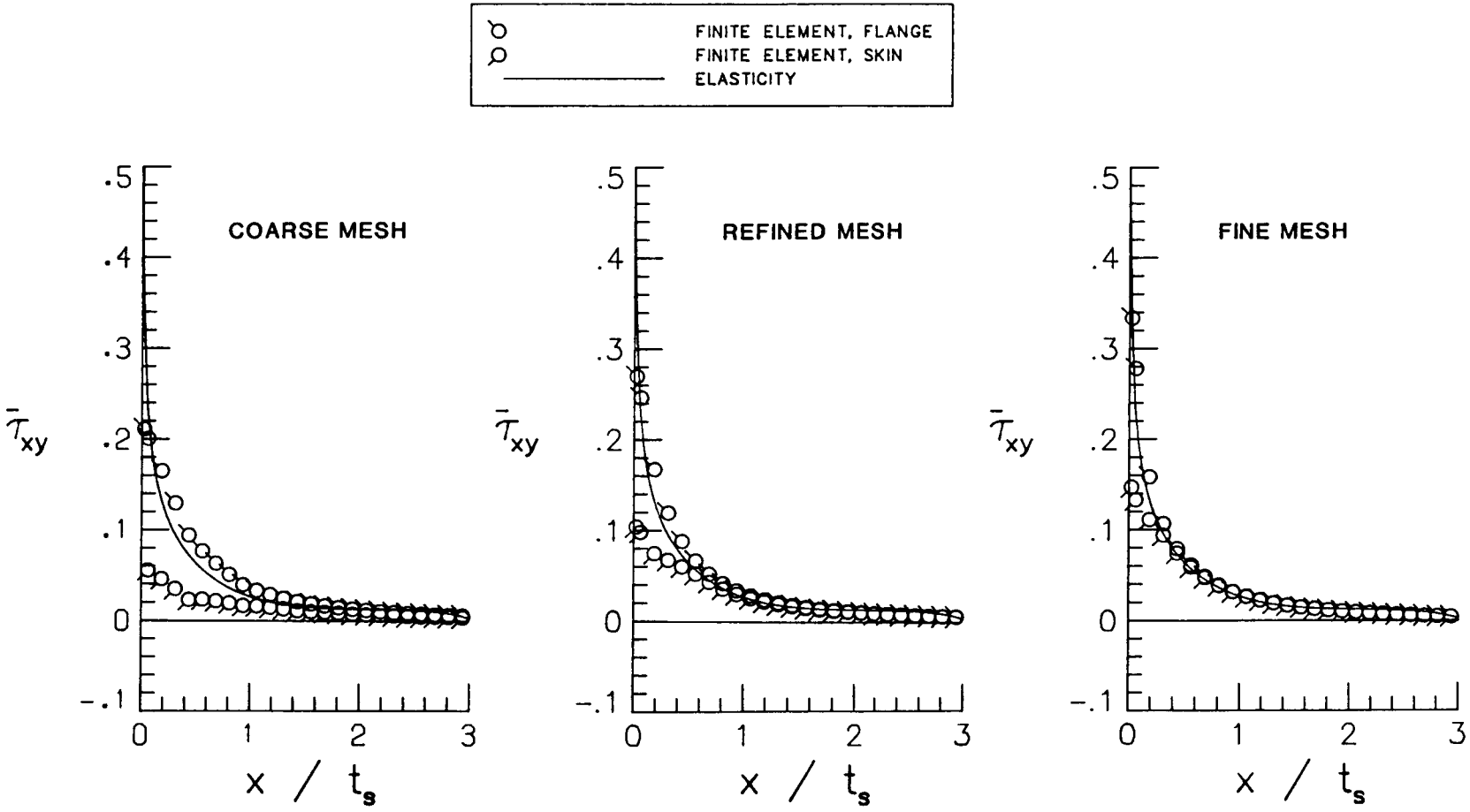

Figure 11. Skin-Stiffener Stress τ_{xy} for 45° Flange Termination Angle, Finite-Element and Elasticity Results Using 15 Eigenvalues and 100 Collocation points.

the inherent inaccuracy of the finite-element data near points of stress singularity. Although the region of inaccuracy shrinks with increases in mesh density near this point, the discrepancy between the two values of stress near the vertex is quite significant. This characteristic occurs for both the 90° and the 45° flange termination angles.

To illustrate that the stresses as computed by the coarse mesh are sufficiently accurate to serve as boundary conditions for the elasticity solution, Figures 12 and 13 illustrate the variation with $\bar{x}$ of the three stresses $\bar{\sigma}_x$, $\bar{\sigma}_y$, and $\bar{\tau}_{xy}$, as generated by the elasticity solution for the two flange geometries. Each figure illustrates the three components of stress and each stress component is represented by three relations, each relation corresponding to the collocation of stress data from the different finite-element meshes. It is immediately evident from the figures that for each stress component for both flange angles, the results of collocating stress data from the three different mesh densities coincide. This indicates that in order to obtain a good approximation of the state of stress in the localized region using the elasticity solution, only the coarse mesh need to be used. This is somewhat expected since at some distance away from the point of singularity the coarse mesh will yield a converged set of stresses. That is, the values of the stresses which were used for collocation on the boundaries CD and EF were approximately the same for all meshes. This supports the computation effectiveness of the current procedure, since only a coarse finite-element mesh is required to produce highly accurate stresses in the localized region. From the figures it is hard to distinguish between the magnitudes of the stresses at $\bar{x} = 0.025$. Hence, the values of $\bar{\sigma}_x$, $\bar{\sigma}_y$, and $\bar{\tau}_{xy}$ at these points, for the three meshes, are given in Table 1. It is observed that the percent difference in these values is negligible, again emphasizing the power of this methodology.

At this point it is appropriate to depart from the discussion of the accuracy of the method and illustrate some of the physical results that can be addressed from the analysis. Table 1 indicates that in terms of the peel stress, the 45° flange termination angle is better than the 90° flange termination angle. At $\bar{x} = 0.025$, the normalized peeling stress is 0.290, while for the 45° angle, the peeling stress is 0.192, 33% less. On the other hand, the shear stress is about

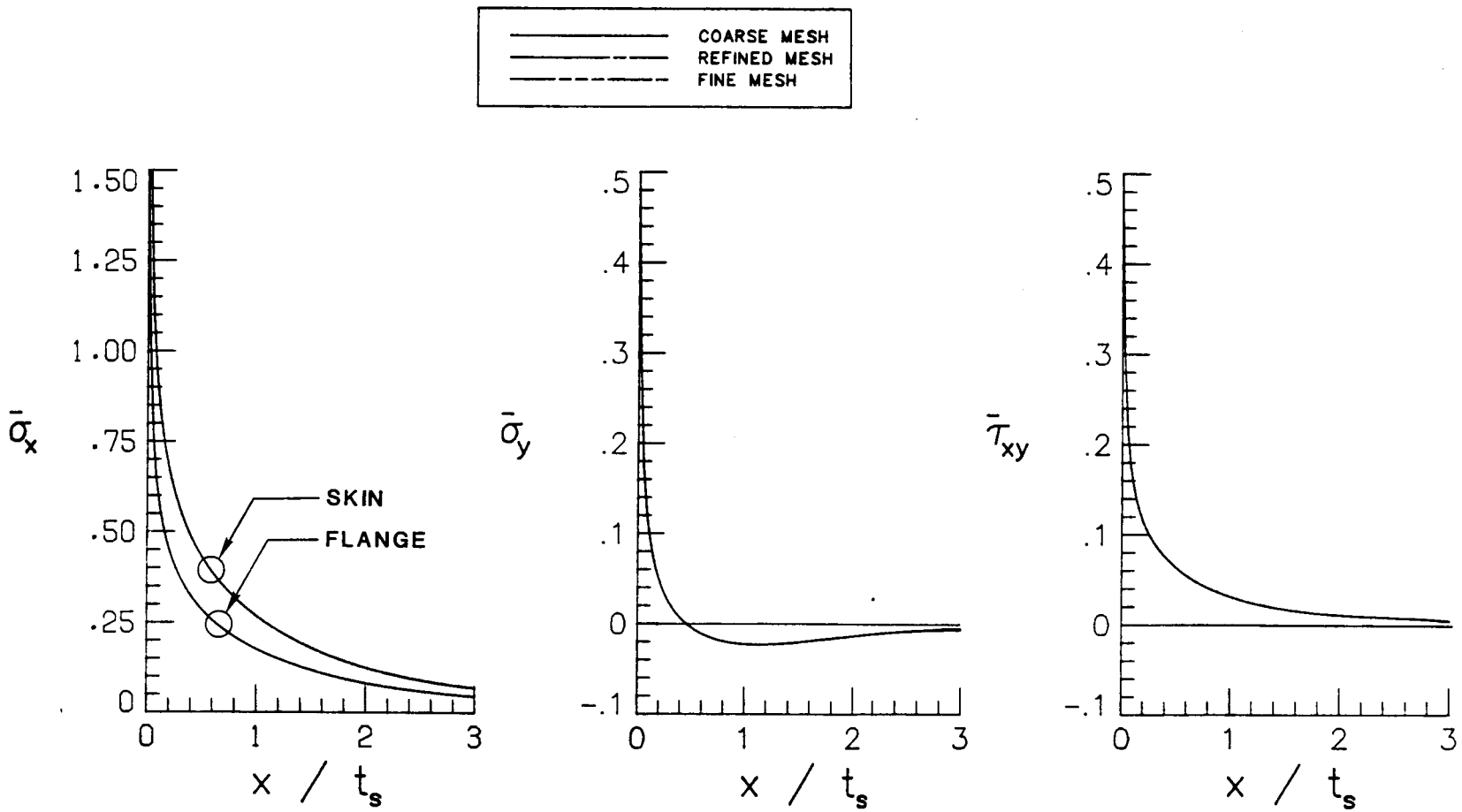

Figure 12. Skin-Stiffener Stresses for 90° Flange Termination Angle Computed From the Elasticity Solution using Three Mesh Refinements, 15 Eigenvalues, and 100 Collocation points.

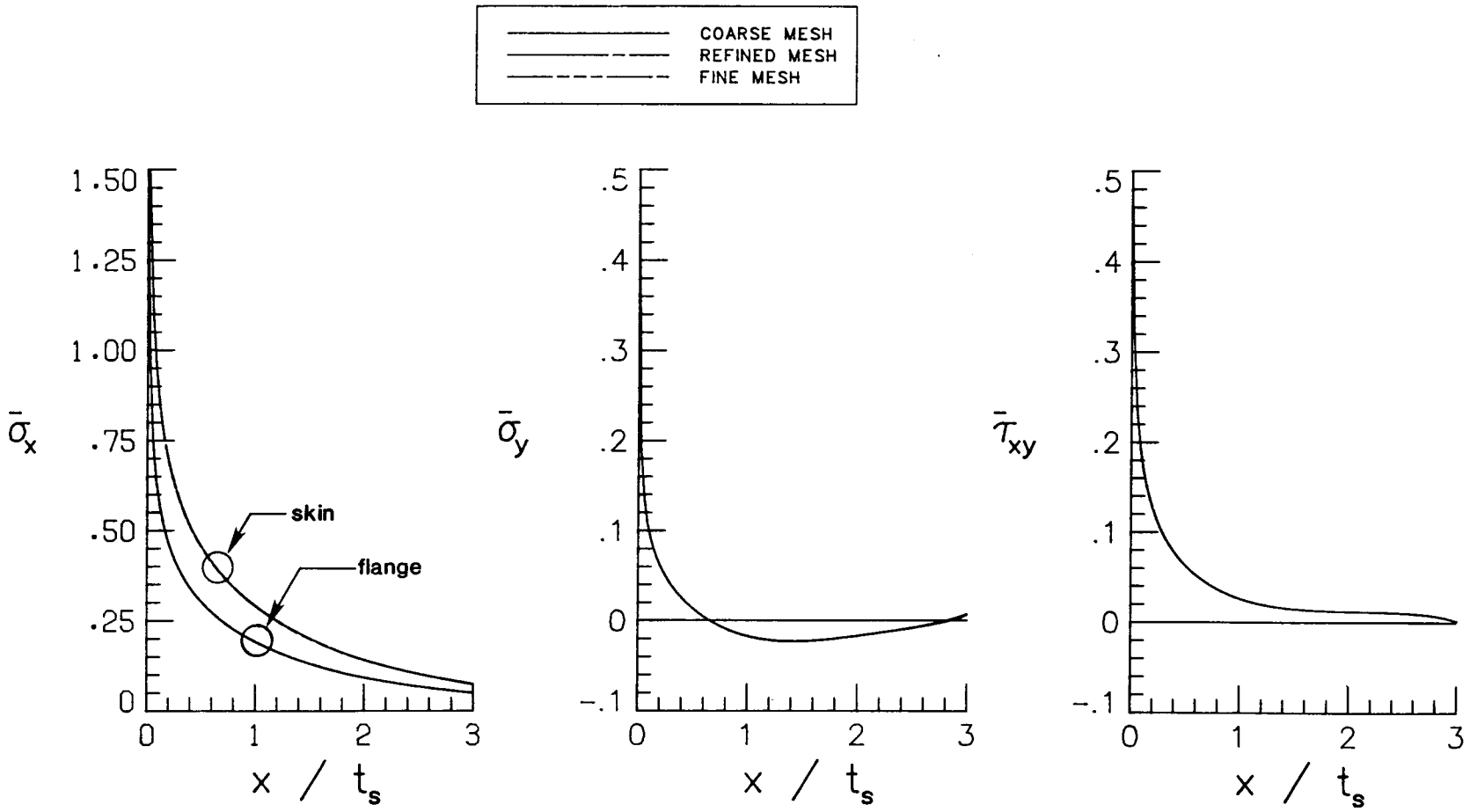

Figure 13. Skin-Stiffener Stresses for 45° Flange Termination Angle Computed From the Elasticity Solution using Three Mesh Refinements, 15 Eigenvalues, and 100 Collocation points.

Table 1. Maximum Stresses at $\bar{x}=0.025$ as Computed from the Elasticity Solution Using Three Finite-Element Mesh Refinements.

90 ° Flange Termination Angle				
Mesh Used For Collocation	$\bar{\sigma}_x$ Flange	$\bar{\sigma}_x$ Skin	$\bar{\sigma}_y$	$\bar{\tau}_{xy}$
Coarse	1.036	1.530	0.290	0.300
Refined	1.039	1.534	0.290	0.301
Fine	1.039	1.534	0.290	0.301
45° Flange Termination Angle				
Mesh Used For Collocation	$\bar{\sigma}_x$ Flange	$\bar{\sigma}_x$ Skin	$\bar{\sigma}_y$	$\bar{\tau}_{xy}$
Coarse	0.968	1.438	0.192	0.319
Refined	0.973	1.446	0.193	0.321
Fine	0.976	1.450	0.193	0.321

the same for the two different flange geometries. On balance, the 45° angle would be better of the two. This coincides with intuition but the methodology developed here allows for the behavior of the two different angles to be quantified.

Next, the issue of the convergence of the truncated eigenfunction expansion, as related to the number of eigenvalues and collocation data points, is addressed. Figures 14 and 15 illustrate the variation with $\bar{x}$ of $\bar{\sigma}_x$, $\bar{\sigma}_y$, and $\bar{\tau}_{xy}$ as computed by the truncated stress functions (eqs. 46 and 47) for 90° and 45° flange termination angles. The multiple data on each plot correspond to stress calculations produced by 5, 10 and 15 eigenvalues in the truncated eigenfunctions. In these computations 100 collocation points from the coarse mesh were used. As can be seen in the figures, convergence of the truncated stress functions for $\bar{\sigma}_y$ and $\bar{\tau}_{xy}$ occurs between 10 and 15 eigenvalues. That is, the stress computation for 15 eigenvalues is bracketed between the computation for 5 eigenvalues and the computation for 10 eigenvalues. On the other hand, this convergence is not completely evident for $\bar{\sigma}_x$. There seems to be a slight increase in this stress value with an increasing number of eigenvalues. There does not seem to be a bracketing effect with increases in the number of eigenvalues, as was observed for the other stress components. However, on a percentage basis, the increase of stress is minimal. Hence it is felt that the use of between 10 to 15 eigenvalues leads to convergence of the eigenfunctions in eqs. 46 and 47. Figures 16 and 17 illustrate data for the same stress components in which the number of collocation points were varied. In particular, the number of collocation points was doubled. For these computations 15 eigenvalues and a coarse mesh were used in the stress computations. From Figures 16 and 17 it is apparent that the number of collocation points has a minimal (or no) effect. This is true provided that the number of collocation points are approximately 3 to 4 times larger than the number of coefficients in the truncated eigenfunctions. It should be noted that the number of collocation points for the 90° flange termination angle, Figure 16, is different than the number of collocation points for the 45° flange geometry, Figure 17, because of slight differences in geometry.

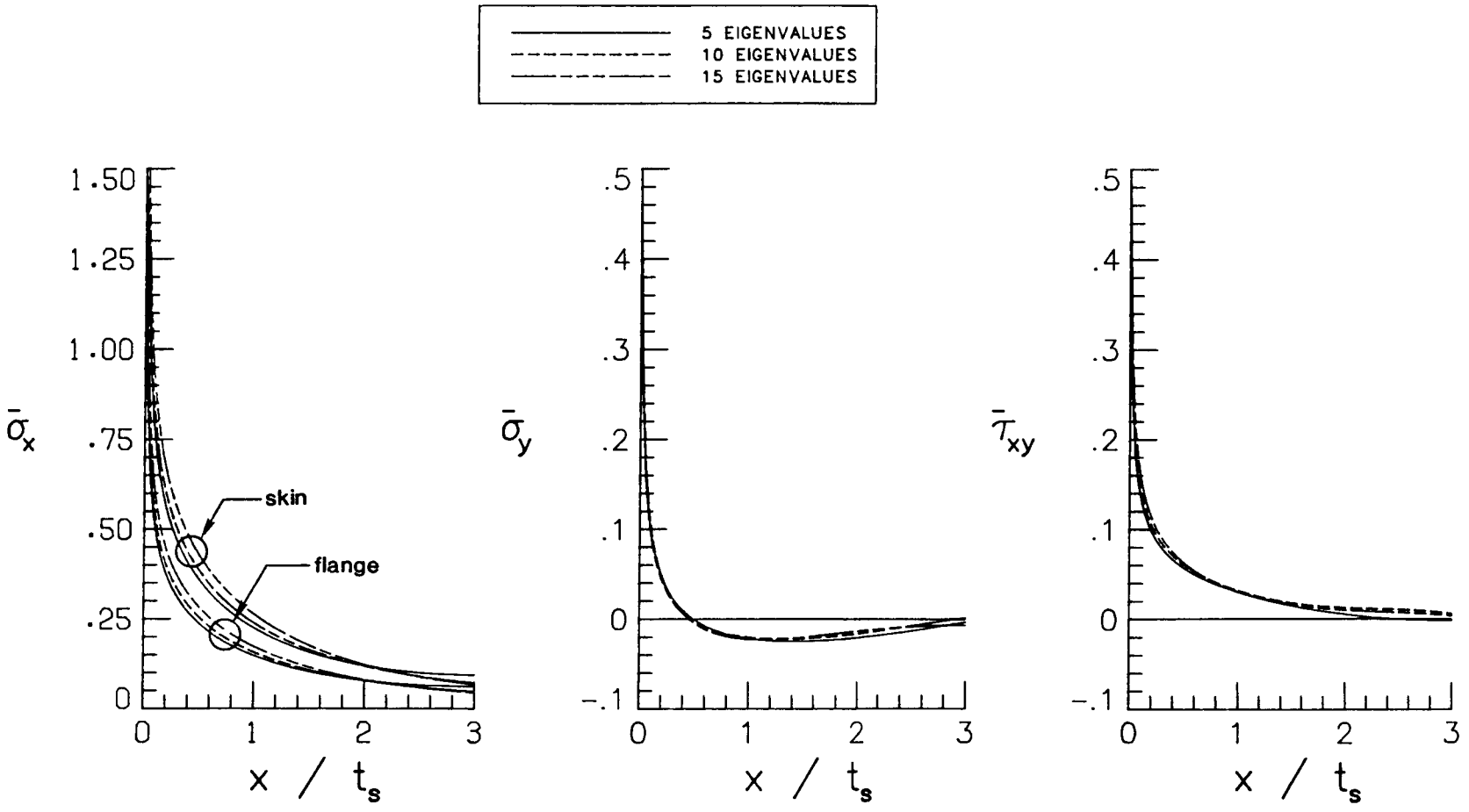

Figure 14. Elasticity Solution of Skin-Stiffener Stresses for 90° Flange Termination Angle as Function of the Number Eigenvalues Using 100 Collocation points.

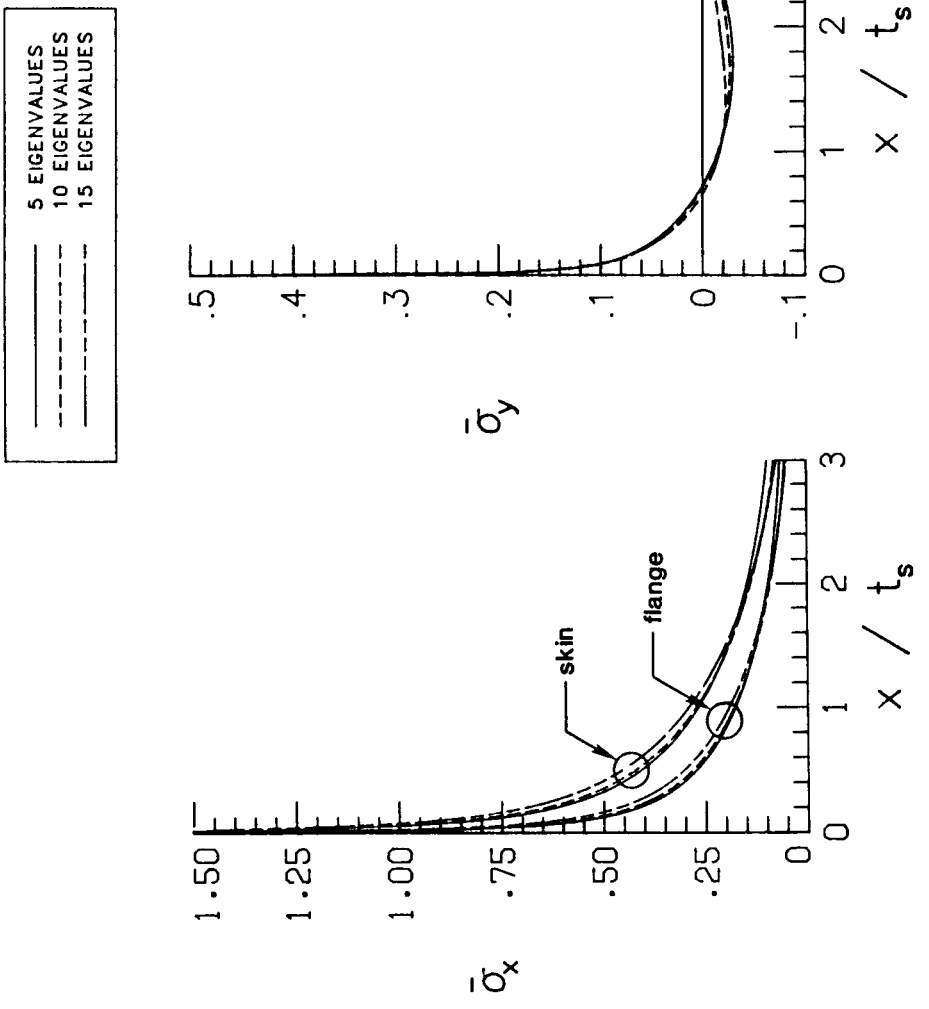

Figure 15. Elasticity Solution of Skin-Stiffener Stresses for 45° Flange Termination Angle as Function of the Number Eigenvalues Using 100 Collocation points.

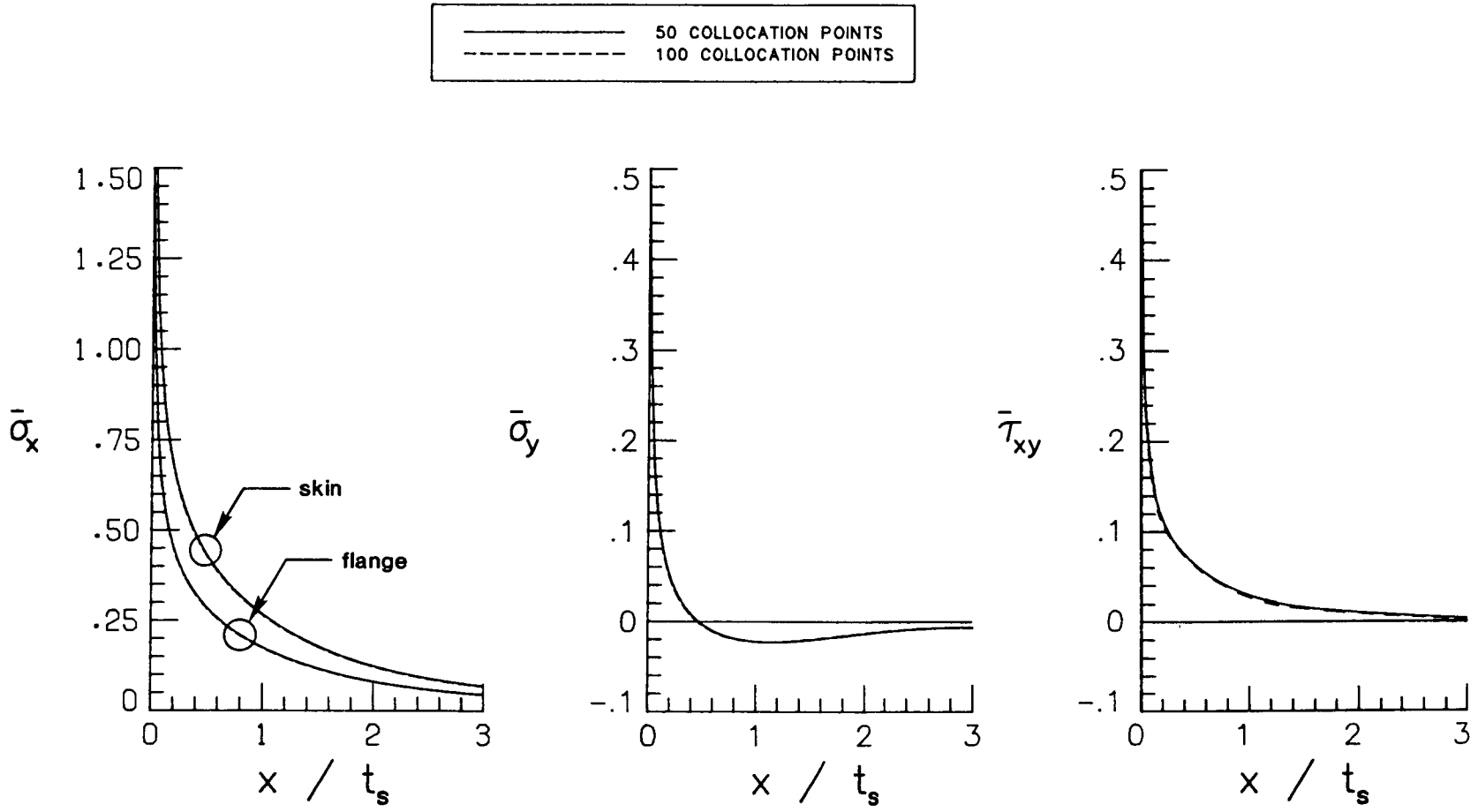

Figure 16. Elasticity Solution of Skin-Stiffener Stresses for 90° Flange Termination Angle as Function of the Number Collocation points Using 15 Eigenvalues.

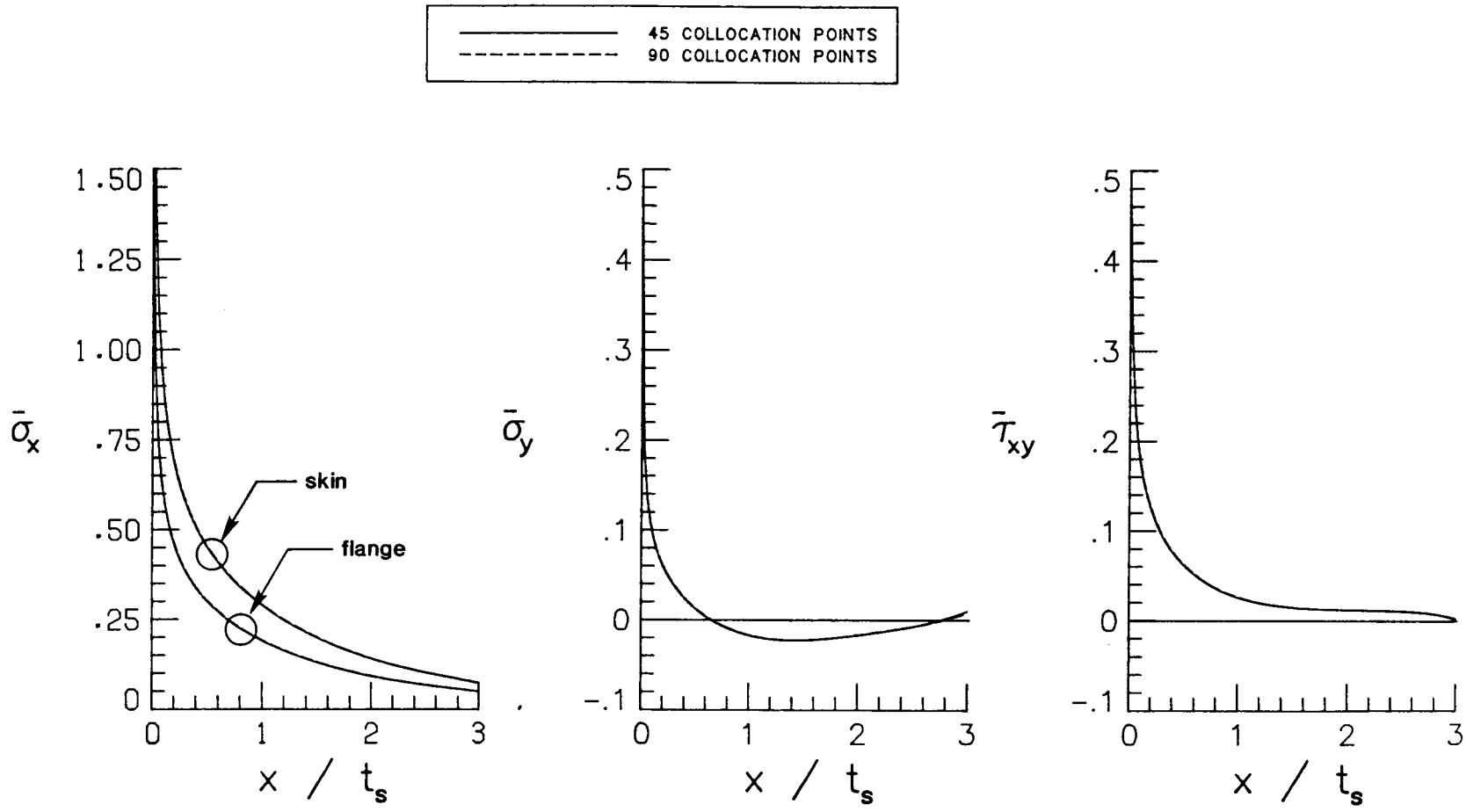

Figure 17. Elasticity Solution of Skin-Stiffener Stresses for 45° Flange Termination Angle as Function of the Number Collocation points Using 15 Eigenvalues.

Next a point of computational importance is addressed. In the course of the investigation it has been found that the stresses on contour ABCDEFA, more specifically the stresses on CD and EF, as computed by the finite-element analysis, are practically independent of the flange termination angle. Thus the stress data from the finite-element analysis of the cross-section with a flange termination angle of 90° can be used as collocation data for the elasticity analysis of a 45° flange termination angle, or any other angle for that matter. Hence, the finite-element analysis need to be done only once. This reduces the computation task, since the one finite-element analysis can be used to produce multiple local elasticity solutions for different flange termination angles. Figure 18 shows results of two elasticity solutions of the 90° flange termination angle. In one solution the finite-element data from the analysis of a cross-section with a 90° termination angle and the eigenvalue expansion solution for the 90° flange angle are used. In the other solution the finite-element data from the analysis of the cross-section with a 45° termination angle and the eigenvalue expansion for the 90° angle are used. Of course the former solution is the one that is correct but it is clear from the figure that the latter solution is essentially identical to the former. Figure 19 shows the solution for 45° flange termination angle solved using both 90° and 45° finite-element analyses as the bases for the collocation procedure. Again it is obvious there is very little difference in the results, indicating that the eigenvalues and eigenvectors play a very important rule in determining the characteristic of the stress distribution in the local region.

It is appropriate at this time to address an issue that is often raised in conjunction with the study of interface stresses. The point is raised now because it will put into context the results to be presented in the remainder of this document. The analysis developed to this point has assumed that the skin and the flange are joined along a line that represents a perfect bond with zero thickness. Depending on the fabrication process, the bond line may have nonzero thickness and the material within this thickness may have properties significantly different than either the skin or the flange materials. At issue is the fact that the interface between the flange and the skin may be an adhesive with nonzero thickness. Of concern is the influence

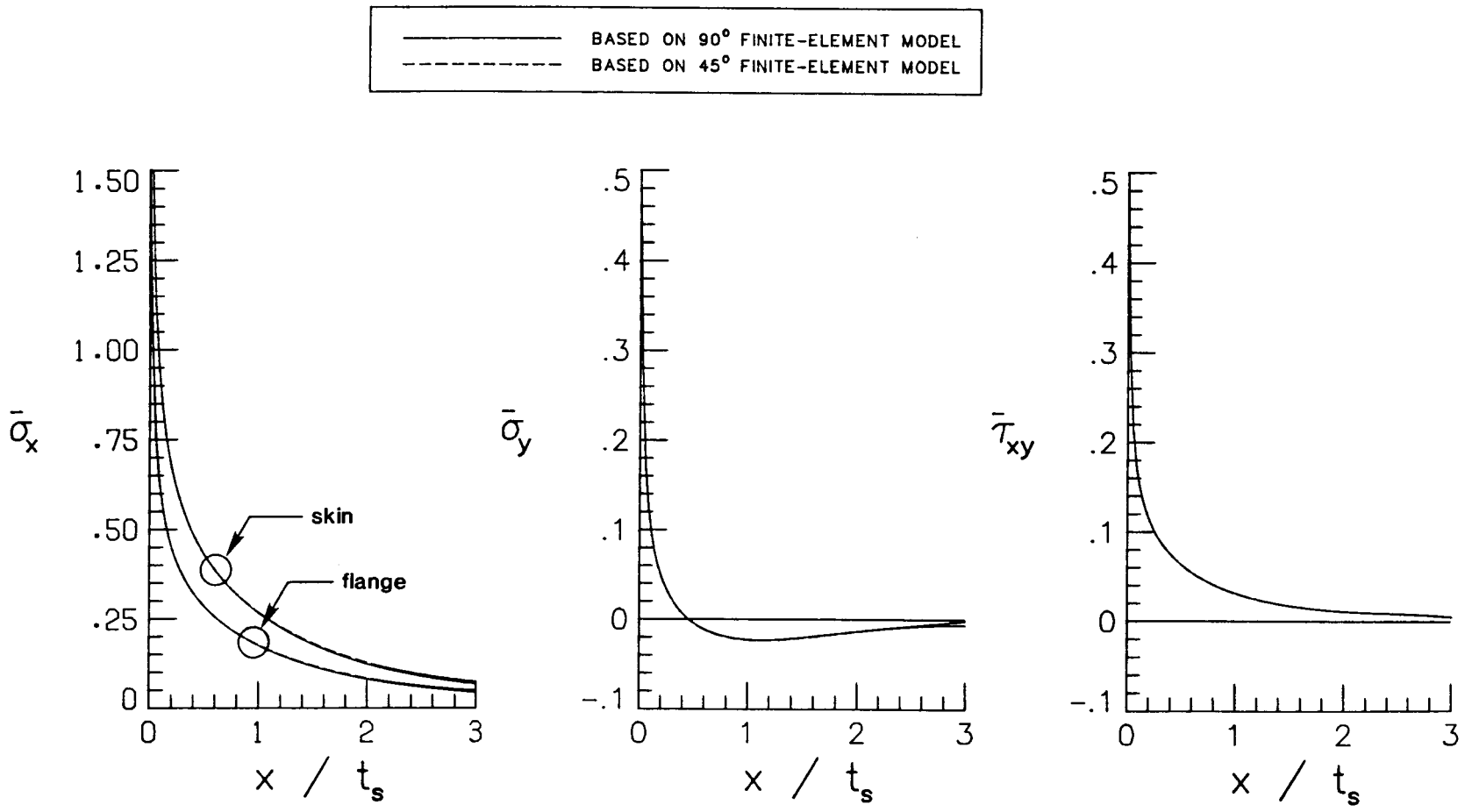

Figure 18. Skin-Stiffener Stresses for 90° Flange Termination Angle Using Boundary Data From the Finite-Element Analysis of a 90° and 45° Flange Termination Angles.

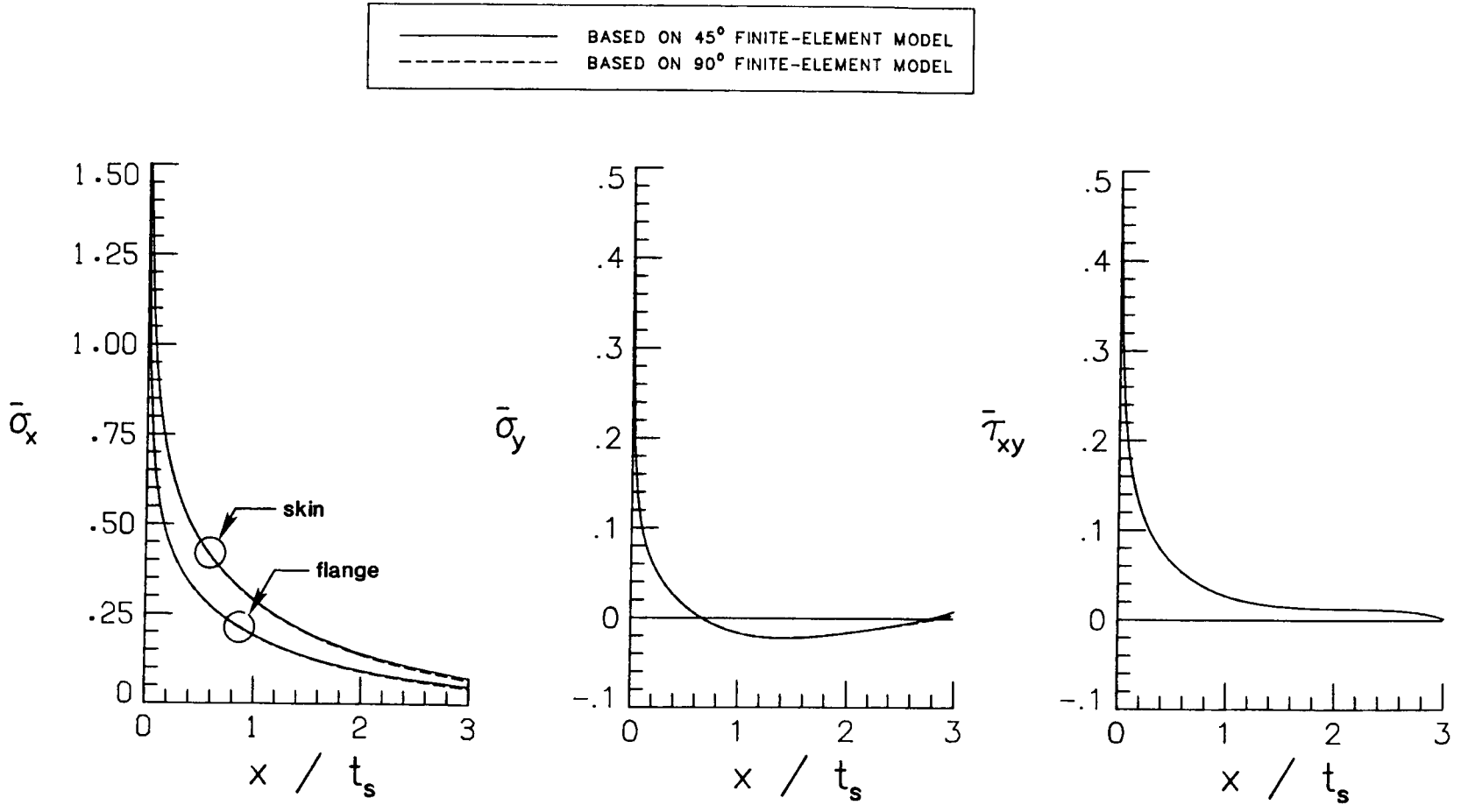

Figure 19. Skin-Stiffener Stresses for 45° Flange Termination Angle Using Boundary Data From the Finite-Element Analysis of a 90° and 45° Flange Termination Angles.

of the adhesive layer on the peeling and shearing stresses. In what follows, the interface stresses are computed using finite-element analyses for two adhesive layer thicknesses. These results are compared to results for the case for which a zero bond line thickness is assumed. The data presented provide important information as to whether the elasticity solution is conservative or nonconservative in the calculation of skin-stiffener interface stresses when an adhesive layer is present. One may postulate that an elasticity solution in which the two adherents are assumed to have a perfect bond of zero thickness will lead to nonconservative stress calculations. This is a consequence of the fact that the assumption of perfect bond reduces the flexibility of the interface, as compared to if the adhesive layer was present. Hence it is important to know how large an error is introduced as a consequence of the assumption made. To determine this effect, the same skin-stiffener geometry and loading conditions which are shown in Figure 4 are analysed. Two adhesive layer thicknesses are evaluated, $\frac{h}{t_s} = 0.05$ and $\frac{h}{t_s} = 0.10$. The thicker adhesive layer represents the upper limit of the bond line thickness. The thinner layer thickness is the nominal bond line thickness. The results from these analyses are compared to stress data for $\frac{h}{t_s} = 0$ layer thickness as computed by the finite-element program and as computed by the local elasticity analysis. The adhesive material properties are given in Appendix D. Mesh refinement in the localized region corresponds to the fine mesh of Figure 4.c. A coarser mesh is used outside the local region. However, element size in the coarse region is such that the adhesive elements' aspect ratio does not exceed 1:4. Figure 20 shows the character of the interface peeling stress σ_y in the localized region. Figure 21 displays similar information for the interface shearing stress τ_{xy}. Each figure consists of two plots, one illustrating the stresses at the interface as computed by elements in the flange, and the other illustrating the same stresses but evaluated by elements in the skin. The finite-element stress data is denoted by symbols, whereas, the local elasticity results are indicated as solid curves. As in previous figures the stresses and distance along the interface have been normalized.

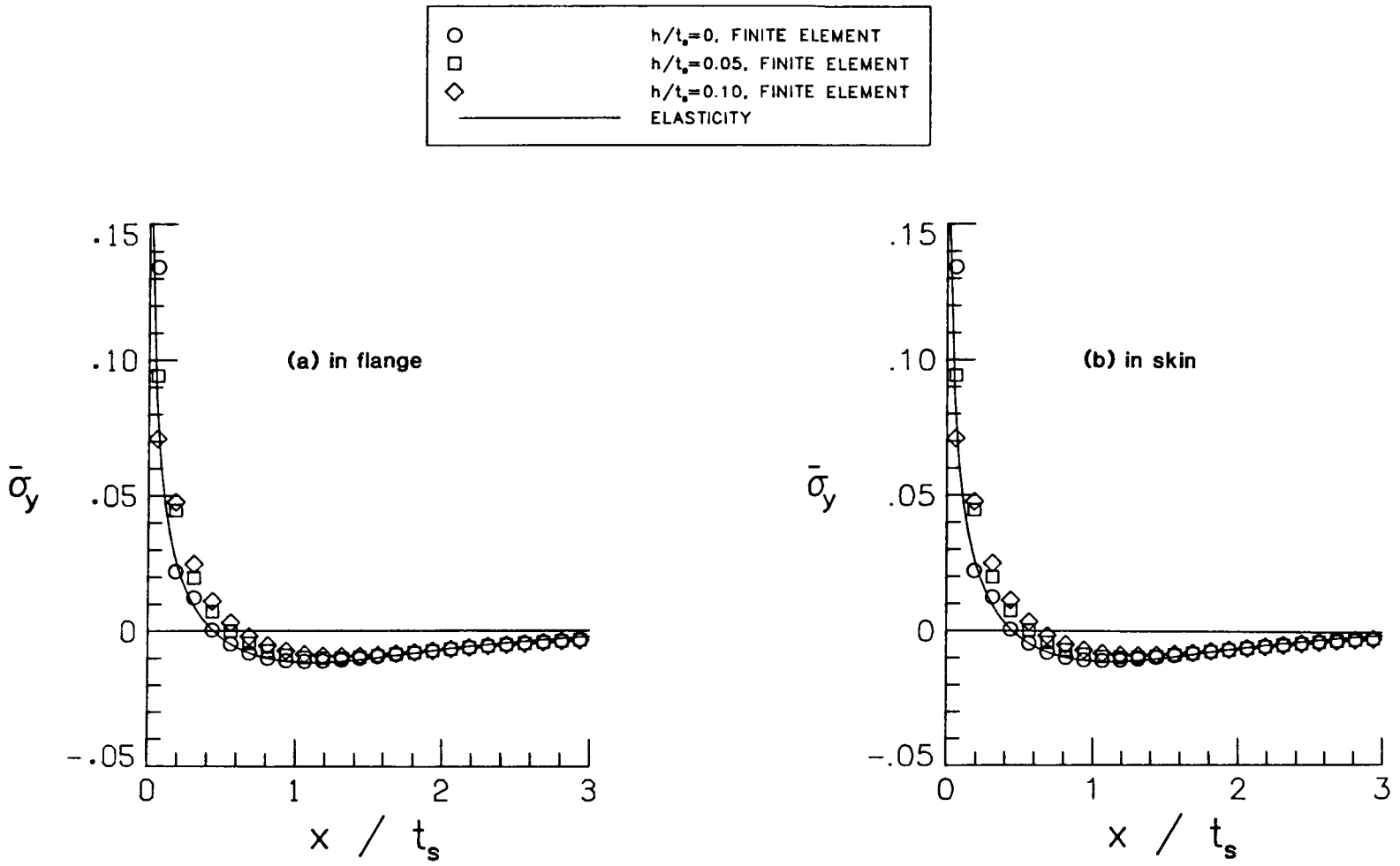

Figure 20. **Skin-Stiffener Interface Peeling Stress, σ_y, Throughout the Flange Termination Region as a Function of Adhesive Thickness.**

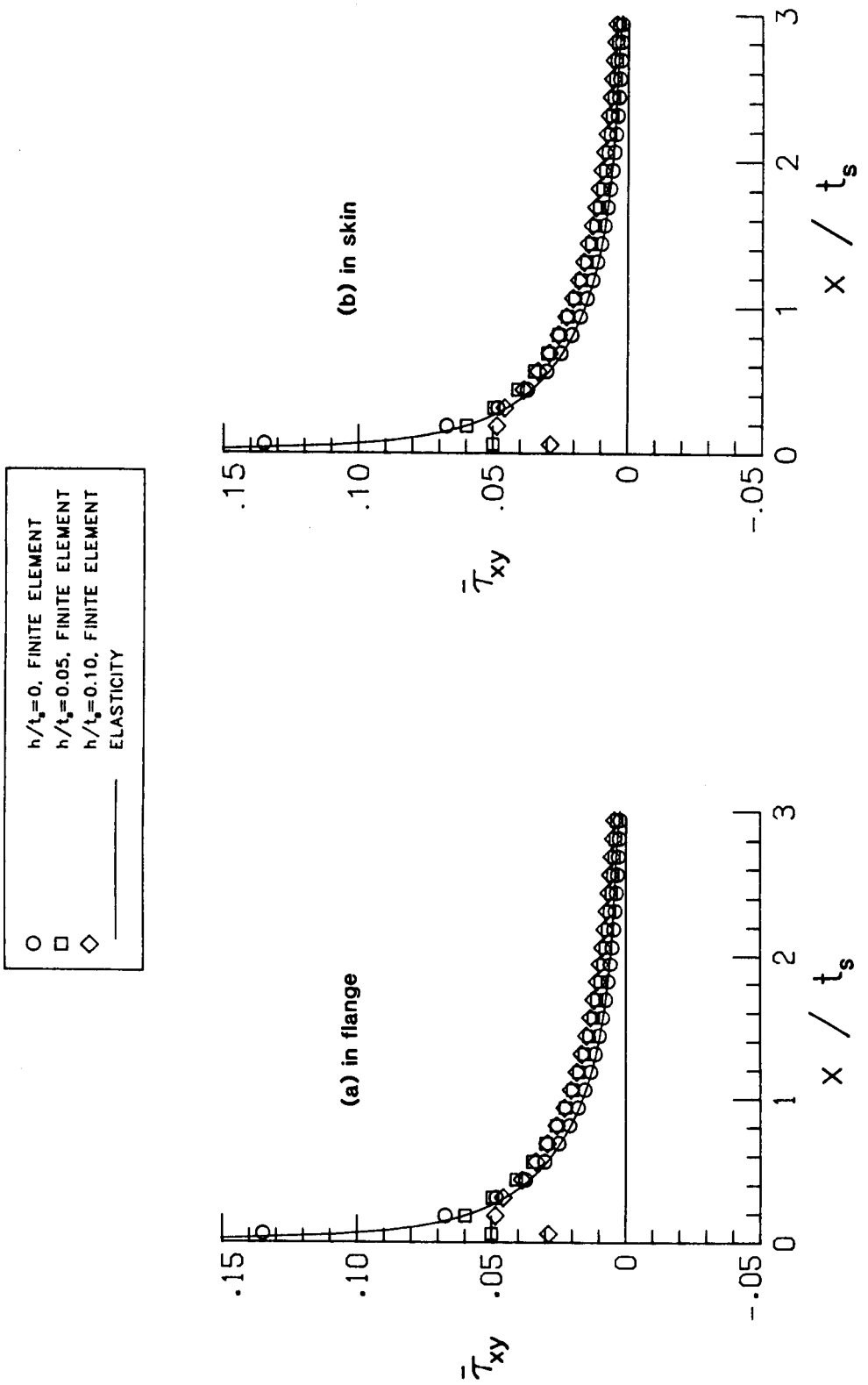

Figure 21. Skin-Stiffener Interface Shearing Stress, τ_{xy}, Throughout the Flange Termination Region as a Function of Adhesive Thickness.

In general, the results of Figure 20 suggest that there is a slight increase in the magnitude of the peeling stress, σ_y , between $\bar{x} = 0.025$ to $\bar{x} = 1$ as the bond line thickness increases. However, the increase relative to the zero bond line results is quite small, something on the order of less than 5%. In general, the results of Figure 20 indicate that even in the present of adhesive layer, the peel stresses tend to become unbounded as the flange terminus is approached. The unbounded nature of the peel stress with an adhesive is in qualitative agreement with the finding of [9]. The conclusions regarding the behavior of the shear stress are not so clear. As has been shown in Figures 8 and 11, the elasticity solution and the finite-element results for zero thickness bond line are in disagreement near the flange termination point. Further, the finite-element shear stress results in the skin and in the flange at the interface near the flange terminus are markedly different from each other. This essentially indicates that the finite-element solution is not converged at this location. However, with the adhesive present, the finite-element stress calculation for the shear stress in the flange are not that different than the calculation for shear stress in the skin. Has the finite-element solution converged and the shear stress is indeed finite and may be less than the zero bond line case ?. Reference [9] indicates that the shear stress is also quite large near the flange termination point. This finding, coupled with what appears to be the poor shear response of the 8-node finite-element for this class of problems would lead to the conclusion that the shear stresses are unbounded near the flange termination point, even in the present of an adhesive layer. Hence, it is felt that the peeling and shearing stresses computed by the elasticity solution for the case of zero bond line thickness are representative of the behavior, even in the present of nonzero bond line thickness.

Attention is now focused on extending the methodology to include geometric nonlinearities, and to study the influence of stiffener geometry and material properties on interface stresses.

3. Application of the Methodology to Stiffened Composite Plates

3.1 Preliminary Remarks

If the cross-section being studied is actually part of a plate which is subjected to a particular loading and boundary conditions, the cross-section experiences a loading more complicated than the simple bending moment used in studying accuracy and convergence. In addition, the loading is most certainly of such a magnitude that the plate experiences geometrically non-linear effects. Thus, to extend the present work to the analysis of stiffened plates with realistic loading and boundary conditions, the cross-section geometry being consider is assumed to be part of a pressure-loaded plate which is clamped on all four sides. The particular plate geometry and boundary condition were chosen since they represent the configuration studied experimentally in [10] and, as shown in Figure 22, the situation simulates a unit cell of stiffened aircraft skin structure. Although in actual aircraft structures the skin is generally subjected to both transverse pressure and inplane loading, only a pressure load is investigated. In that

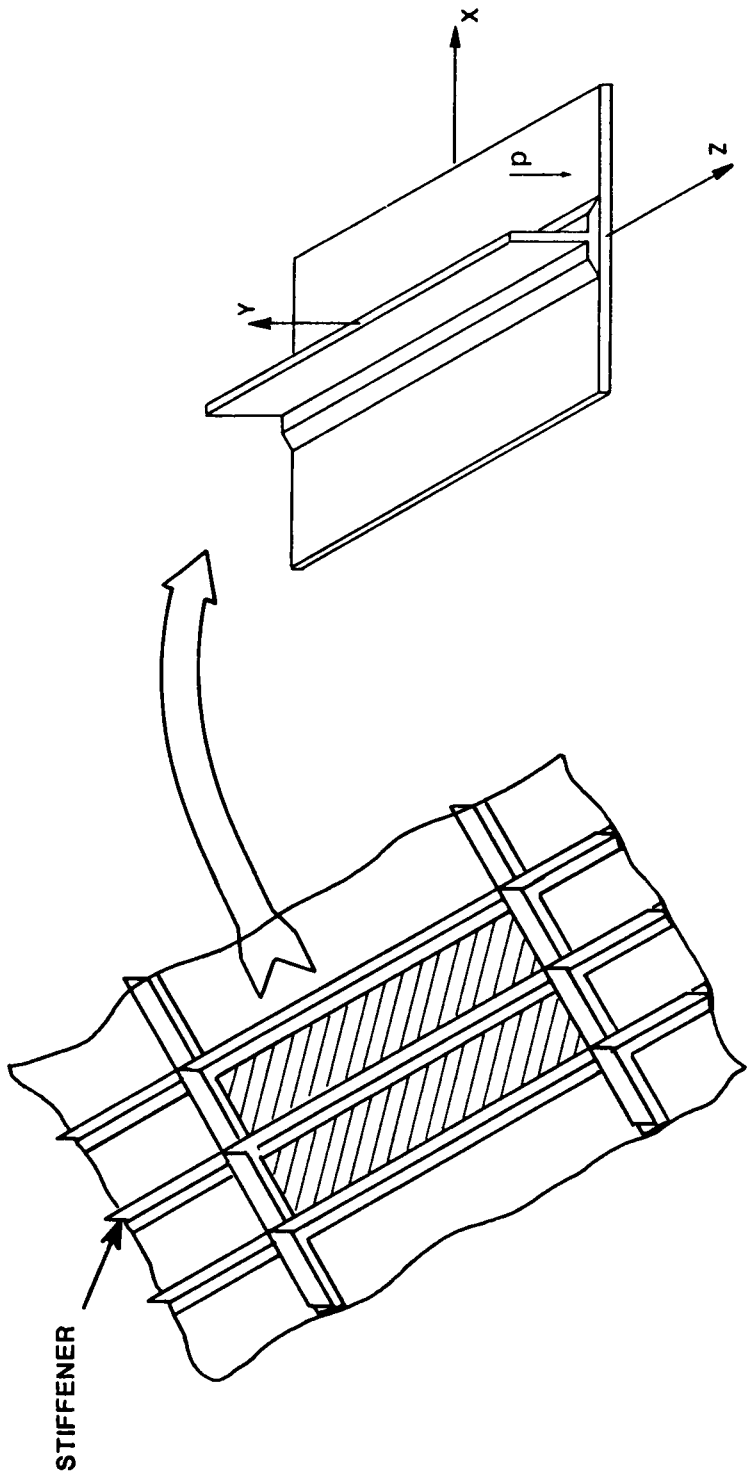

Figure 22. Single Stiffener Plate Geometry.

context it should be mentioned that the methodology can be extended to include more general loadings and stiffener geometries. In the present investigation a coordinate system different than the one commonly use by plate theory was chosen (see Figure 22). This was done in order to keep the coordinate system consistence with the elasticity solution developed earlier. Although, this may lead to some confusion, it was felt that the plate analysis (herein called the structural analysis) had only sideline importance in the present development, the elasticity analysis being the principal analysis.

The analysis procedure to be discussed consists of three steps. First, a two-dimensional structural level analysis of the entire stiffened composite plate is conducted. Next, a typical cross-section in the central region of the stiffened plate structure is isolated and a three-dimensional finite-element analysis of the cross-section is performed. The boundary conditions for this three-dimensional model are provided by the structural level analysis. Hereafter, the finite-element analysis of the stiffener-skin cross-section is alluded to as the substructural analysis. In the previous chapter this type of analysis was referred to as global analysis. Here, it is felt that since the stiffened-skin cross-sectional analysis is a subset of the structural level analysis, this terminology is more appropriate. Finally, the stresses from the substructural analysis are coupled with boundary collocation scheme to produce a rigorous elasticity solution in the flange termination region, i.e., the localized region. The scheme thus may be termed as a structure-substructure-local analysis. Both the structural and substructural analyses were conducted using the commercially available Engineering Analysis Language (EAL) finite-element code [40]. Before proceeding to discuss the structure-substructure-local analysis model, the extension of the elasticity solution to account for geometric nonlinearities is considered.

3.2 Geometrically Nonlinear Elasticity Analysis

Since stiffened composite aircraft skin structures are generally designed to operate in the postbuckling or geometrically nonlinear range, this characteristic must be considered. Despite the geometrically nonlinear deformations, it can be assumed that the strains are small and hence linear elastic material response will prevail. In addition, for a thin flexible structure, such as a stiffened composite plate, it is customary to assume that the inplane deformations, u and w, are much smaller than the plate dimensions in x and z directions, whereas, the out-of-plane deformation, v, can be of the same order of magnitude as the plate thickness. The above assumptions lead to neglecting all nonlinear terms in the strain-displacement relations which contain the derivatives of $\hat{u}$ and $\hat{w}$ ($\hat{}$ indicates inplane displacement of the plate midsurface). In addition, if it is assumed that a line perpendicular to the midsurface remains perpendicular and unstrained after deformation, then one arrives at the well-known Von Karman plate kinematic relations.

The extension of the geometrically linear elasticity solution previously developed to the geometrically nonlinear range relies on (for the problem studied here) the assumption of small strains and small to moderate angular rotations, ω_x and ω_z, about the x and z axes. In addition, it is required that these rotations are independent of spatial location within the localized region. Under these assumptions the stress equilibrium equations written in the deformed body coordinates are satisfied by the stress function relations, eqs. 15.a through 15.c, written in the same coordinate systems. To facilitate our understanding as to why such a statement can be made, a brief discussion of the general nonlinear stress equilibrium conditions follows. For a detailed discussion of the subject the reader is referred to Novozhilov, [41].

In the geometrically nonlinear range the equilibrium equations are derived by summing forces on an infinitesimal element in the deformed state. For the purposes of the analytical

development, it is sufficient to concentrate on the geometric representation of a body undergoing small strains and small to moderate rotations. In the case of small straining, the infinitesimal element shape in the deformed state may be approximated by its original undeformed shape. In addition, the x-y-z coordinate system will be transformed into a rectangular cartesian system, $\tilde{x}$-$\tilde{y}$-$\tilde{z}$, in the deformed body, as shown by Figure 23.

In the skin-stiffener nonlinear analysis context, the following assumptions are made:

(a) The condition of small strains exists in the localized region and linear elastic material response is obeyed.

(b) The condition of small to moderate rotations exists and these rotations are independent of spatial location within the localized region.

Under the above considerations, the localized skin-stiffener region in its original shape undergoes rigid-body rotations as shown in exaggerated form in Figure 23.a. Since $\tilde{x}$-$\tilde{y}$-$\tilde{z}$, is a rectangular cartesian system, the equilibrium equations can be written in the deformed state by adding tildes over x,y and z. Hence, the elasticity solution developed previously is assumed to be valid, provided that it is applied in the deformed body state and that the angular rotations are spatially uniform within the region of its application. The procedure outlined previously for the determination of the coefficients, c_n and c'_n in the eigenfunction expansion, eqs. 46 and 47, is then valid provided it is performed in the deformed body state.

3.3 Structural-Substructural-Local Analysis Procedure.

The structure-substructure-local analysis procedure is depicted by Figure 24. First, a structural analysis of the entire blade-stiffened plate (Figure 24.a) is conducted using plate elements. Next, a substructural analysis of an isolated region, where skin-stiffener interface

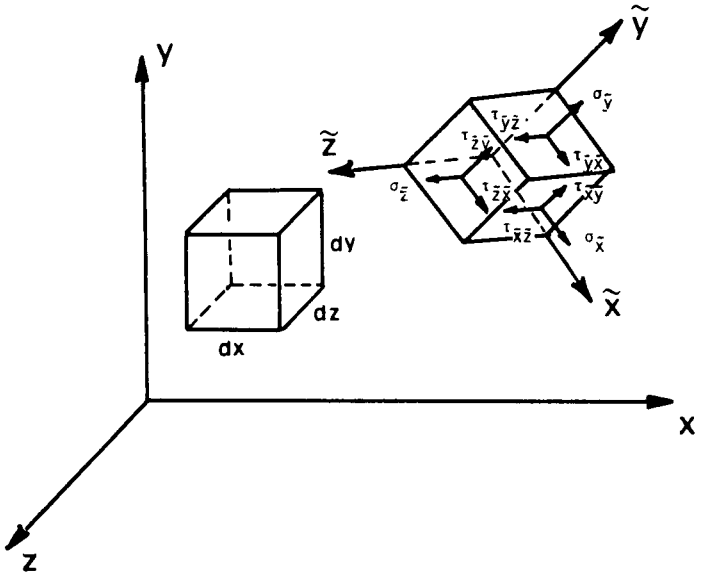

(a) Finite Rotation Infinitesimal Body Geometry.

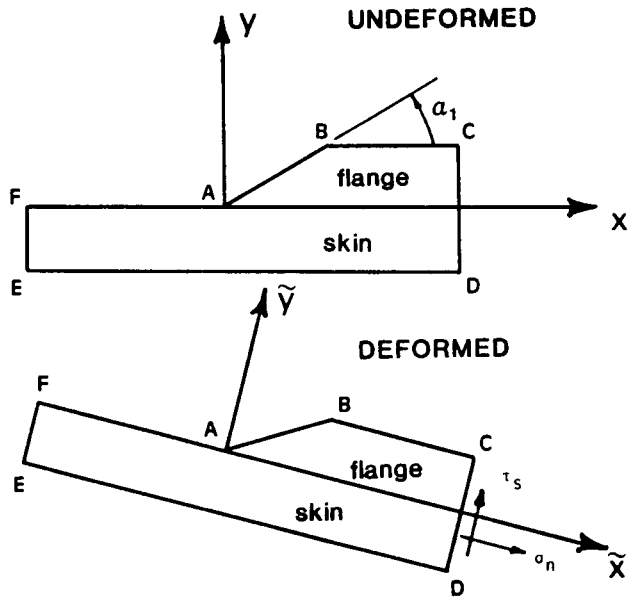

(b) Finite Rotation of the Skin-Stiffener Local Region.

Figure 23. Nonlinear Skin-Stiffener Analysis Geometry.

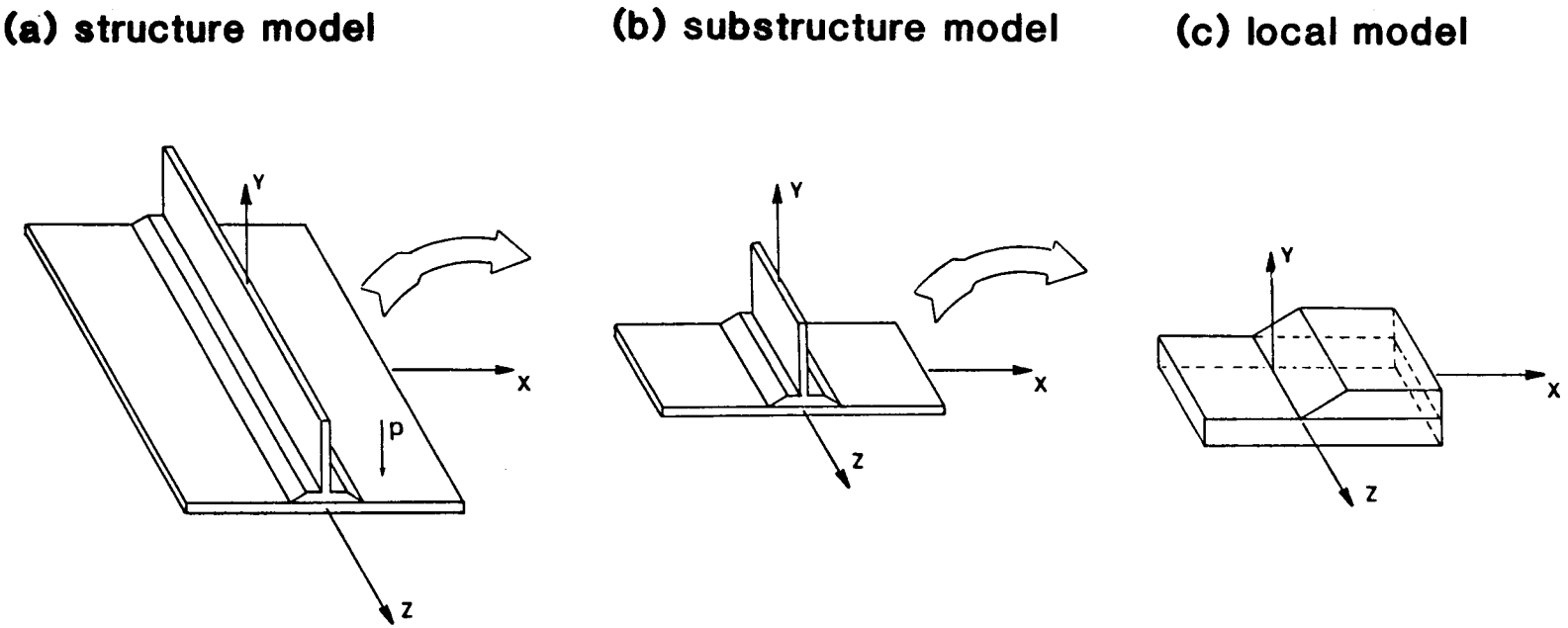

Figure 24. Structure - Substructure - Local Analysis Procedure.

stresses are expected to be high, is performed (Figure 24.b). Finally, a local elasticity analysis of the flange termination region is performed (Figure 24.c).

The structural finite-element model uses plane stress membrane and bending plate elements. The substructure finite-element model employs three-dimensional brick elements. All of these elements are available in EAL. Using these elements, both linear and nonlinear analyses can be performed. The nonlinear solution algorithm used by EAL employes the full or the modified Newton-Raphson method. In the present investigation the full Newton method was used. Most of the elements in the EAL library (and all of the ones used here) are based on Pian's [42] hybrid element formulation derived according to the minimum complementary energy principle. In general terms, this formulation assumes a stress field (generally in polynomial form) which satisfies stress equilibrium in the element interior. The displacements along the element boundaries are expressed in terms of compatible generalized nodal displacements, in a manner identical to the one used in displacement formulation finite-element development. Next, using the principle of minimum complimentary energy, the element stiffness matrix can be constructed. For a detailed discussion of this method see [42] and Appendix C. In the next sections each step of the analysis procedure is discussed.

3.3.1 Structural Analysis

3.3.1.a Details of Finite-Element Analysis

The stiffened plate is discretized using 4-node plate elements, referred to as the E43 element in EAL, as shown in Figure 25. Each element of this type has 5 degrees of freedom namely;

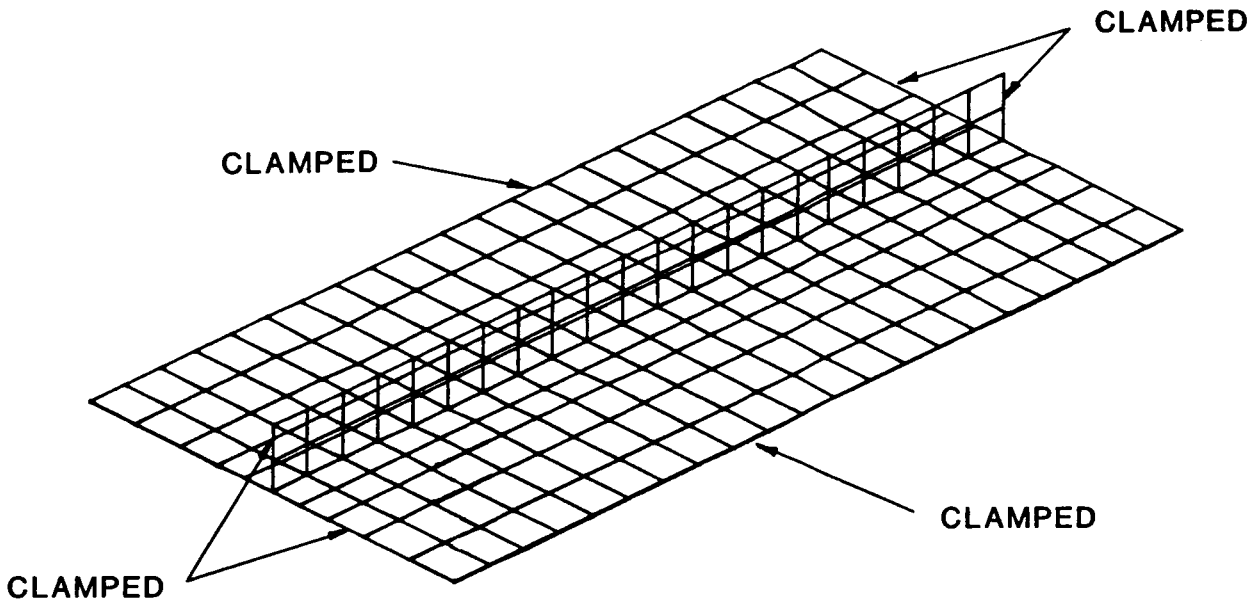

Figure 25. EAL Finite-Element Discretization of a Stiffened Plate Configuration.

To verify of the structural analysis procedure and the accuracy of the EAL finite-element model, a stiffened plate configuration which was tested and analysed in [10] was reanalyzed using EAL, E43 elements. In [10] the STAGS finite-element model was used in the analysis of the plate. The stiffened-plate finite-element discretization used was similar to the one shown in Figure 25. The comparison between the EAL analysis, the STAGS analysis, and the experimental data is shown in Figure 26. In the figure the out-of-plane deflection, at the center-of-plate and in the skin away from the center of the plate, are plotted as a function of the applied pressure. Both the results from STAGS and from EAL are based on geometrically nonlinear analyses. The figure clearly show that the two finite-element methods give nearly identical results. For an explanation of the difference between the experimental data and the analytical results, the reader is referred to [10]. Results like the one displayed in Figure 26 provide confidence in the accuracy of the EAL structural analysis model used in the present investigation.

3.3.1.b Details of Structural Analysis

To be consistent with the constitutive law used in the elasticity solution, in the structural level analysis all extension and bending-twist coupling terms are set to zero. These terms include B_{16}, B_{26}, D_{16}, and D_{26}. For symmetric balanced laminates, such as the ones considered here, $B_{16} = B_{26} = 0$ for both the skin and the flange. On the other hand, neither D_{16} nor D_{26} are zero. However, they tend to be small relative to D_{11}, D_{12}, D_{22}, and D_{66}. Given these material restrictions, and the geometry, and loading conditions considered, it was only necessary to analyse one-quarter of the plate using the two planes of symmetry (i.e., [x,y,0] and [0,y,z]).

Before proceeding, an important point must be raised. The elasticity analysis of the flange termination region relies on the assumption that the stresses do not vary with the z coordi-

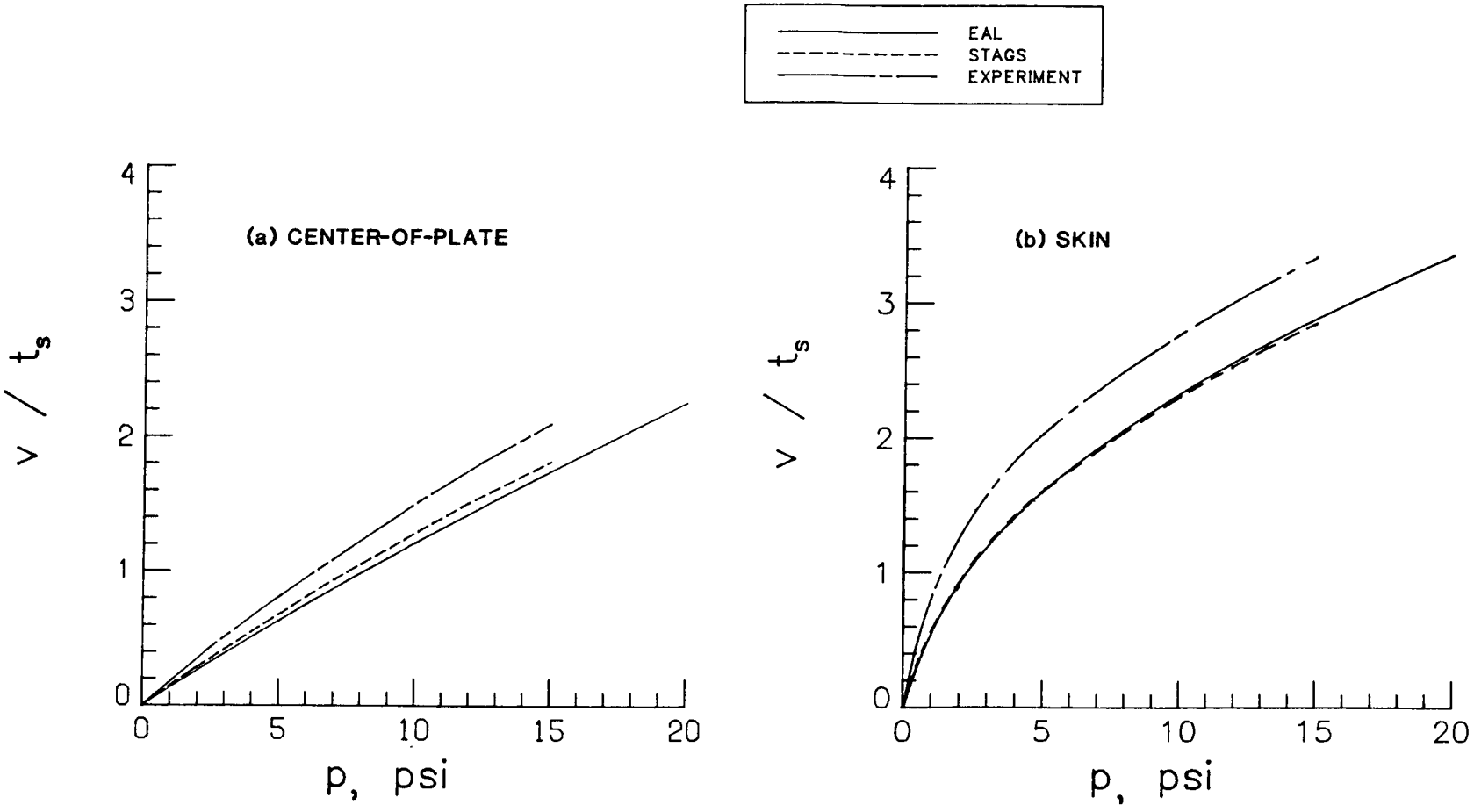

Figure 26. Out-of-Plane Deformation, EAL, STAGS, and Experimental Results (STAGS and Experimental Results are From [10]).

nate, i.e., the stiffener direction. The stresses in a stiffened plate which is clamped on all four sides clearly vary with the z coordinate, particular near the ends of the stiffener. However, toward the center of the plate there will be a region within which the stresses are quite uniform with respect to the z coordinate. It is in this region that the elasticity analysis is valid. Consequently, it is in this region that the structural analysis will be refined to a substructural analysis, and the substructural analysis used to provide boundary data for the collocation scheme. It is fortunate that in many instances skin-stiffener separation occurs near the center part of the plate because the analysis methodology discussed here is indeed valid in this region.

Since attention will be focused on the central region of the plate, it is of interest to study the convergence of the structural level finite-element analysis in this area. Figure 27 illustrates a coarse mesh and a mesh which was refined twice in the central region. These two meshes and one which was refined once, not shown in the figure, were used to study plate response, and in particular, convergence. In the mesh refinement, triangular elements were used as transition elements. The triangular element, E33, and the regular element, E43, are discussed in Appendix C.

Figure 28 shows the convergence characteristics of the three components of displacement along x at $z=b/3$. The distance of $z=b/3$ is the distance from $z=0$ to the second nodal line along x and b is the flange half-width. The second nodal line was selected over the first one since along the first nodal line, at $z=0$, both w and β_x are zero and therefore cannot be used for convergence study. The displacements studied are the displacements at the skin midsurface. The figure shows the displacements for the three meshes used to study convergence, i.e., coarse , refined, and fine meshes. It is clear that the results for the refined and the fine meshes coincide, indicating convergence of the response along the line $z=b/3$. Figure 29 shows similar results for components of rotation, β_x and β_z along the line $z=b/3$ Although the figures present displacements and rotations data at $z=b/3$, similar convergence characteristics were observed for the entire mesh refinement region.

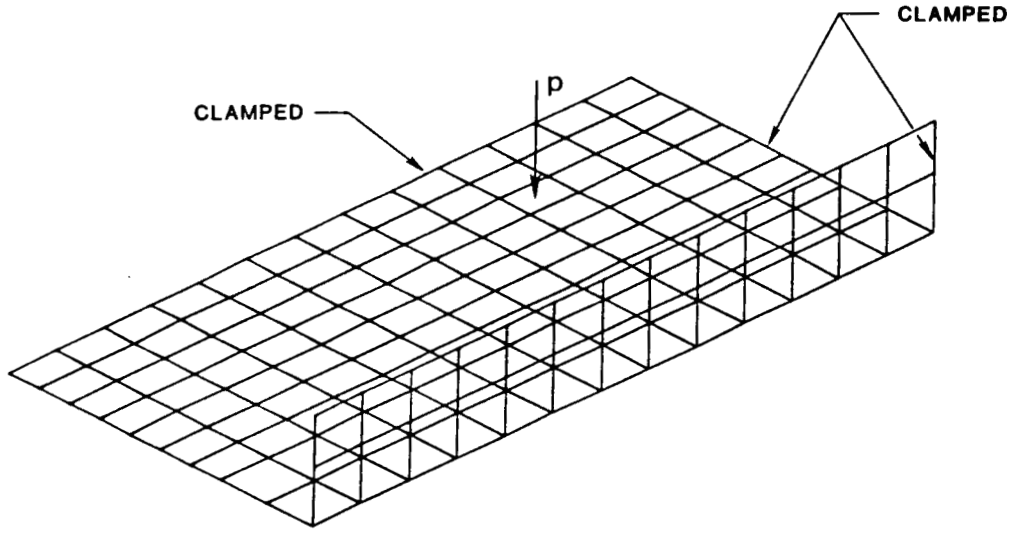

(a) Coarse Mesh

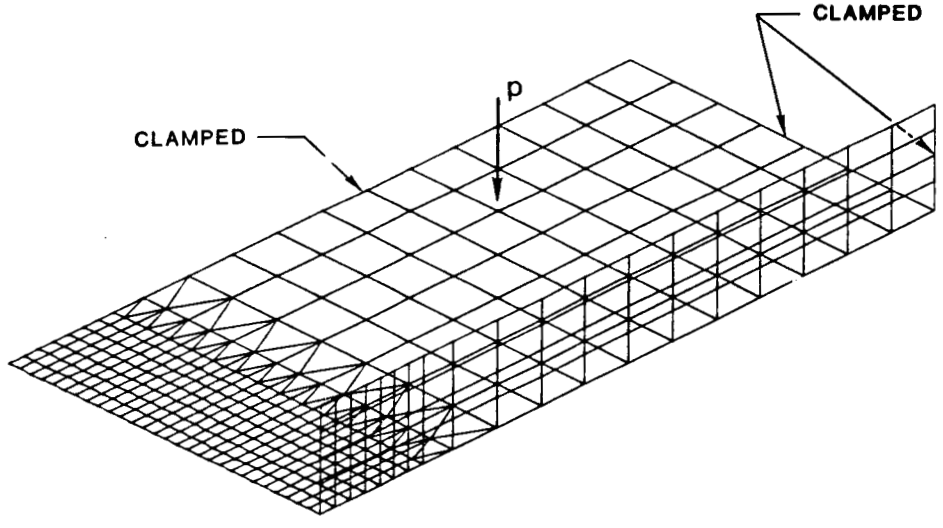

(b) Fine Mesh

Figure 27. 1/4 Symmetry Stiffened Plate Discretization and Mesh Refinements.

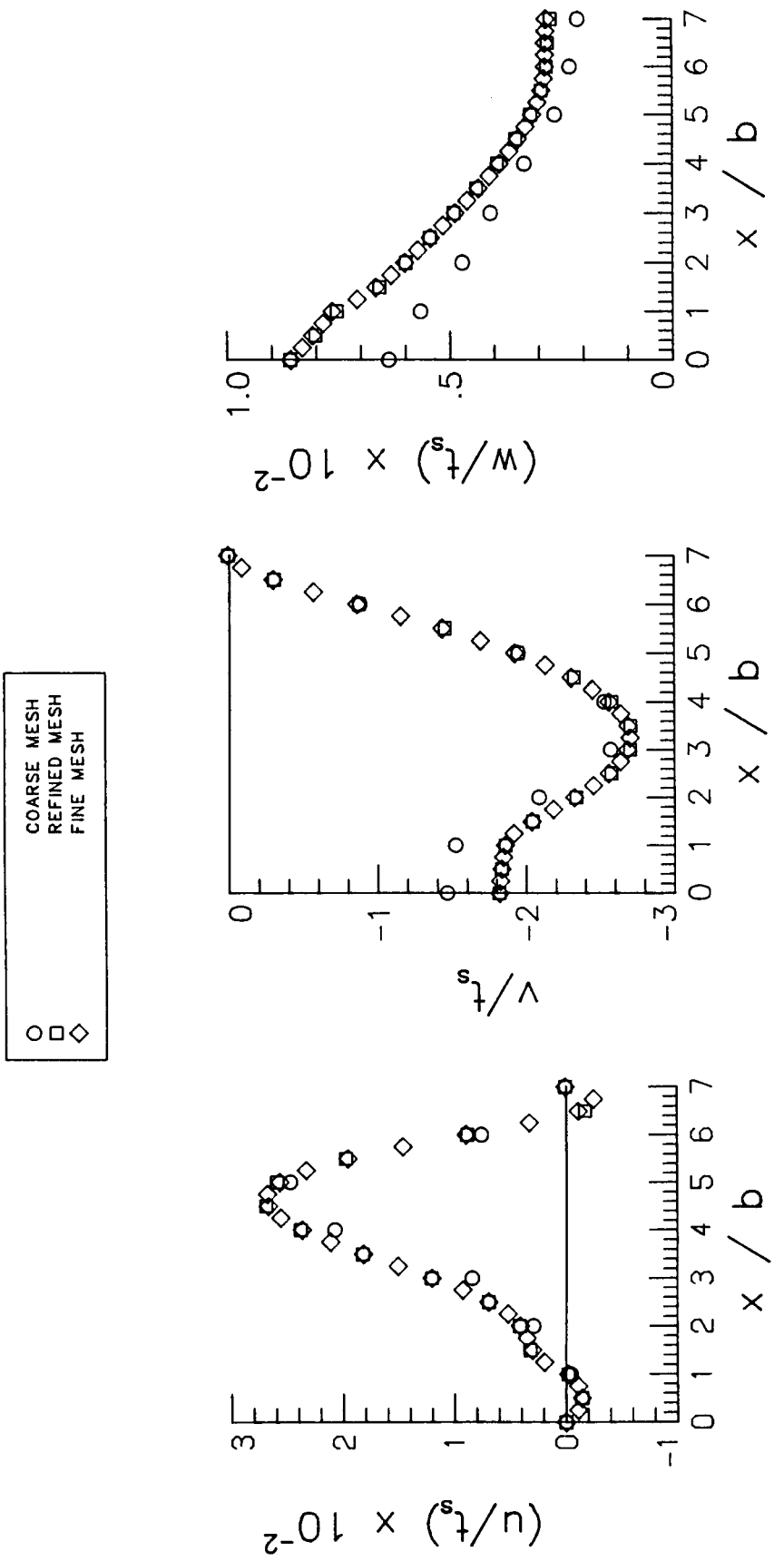

Figure 28. Displacement Convergence Study in a Stiffened Composite Plate Nonlinear Analysis with 10 psi Pressure (Data Plotted at z= b/3).

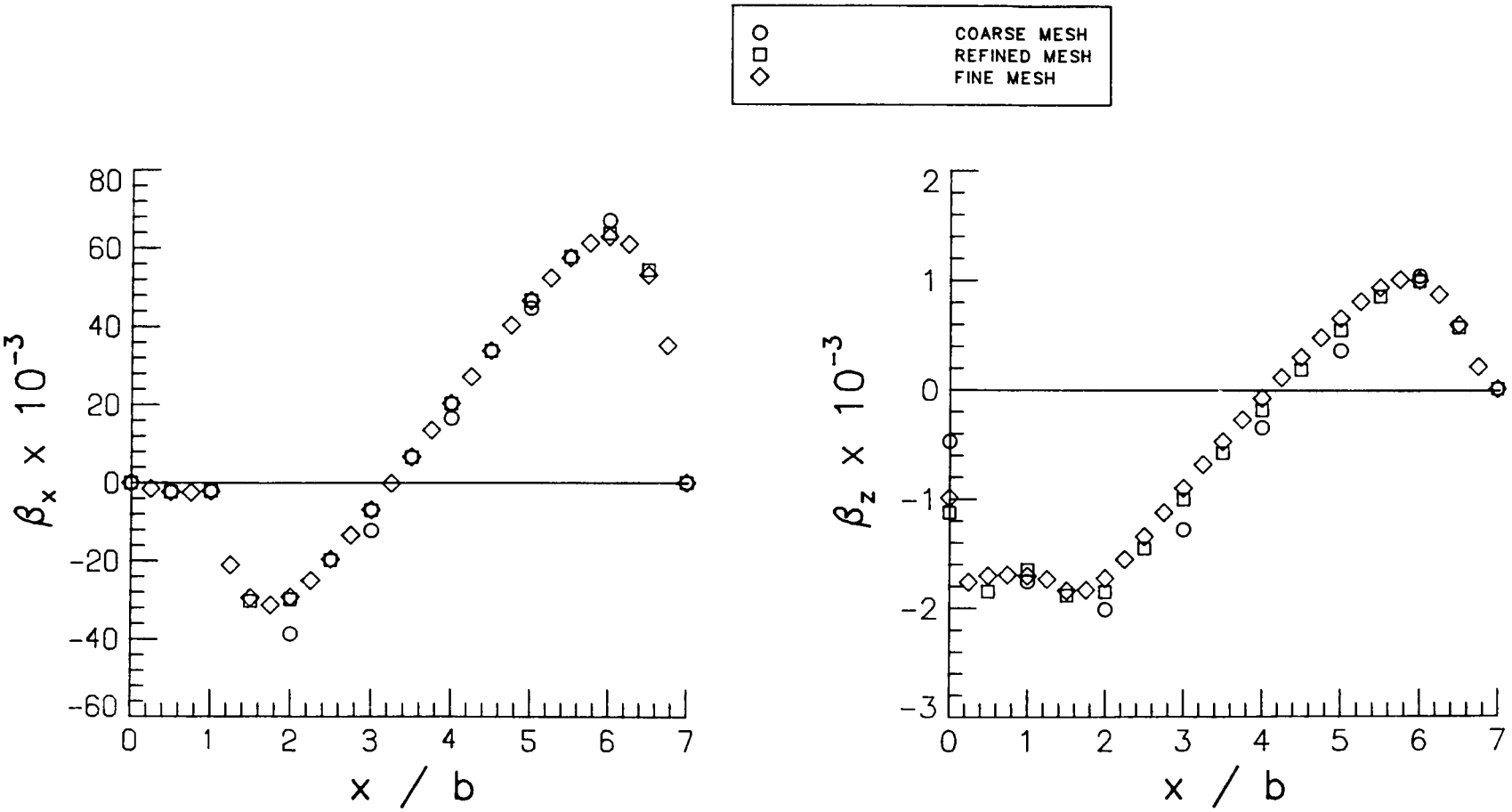

Figure 29. Rotation Convergence Study in a Stiffened Composite Plate Nonlinear Analysis with 10 psi Pressure (Data Plotted at z=b/3).

One of the unique characteristics of stiffened composite plates is revealed in Figure 28. This is the phenomenon of pillowing. Pillowing is the term used to describe the fact that the skin at $x/b \cong 3$ deflects out-of-plane more than the center-of-plate, $x/b = 0$. This pillowing literally pulls the skin away from the flange. Pillowing is the reason the displacement of the skin in Figure 26 is greater than the displacement of the center-of-plate.

3.3.2 Substructural Analysis

The substructural analysis is conducted using 8-node hexahedrons and 6-node pentahedrons, solid elements which are available in EAL. Each node of these elements has 3 degrees of freedom, namely u, v, and w. Both elements accept fully anisotropic material constitutive behavior. To be consistent with the elasticity solution developed, the material compliance matrix is taken to be orthotropic. A brief description of the two solid elements used is given in Appendix C.

The substructural analysis is conducted on isolated area in the structure. As mentioned above, attention is given to the plate center location. The region for which the substructural analysis is carried out is indicated by the area outlined by the heavy line in Figure 30. In addition, Figure 30 also shows schematic discretization of the substructure model. The model includes both sides of the symmetry plane and has a width of 4b/3. One side of the model coincides with nodal lines in the structure model at $z = 2b/3$. The model is discretized with 8 elements in the z direction and the mesh refinement of the flange-skin cross-section corresponds to the coarse mesh used in section 2.6. As was done in the structural analysis, the web is modelled with plate elements except that now the web is attached to the top of the flange. The following displacements boundary conditions are imposed on the substructure model:

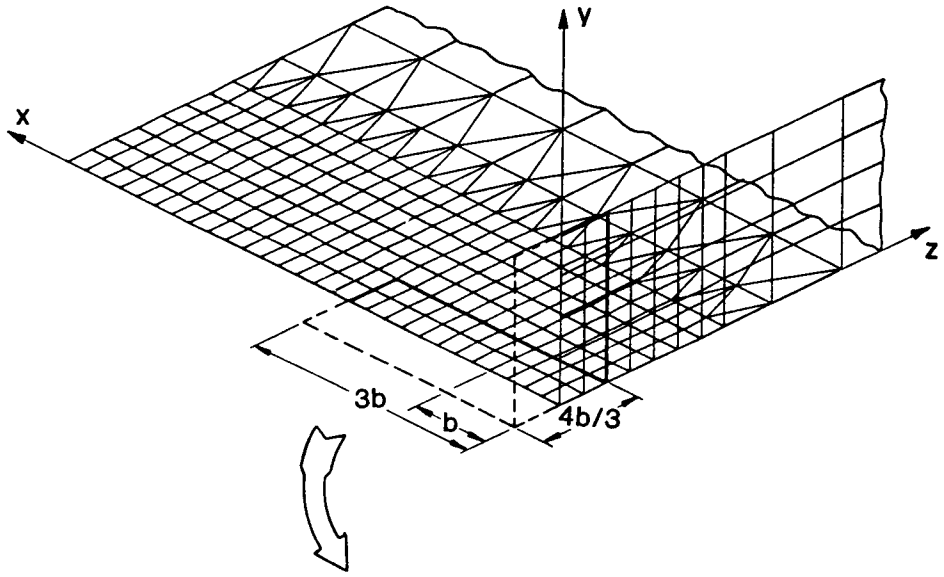

(a) Structure Model.

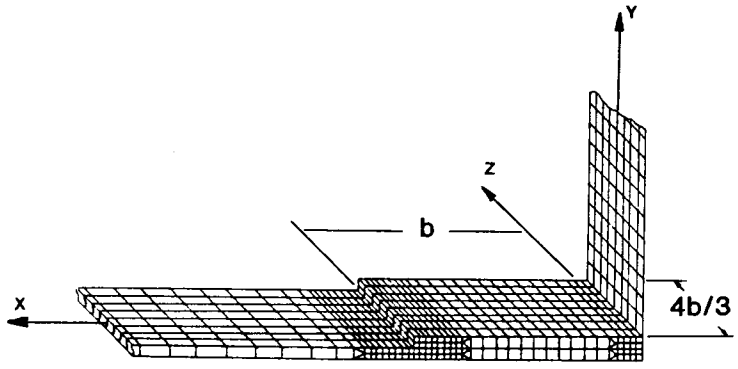

(b) Substructure Model.

Figure 30. Structural to Substructural Analysis Procedure and Schematic of Substructure Discretization.

Boundary	Specified Displacements
(x,y,-2b/3)	u, v, and w
(x,y,+2b/3)	u, v, and w
(3b,y,z)	u, v, and w
(0,y,z)	u = 0
(x,y,0)	w = 0

where u, v, and w are determined from the structural analysis displacement and rotation data by applying Kirchhoff assumptions. That is:

$$u(x,y,z) = u_o(x,z) - \frac{\partial v_o}{\partial z} y \quad , \qquad [68.a]$$

$$v(x,y,z) = v_o(x,z) \quad , \qquad [68.b]$$

$$w(x,y,z) = w_o(x,z) + \frac{\partial v_o}{\partial x} y \quad . \qquad [68.c]$$

Here, u_o, v_o, and w_o are the displacements of the skin midsurface as determined from the structural level analysis. On the -z boundary the displacement boundary conditions are evaluated using the oddness and evenness of the displacement and rotation functions. These conditions are

$$u_o(x,z) = u_o(x,-z) \; ; \quad v_o(x,z) = v_o(x,-z) \; ; \quad w_o(x,z) = -w_0(x,-z) \quad ,$$

$$\frac{\partial v_o(x,z)}{\partial x} = \frac{\partial v_o(x,-z)}{\partial x} \; ; \quad \frac{\partial v_o(x,z)}{\partial z} = -\frac{\partial v_o(x,-z)}{\partial z} \quad . \qquad [69]$$

C-2

The boundary conditions determined by using eq. 68.b lead to unnatural through the thickness constraints at the boundaries of the substructural region. This restriction may be alleviated by specifying linear variation of v through the thickness, as was done in [44]. In the present study the local elasticity analysis was performed along the substructure symmetry plane [x,y,0]. Consequently, it was felt that the effect of through-the-thickness constraints at the boundaries, ($z = \pm 2b/3$), would have little if any effect on the state of stresses of the location $z=0$. In addition to the displacement boundary conditions of eqs. 68, the substructure model was subjected to transverse pressure. Here the pressure load was applied in the form of a vacuum to the skin side. This was done in order to simulate the loading conditions used in [10].

In a linear analysis, a set of displacements corresponding to a particular pressure level, as compute by the structural analysis, is imposed on the substructure model. The system of equations representing the state of the body is then solved once. Solution for any other pressure level may be obtained by simple ratio of the previous results. In a nonlinear analysis, a more complicated procedure is required. Specifically, the response at each pressure level is the result of a series of finite-element calculation. First, a converged set of displacements and rotations for a particular pressure level, say p_1 , is obtained using the structural analysis. This set of displacements and rotations are then used to compute the boundary conditions discussed above for the substructure model. Next, using these conditions, the set of equations representing the substructure is solved iteratively until convergence is reached for that pressure level. The converged solution represents the solution for one pressure level, p_1. The process must be repeated if another, say a higher, pressure level is required. Using the converged solution, the stresses can be computed at any point throughout the interior of the substructure using the stress polynomials which are part of the EAL finite-element formulation (see Appendix C). These stresses are then used in the collocation scheme.

Before proceeding to discuss the local analysis procedure, it is instructive to compare the response predicted by the substructural analysis with the response of the structural analysis.

Probably the single most significant kinematic variable in the analysis of flexible stiffened plate structures is their out-of-plane deformation. Consequently, this variable was chosen as a measure of comparison between the two models. The results of such comparison are shown in Figure 31. In this figure the out-of-plane displacement v is plotted as a function x for both the structure and substructure models. The results correspond to nonlinear analysis using 10 psi applied pressure. One portion of the figure corresponds to v(x,0) and the other portion to v(x,b/3), z=b/3 being half the distance between the symmetry plane and the boundary in the substructure model. The substructure extends to 3b in the x direction, as can be seen from the point of termination of the dashed line. The figure demonstrates the excellent agreement between the two models. However, as would be expected, the substructure model appears to be slightly stiffer. One may improve on the agreement between the two models by adding additional elements in the z direction to the substructure model. This, off course, would increase the cost per run. The error observed with the present results are on the order of 1 to 2 % and do not justify the increase in cost.

3.3.3 Application of the Local Elasticity Analysis

In practice there is only one difference between the geometrically linear and nonlinear local elasticity analyses. The difference between the two is that in the nonlinear analysis the collocation procedure must be performed in the deformed body configuration. In practice, this presents no problems. It should be pointed out that should collocation of displacements or a mixture of displacements and stresses been used, extension to the nonlinear case would not have been as simple. Given the discussion of section 3.2, the only requirement on the local geometrically nonlinear elasticity analysis which is different from the linear analysis is that σ_n and τ_s must be computed in the deformed local region configuration. Having computed the normal and tangential stresses along boundaries CD and EF (see Figure 23), the collocation

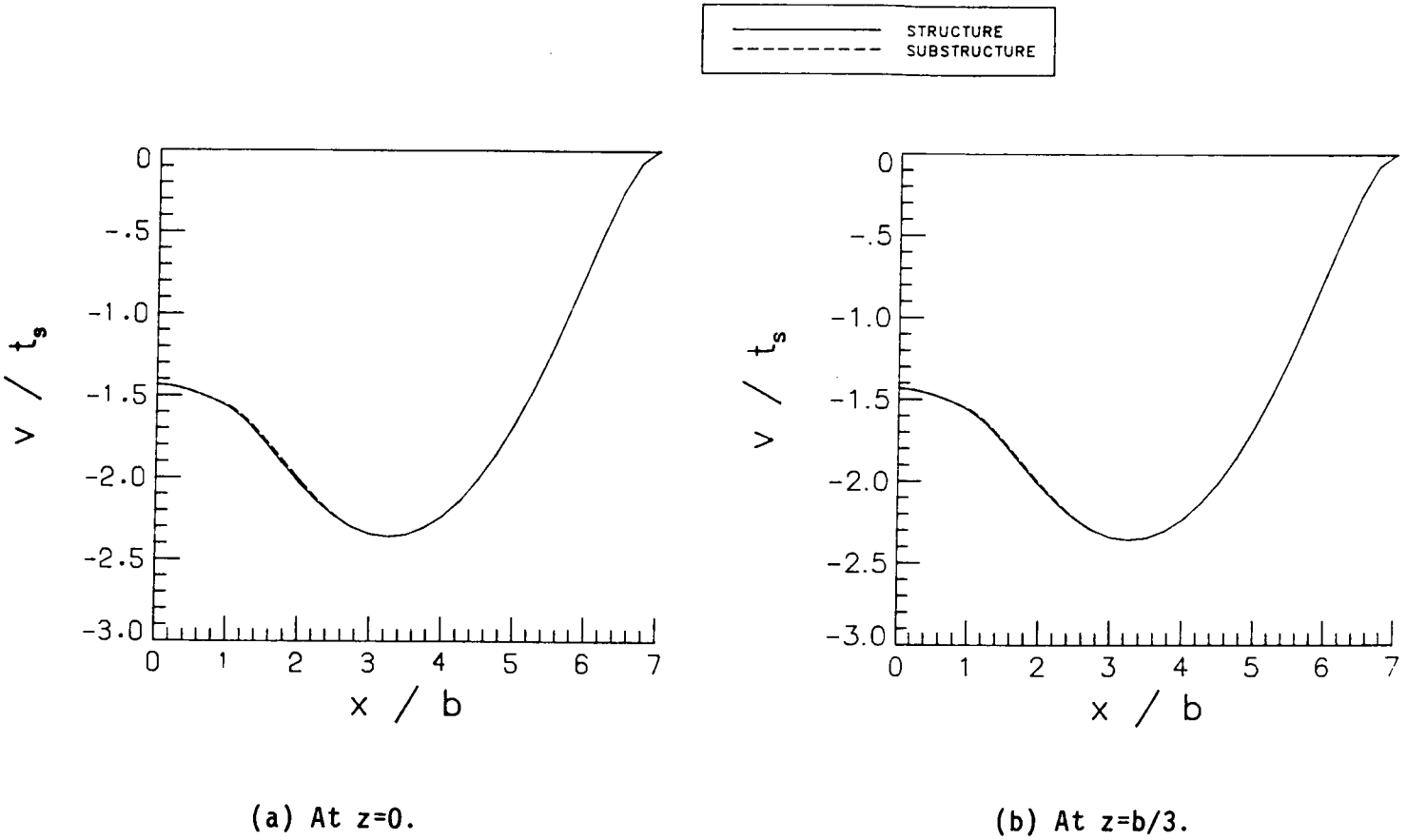

Figure 31. Transverse Deformation, v, for Structure and Substructure Models, Nonlinear Analysis at 10 psi Pressure.

procedure outlined in section 2.4 has the same format for the two types of analyses. For the loading conditions considered in the study, boundary DE of the local region is subjected to applied pressure, p. As stated earlier, this pressure is negligible, in the collocation procedure context, as compared to the stresses generated by the pressure (i.e., on boundaries CD and EF).

Other restrictions in the present analysis which are a result of the assumptions used in the the elasticity solution relate to the uniformity of response in the local region. These restrictions are:

(a) The stresses do not vary with z.

(b) e_o, κ_z , and κ_{xz} are uniform throughout the local region.

For the skin-stiffener geometry, the loading conditions, and the material constitutive law used, these conditions are met to within a 10 % (or less) variation. With a 10 % variation, the restrictions imposed by the elasticity solution are not perfectly satisfied. However, they are sufficiently close from an engineering view point.

To utilized the convergence information established in section 2.6, the stress calculations in the local region using EAL solid elements are compared to the stress calculations using the PE2D finite-element. It was hoped that on the boundary of the local region, the EAL solid elements would yield the same stresses as the PE2D elements. If the data compared favorably, then the convergence studies of Chapter 2, using PE2D, could be used to imply convergence of the EAL analysis. To facilitate this comparison, a case which was studied previously using PE2D was used. This is the case of bending illustrated in Figure 4. The results of one such comparison is shown in Figure 32. The comparison is for the coarse mesh Figure 4.a. As before, the interface stresses are normalized by $\frac{Mt_s}{2I}$. Both the stresses in the skin and flange, at the interface, as computed by EAL and PE2D are shown. Further, the elasticity solution as derived from the collocation of stress data generated by EAL and generated by PE2D analyses are also plotted. Apparent from the figure is that the two approaches produce identical elasticity solutions. On the other hand, there are some differences with regard to the finite-

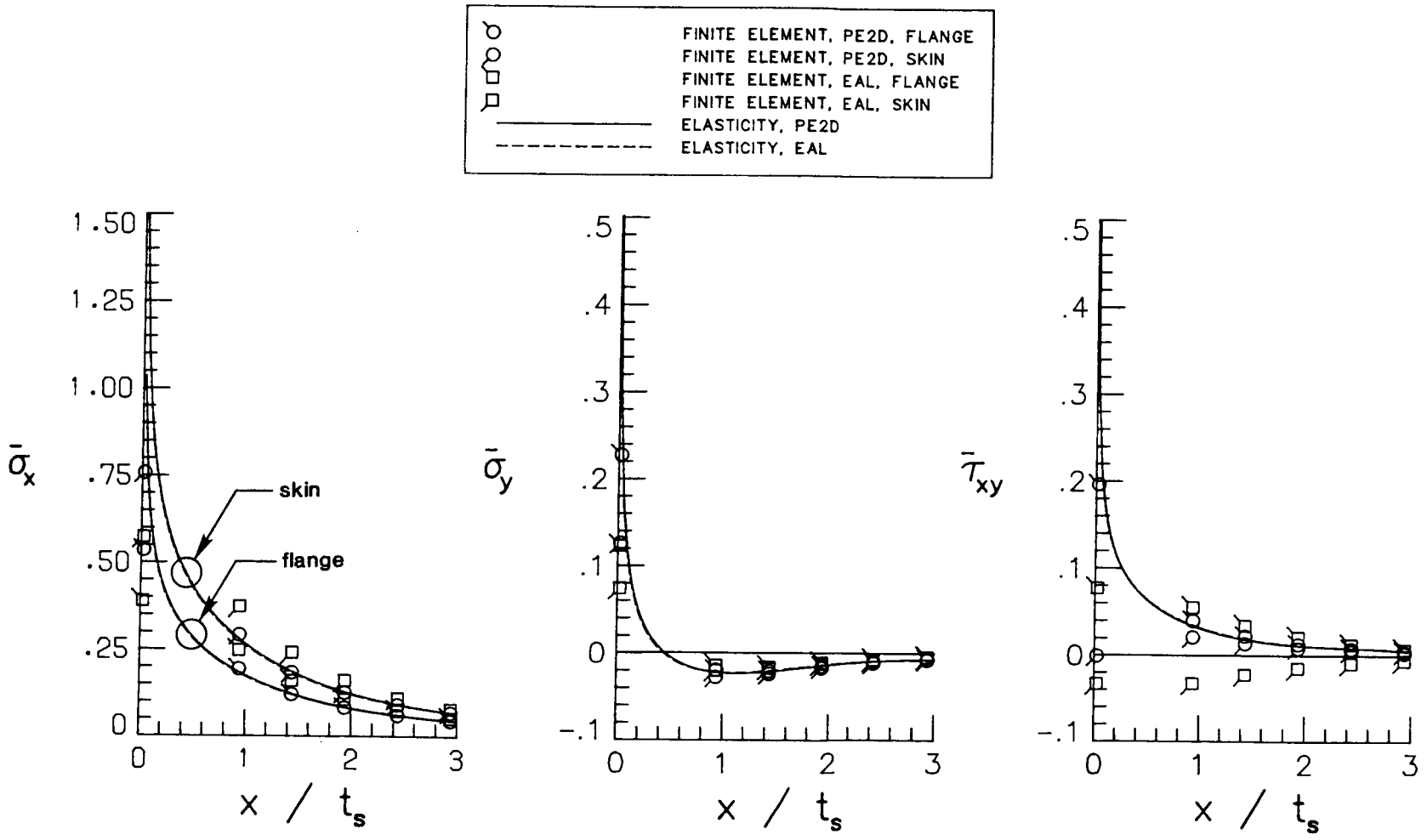

Figure 32. Skin-Stiffener Stresses, σ_x, σ_y, and τ_{xy} in the Local Region; EAL Verses PE2D.

element computed stresses within the localized region. This is particularly apparent for τ_{xy} . However, this is not surprising, since the EAL solid elements have constant shear stress through the element cross-section. Hence such an element will have a more difficulty conforming to the large stress gradients in the localized region. Nevertheless, PE2D and EAL produce almost identical stresses along the local region boundaries at $x/t_s = \pm 3$. This in turn produces the perfect agreement between the two elasticity solutions. Based on the data presented in section 2.6 and comparisons like the one shown in Figure 32, it was concluded that the use of EAL leads to an accurate local elasticity analysis.

In the last part of this chapter the local analysis of the skin-stiffener interface in the pressure loaded plate is presented. This presentation completes the analysis procedure depicted in Figure 24, starting with the structural analysis of Figure 27, proceeding to the substructural analysis of Figure 30, and ending with results similar to Figure 32, but for a pressure loaded plate. In the following figures, the stresses are normalized by the applied pressure, p, and distance have been normalized by the flange half-width, b, or by the skin thickness, t_s.

The stresses along the entire skin-flange interface are shown in Figure 33. Figure 34 focuses on the distribution of these same stress components in the local flange termination region. It should be kept in mind that the loading is actually a 10 psi vacuum applied to the side of the plate without the stiffener. Thus the plate out-of-plane deformation is in the -v direction (see Figure 24). The flange termination angle is 90°. Figure 33 indicates that along the entire interface, on either side, the stress σ_x is positive. This despite the fact that the interface is on the top side of the skin and, in the sense of a linear analysis, subjected to compressive bending stresses. The positive σ_x is attributed to the tensile membrane force that develops as a result of the large out-of-plane deformations of the plate.

The peeling, σ_y, is nonzero at the flange termination point, the local region, and under the stiffener web. Since the stiffener web has much more resistance to out-of-plane deformation, the skin has a tendency to pull away at this locality as well as in the flange termination region.

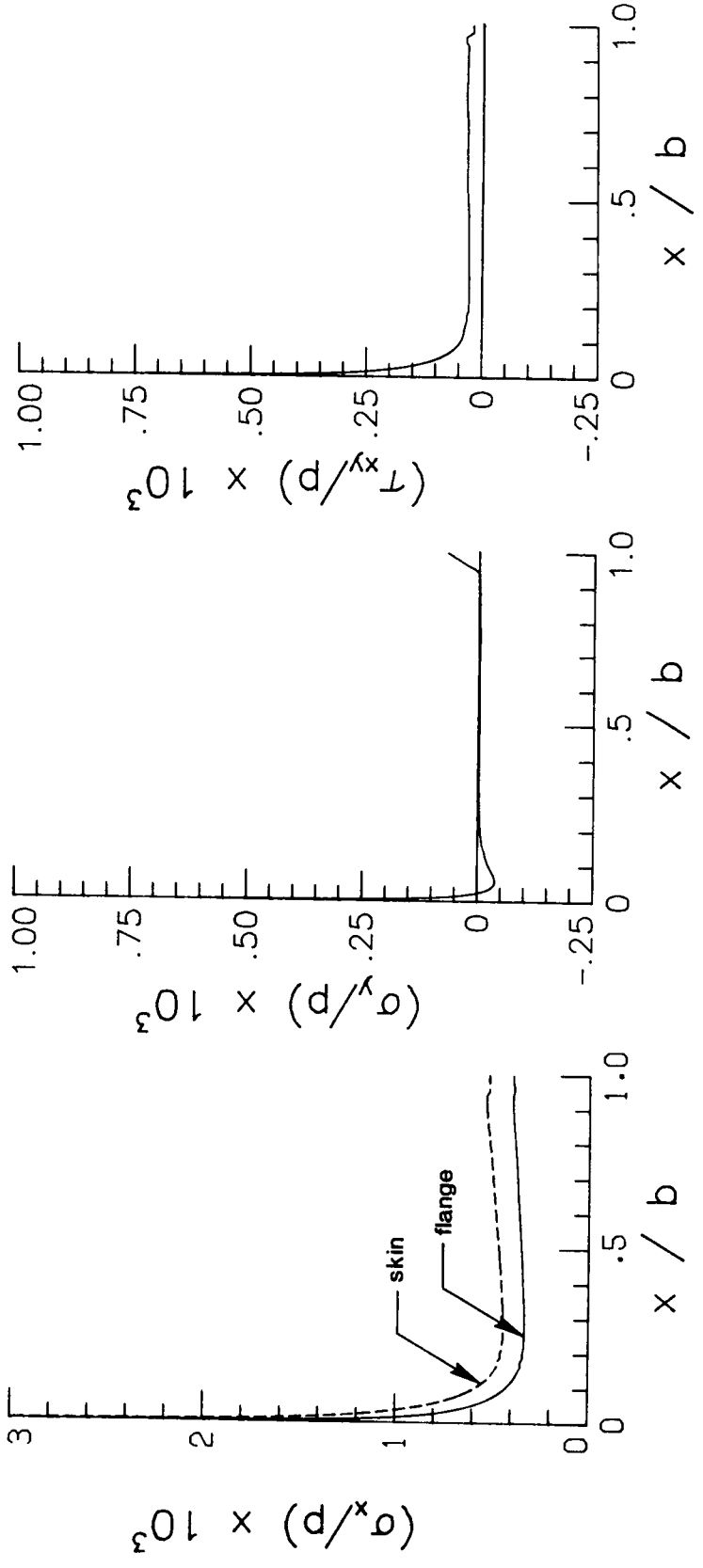

Figure 33. Skin-Stiffener Stresses Along the Entire Skin-Flange Interface Length in Pressure Loaded Plate.

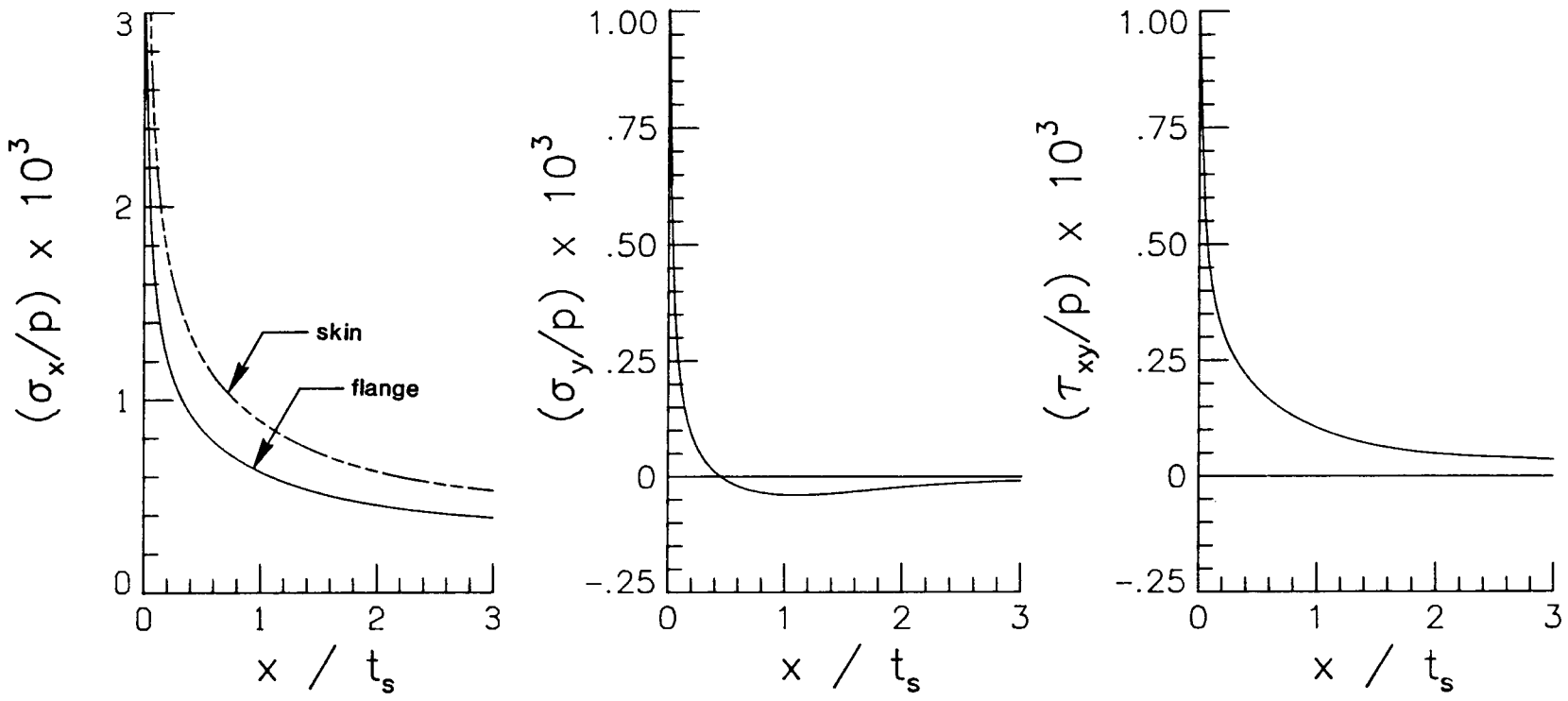

Figure 34. Skin-Stiffener Stresses in the Local Flange Termination Region in Pressure Loaded Plate.

The shear stress τ_{xy} is nonzero along the entire skin-flange interface, but it is constant in magnitude away from the flange termination point, and away from the web.

This concludes the discussion as related to the analytical developments and their application to actual stiffened-skin composite structures. In the next chapter the structure-substructure-local analysis procedure will be used to investigate the influence of geometric nonlinearities on skin-stiffener interface stresses. Following that is study of the influence of stiffener parameters on the state of interface

4. Results

With the methodology for computing skin-stiffener interface stresses verified as regards convergence and fidelity, the influence of various stiffener parameters on the skin-stiffener interface stresses can be evaluated. In addition, the importance of geometric nonlinearities can be evaluated, and an assessment of the error incurred by not including these effects can be made. To that end, this chapter begins by evaluating the influence of geometric nonlinearities on the interface stresses. This is followed by the determination of the effects of stiffener parameters on the state of these stresses. In the last part of this chapter, criterion by which various stiffener designs may be evaluated for their tendency to separate, using the current analysis procedure, are presented. The results presented in the following sections are for a plate clamped on all four edges with a single stiffener, depicted in Figure 22. The plates are subjected to three levels of transverses pressure, 1, 10, and 20 psi, respectively. The 10 psi pressure level represents the operating aircraft fuselage pressure, while the 20 psi pressure represents the design level. The 1 psi pressure level is used since the linear and nonlinear analyses would produce similar results at this pressure level, and linear results for the other pressure levels can be scaled from the 1 psi analysis.

4.1 The influence of Geometric Nonlinearity

To a great extent, the importance of incorporating geometric nonlinearities in the skin-stiffener interface stress analysis will depend on how flexible the structure is. For stiffened aircraft structures which exhibit out-of-plane deformations on the order of magnitude of 2 to 4 times the skin thickness, geometrically nonlinear effects can be significant. As was evident from Figure 26, the skin-stiffener configuration being studied did in fact experience such deformation levels.

To study the influence of geometric nonlinearities on the interface stresses, a baseline skin-stiffener configuration is considered. The three pressure levels are used, and the linear analysis case is also considered for comparison. The baseline stiffener design has a web height of $h_w = 1.5$ in., a flange width of $2b = 1.5$ in., and a flange thickness of $t_f = 0.04$ in. For this configuration the flange and the web are constructed of a quasi-isotropic laminate with $(\pm 45/0/90)_s$ layup sequence. The skin is orthotropic with a laminate layup of $(\pm 45/90_2)_s$, and skin thickness of $t_s = 0.04$ in.

Figure 35 illustrates the skin-stiffener interface stresses, σ_x, σ_y, and τ_{xy} along the entire flange-skin interface length. Each portion of Figure 35 illustrates four relations, three of which represent nonlinear analyses for 1, 10, and 20 psi pressures, and one that corresponds to the linear analysis. Each relation is determined using a combination of stress data generated by an elasticity analysis in the local region, and an EAL finite-element analysis outside of this locality. In Figure 35 and all other figures which display stress data, stresses are normalized by the applied pressure. With this normalization the linear analysis is independent of the applied pressure level. The distance, x, from the flange termination vertex is normalized by b, the flange half width, or by t_s, the skin thickness. Clearly evident from the figure is the nonlinear interaction between the level of applied pressure and the magnitude of the skin-stiffener

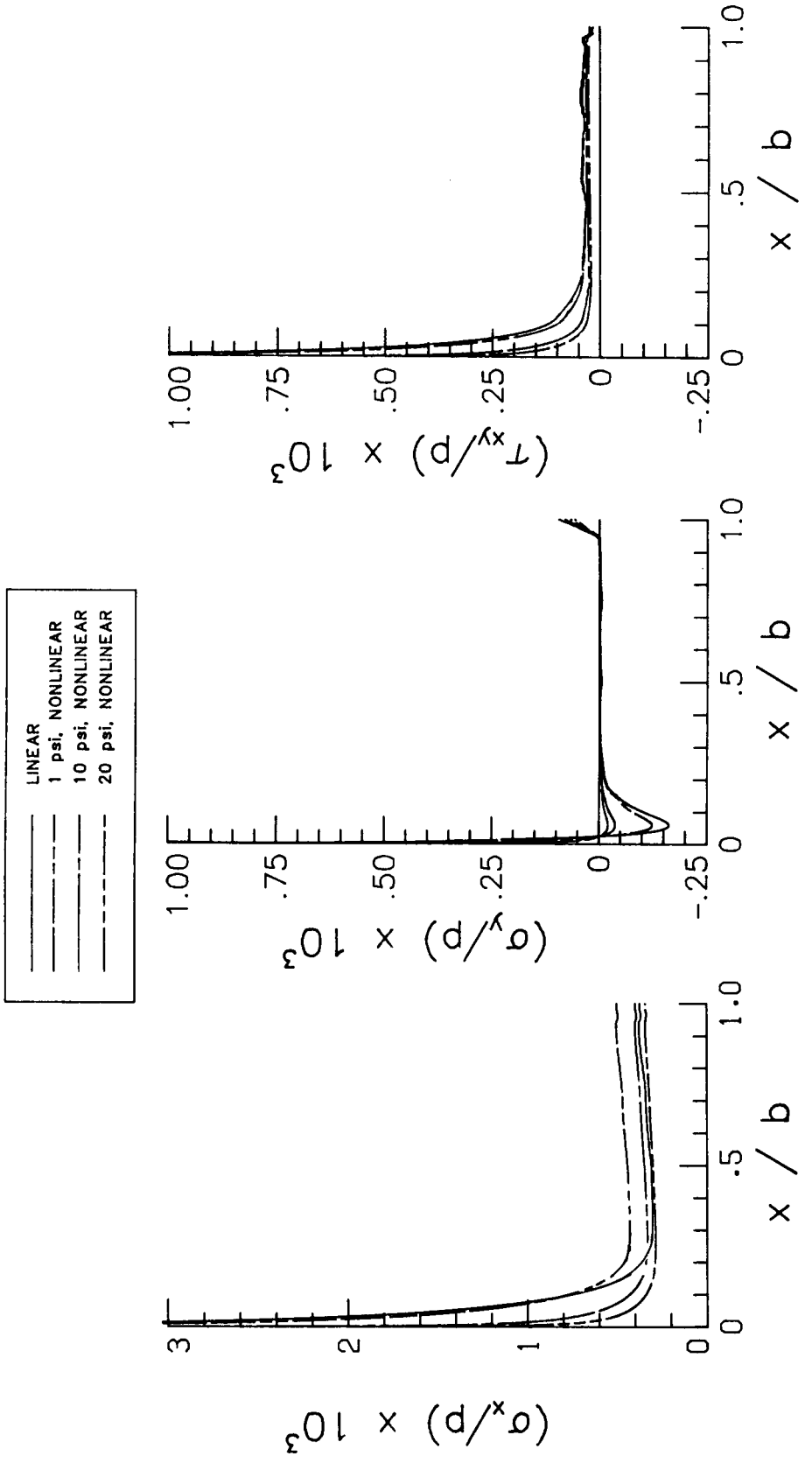

Figure 35. Distribution of Skin-Stiffener Interface Stresses Along the Entire Flange Length, Linear and Nonlinear Analyses Results.

interface stresses. Focusing on the peel stress, for example, the linear and the 1 psi nonlinear analyses produce stresses of similar magnitude. However, the nonlinear analysis for 10 psi and the linear analysis show significantly different results. The 20 psi nonlinear analysis deviates even more from the linear analysis. In all cases and for all stress components, the large stress gradients appears to be confined primarily to the local flange termination region. Under the web there is a local maximum in the peel stress and the maximum value tends to decrease slightly with increases in pressure. Relations like the one shown in Figure 35 indicate that load transfer from the skin to the stiffener is confined to either a very short portion of the flange width (something on the order of b/4), or directly under the web. In Figure 36 attention is shifted to the interface stress distribution in the flange termination area. As in the previous figure, there are four relations in each portion of the figure, one for the linear analysis and the other three for nonlinear analyses. Only the interface peeling, σ_y, and shearing, τ_{xy}, stresses are shown in this figure. The most significant point to emerge from Figures 35 and 36 is a clear illustration of the nonlinear interaction between the applied pressure and skin-stiffener interface stresses. If a linear analysis is used, the normalized interface stress variation throughout the flange termination region would be independent of the applied pressure. However, with geometric nonlinearities included, significant changes in the characteristics of the stress distributions are observed. In a geometrically nonlinear analysis an increase in pressure tends to flatten the peeling stress relation. Increases in pressure lead to a shift in the high stress gradients in both the peeling and shearing stress relations toward the flange termination point. As a result, it appears that increases in pressure lead to a reduction in the area under the two stress relations. The possible significance of such behavior in the stiffener separation context will be discussed latter.

As noted above, the variation in σ_y throughout the local interface region is markedly different between the 1 and 20 psi pressure levels. This may be understood by considering Figure 37. In this figure the stress component σ_x along the collocation boundaries CD and EF (see Figure 23) is plotted as a function of the distance through the thickness, y. Boundary EF cuts

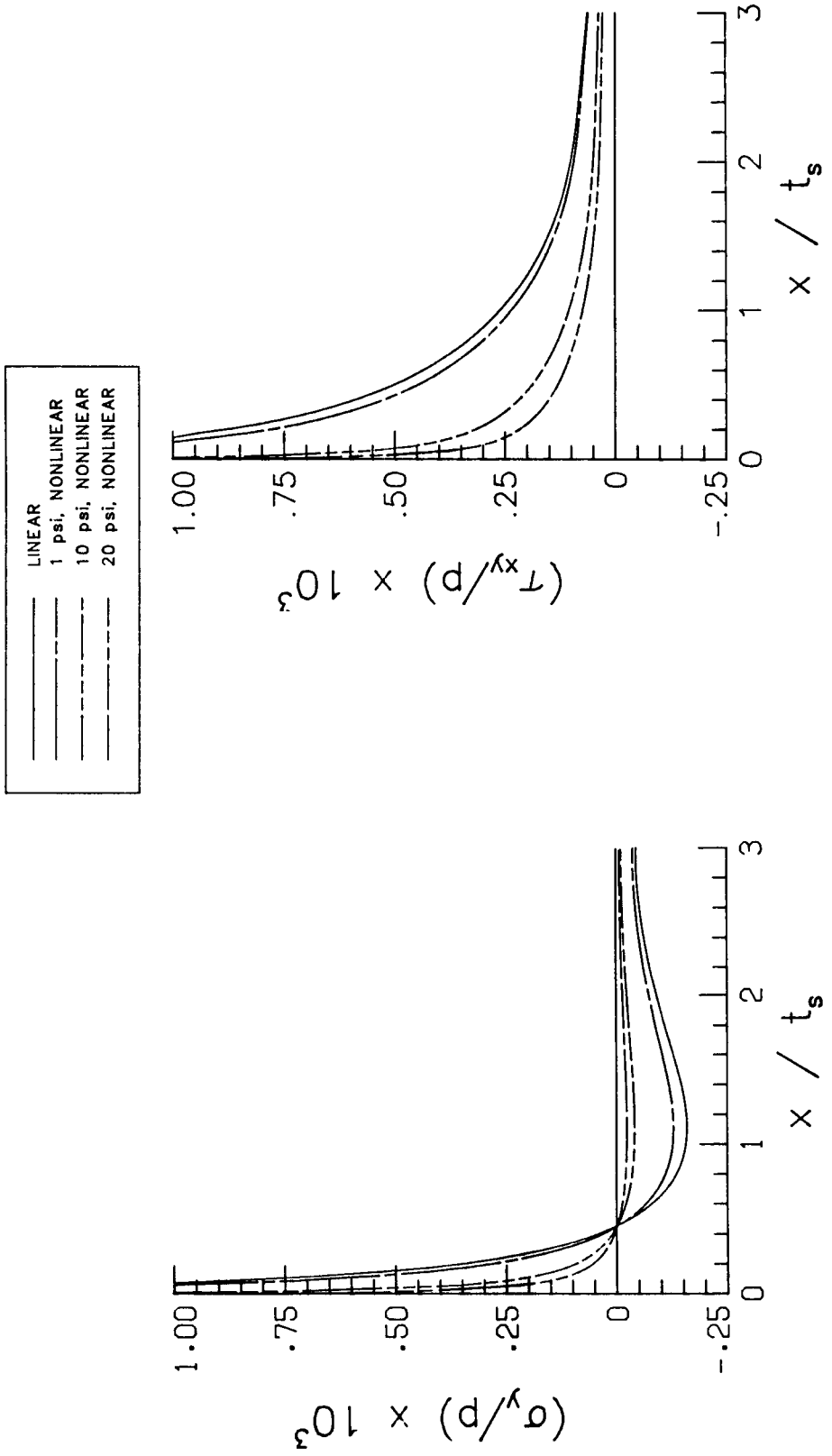

Figure 36. Variation of Skin-Stiffener Interface Peeling and Shearing Stresses in the Local Flange Termination Region.

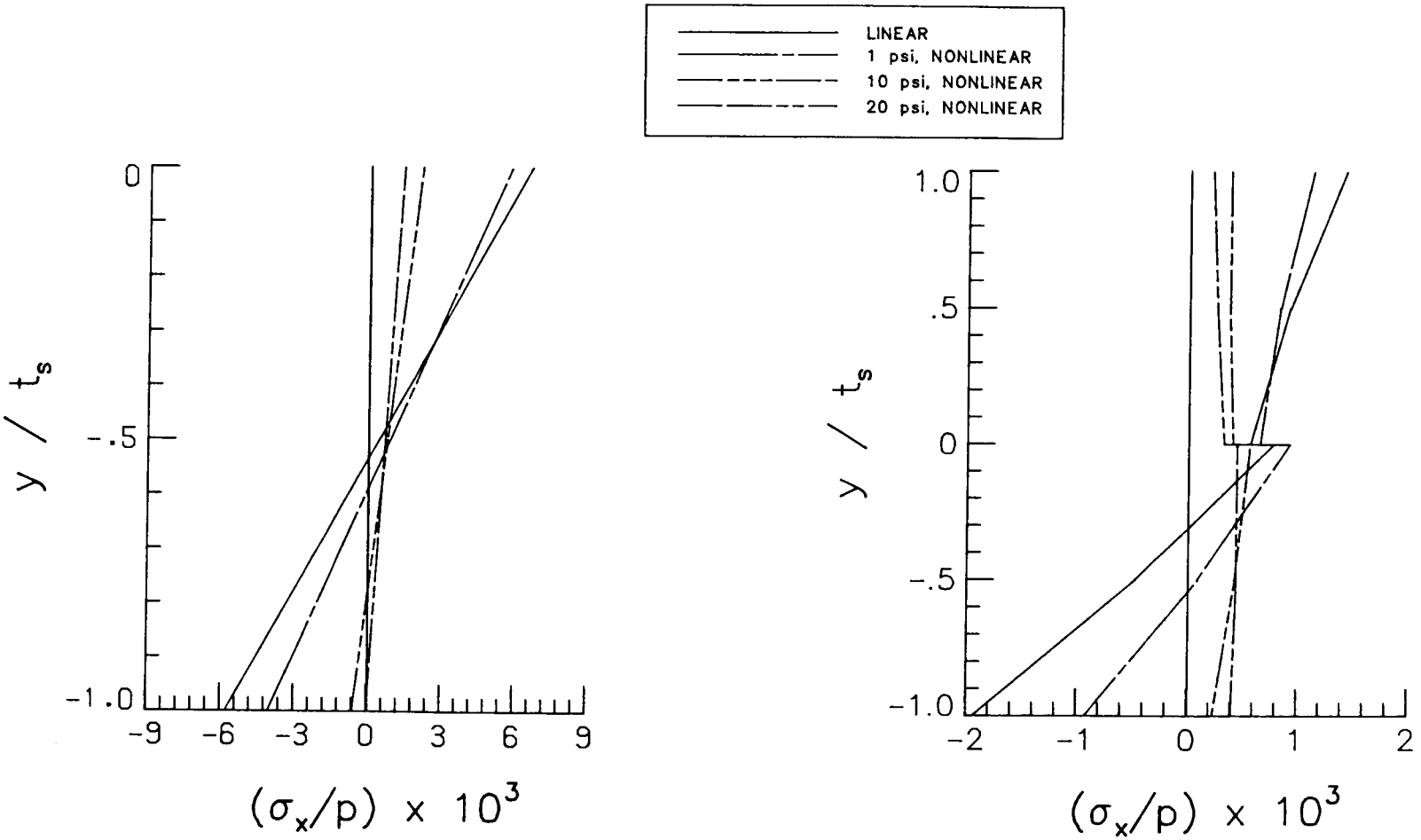

(a) Through the Skin Thickness, at $x=-3t_s$.

(b) Through the Skin and Flange Thicknesses, at $x=3t_s$.

Figure 37. Distribution of σ_x Through the Skin and Skin-Flange Thicknesses Along the Collocation Boundaries.

through the skin at $x = -3t_s$, whereas, boundary CD cuts through the skin and the flange at $x = +3t_s$. It should be noted that on these boundaries $\sigma_x = \sigma_n$ and $\tau_{xy} = \tau_s$, and that both σ_n and τ_s are collocated. Nevertheless, σ_n is about two orders of magnitude larger than τ_s, and therefore has the most significant influence on the local elasticity solution. As in previous figures there are four relations on each plot, one for the linear analysis and three for the nonlinear analyses at the 1, 10, 20 psi pressure levels. Concentrating for the moment on the stress in the skin, Figure 37.a, the most important point to emerge is that at a low applied pressure, the skin is loaded primarily in bending. As a matter of fact, in a linear analysis of the stiffened plate which is loaded by pressure, the skin should be loaded in pure bending. This is indeed evident from the line depicting the linear analysis results. For a linear analysis at higher applied plate pressures, the relation would remain one of pure bending. However, due to the geometric nonlinearities, the stresses in the skin change from a state which is nearly pure bending, at low pressure, to a state at the high pressure level which is dominated by stretching. At 20 psi the skin is entirely in tension. Turning to the skin-flange combination, the normal stress distribution through the skin and the flange at $x = +3t_s$ (Figure 37.b) shows more complex characteristics. This is due to the abrupt change in material properties in going from the skin to the flange. Nevertheless, σ_x becomes purely tensile at the higher pressure level. Since the local region must remain in force equilibrium, this is expected, the stress distribution in the skin-flange region balancing out the stresses in the skin away from the flange. The above data suggest that the observed differences in the peeling stress distribution for the 1 and 20 psi pressure levels are related to the state of inplane loading. That is, at low pressure levels, for which the plate is loaded primarily in bending, the peel stress distribution is high at the flange termination and reverses to become negative away from the terminus. At high pressure levels, for which the plate is loaded primarily in inplane stretching, the peel stress is reduced at the flange terminus and as a result does not experience as large a reversal away from the terminus, i.e., the peel stress distribution flattens with distance from the terminus.

To facilitate a better demonstration of this important nonlinear interaction between skin-stiffener interface stresses and applied pressure, stress eigenfactors (SEF) are used. These stress eigenfactors are defined as:

$$K_y = \lim_{x \to 0} x^{-\lambda_1} \sigma_y(x, 0; \lambda_1) \quad , \qquad [70.a]$$

$$K_{xy} = \lim_{x \to 0} x^{-\lambda_1} \tau_{xy}(x, 0; \lambda_1) \quad , \qquad [70.b]$$

where K_y and K_{xy} are the peeling and shearing stress eigenfactors, respectively, and λ_1 is the first eigenvalue. As noted previously, values of $-1 \leq Re(\lambda_1) \leq 0$ will lead to singular stress characteristics near the flange termination vertex. It should be noted that in the field of fracture mechanics the stress eigenfactor is commonly known as the stress intensity factor. The stress eigenfactor is a measure of how rapidly the stresses become unbounded as the flange termination point is approached. The factor can be used as a measure of the severity of the interaction between the skin and the stiffener. Figure 38 shows the skin-stiffener interface peeling and shearing stress eigenfactors as a function of the applied plate pressure. The stress eigenfactors have been normalized by the peeling stress eigenfactor for a 1 psi linear analysis. The influence of nonlinear effects is clearly illustrated in the figure. For a linear analysis the stress eigenfactor would simply be in proportion to the applied pressure. However, it is clear that inclusion of geometric nonlinearities results in a different behavior. Specifically, the stress eigenfactors increase slower than the applied pressure. This is consistent with the finding of Figure 36 and both figures point to the need for considering geometric nonlinearities in the study of skin-stiffener interaction. More importantly, it would appear that when conducting failure analyses of such structures, it should be recognized that a doubling of applied pressure does not result in a doubling of interface stresses and to assume so would be in error.

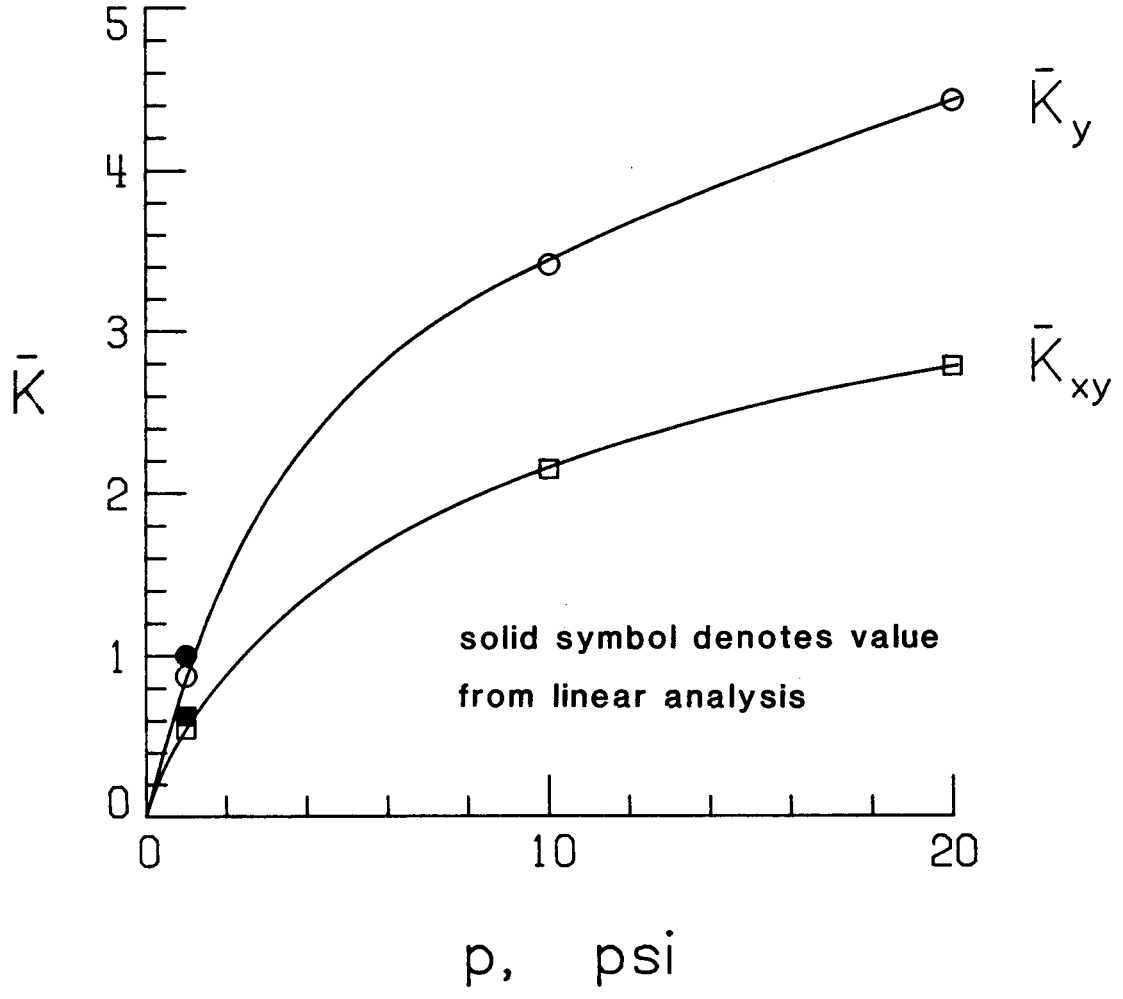

Figure 38. Peeling and Shearing Stress Eigenfactors as a Function of Plate Pressure.

Finally, the influence of geometric nonlinearities on the out-of-plane deformations of the baseline plate configuration are considered in Figure 39. The figure consists of two portions: one depicting the out-of-plane deformation along the symmetry line (x,0,0) and the other portion the deformation under the web, colinear to the stiffener, along the symmetry line (0,0,z). Each portion of the figure encompasses four relations, one representing a linear analysis at 1 psi pressure, and the other three corresponding to the nonlinear analyses at 1, 10, and 20 psi applied pressure. The out-of-plane displacement, v, is normalized by the skin thickness, t_s. The distance from the plate center (in the directions x or z) is normalized by the flange half-width, b. Visible from Figure 39 is the large pillowing effect, the skin away from the flange experiencing much larger out-of-plane deformations than the flange. This pillowing effect becomes more important with increases in pressure. As a result, geometric nonlinearities have an important role in determining the character of the pillowing. Specifically, for a linear analysis at 10 psi pressure, the maximum skin deflection would be about $7t_s$, while the stiffener deflection would be about $2t_s$. The nonlinear analysis at the same pressure level indicates that the maximum skin deflection is only $2.4t_s$, while the stiffener deflection is $1.4t_s$. Therefore it is clear that geometrically nonlinear effects actually reduce pillowing. The pillowing effect shown here was observed experimentally in [10].

This concludes the discussion of the importance of geometric nonlinearities in the analysis of skin-stiffener interface stresses. It has been shown that neglecting these effects may lead to large errors in the calculation of plate response, particularly interface stresses. Next, attention is given to an examination of the influence of stiffener geometry and material properties on skin-stiffener interface stresses.

4.2.1 Stiffener Parametric Study Results

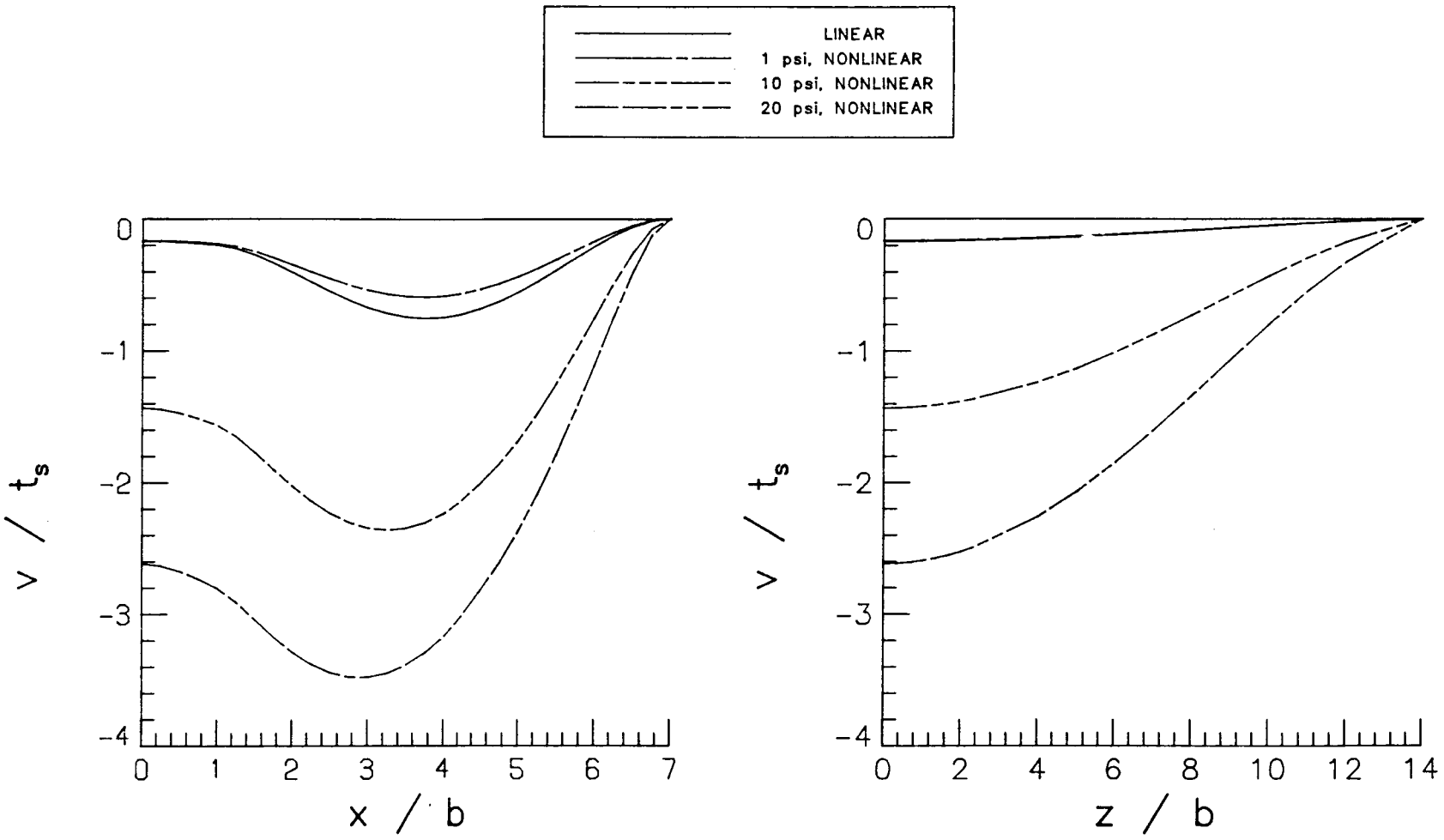

(a) Transverse to the Stiffener, Along (x,0,0).

(b) Along the Stiffener, Along (0,0,z).

Figure 39. Out-of-Plane Deformation for a Stiffened Composite Plate.

To establish the usefulness of the analysis method in the design of stiffened composite structures, eight different stiffener configurations are studied. Table 2 lists the various stiffener designs considered, and their designation, geometry, and lamination sequence. In the following sections each stiffener configuration is referred to by a nickname (second column in Table 2). This nickname signifies what is unique about this stiffener relative to the baseline configuration. The baseline configuration, configuration A, is always referred to by the nickname "baseline". The baseline stiffener design was defined earlier but for the reference, it has a web height h_w = 1.5 in., flange width 2b = 1.5 in., and flange thickness t_s = 0.04 in. For baseline, the flange and the web are constructed of a quasi-isotropic laminate with $(\pm 45/0/90)_s$ layup sequence. The skin is orthotropic with a laminate layup of $(\pm 45/90_2)_s$. In comparison to the baseline, the nickname "soft flange" was chosen for configuration B since the flange layup resulted in transverse flange modulus E_x = 3.83 Msi relative to E_x = 8.05 Msi of the baseline configuration. All other stiffener nickname designations follow the same logic. Lamina and laminate material properties are given in Appendix D. The structural analysis is conducted using the mesh shown in Figure 27. It should be noted that tapering of the flange will lead to a slight reduction in the moment of inertia of the flange relative to the case of a 90° flange termination angle. However, the structural analysis model is insensitive to the influence of the reduced moment of inertia. For this reason configurations A, B, D, and F are analysed using the finite-element discretization model for the baseline flange. Similarly, configurations E, G, H, and I are analysed using the finite-element discretization model for the thick flange. However, the substructural finite-element model for 90° and 15° flange termination angles are not the same, the difference reflecting the flange angle. The difference is similar to the difference between Figures 4 and 5. Based on the results which were presented in Figures 18 and 19, it is possible to use only one substructural finite-element analysis, for example, the one for the 90° flange angle, to produce two local elasticity solutions, one for 90° flange termination angle and another one for 15° flange termination angle. However, 15° is considered a shallow angle and it is not clear that one substructural analysis is all that is necessary. Since an important part of the current investigation is related to the method de-

Table 2. Stiffener Configurations.

Config-uration	Stiffener Nickname	Web Height	Flange Thickness	Flange Tapere Angle	Siffener Laminate
A	Baseline	1.50	0.04	90°	$(\pm 45/0/90)_s$
B	Soft Flange	1.50	0.04	90°	$(\pm 45/0_2)_s$
C	Short Web	0.75	0.04	90°	$(\pm 45/0/90)_s$
D	Tapered Flange	1.50	0.04	15°	$(\pm 45/0/90)_s$
E	Thick Flange	1.50	0.08	90°	$(\pm 45/0/90_2/0/ \pm 45)_s$
F	Soft & Tapered Flange	1.50	0.04	15°	$(\pm 45/0_2)_s$
G	Thick & Tapered Flange	1.50	0.08	15°	$(\pm 45/0/90_2/0/ \pm 45)_s$
H	Thick & Soft Flange	1.50	0.08	90°	$(\pm 45/0_4/ \pm 45)_s$
I	Thick, Soft, & Tapered Flange	1.50	0.08	15°	$(\pm 45/0_4/ \pm 45)_s$

velopment and verification, two separate substructure analyses are used. In a latter part of this section data is presented to support the assertion that a single analysis would lead to acceptably accurate results, but not as accurate as for less shallow angles, say 45°.

The results in the following section are presented in a form of skin-stiffener interface peeling and shearing stresses throughout the localized region. Each figure represents a comparison of the stresses between the baseline stiffener configuration and one of the other eight stiffener designs. Stress data are given for 1 and 20 psi applied pressure and are based on a nonlinear analysis. The low pressure represents the level at which linear and nonlinear analyses give similar results. The high pressure level represents a pressure where geometrically nonlinear effects become significant. The figures are useful in demonstrating qualitatively how interface stresses are affected by the various stiffener parameters. However, they may be less helpful quantitatively since they provide stress distributions rather than one numerical value which can be applied to design, failure, or optimization procedures. The calculation of a numerical value is done in the last part of this chapter, where the performance of each stiffener configuration is evaluated against the baseline stiffener design.

Figure 40 shows a comparison of skin-stiffener interface peeling and shearing stresses between the baseline and the "soft flange" configurations. It appears from the figure that reducing the transverse flange modulus, E_x , more than 50% has little effect on the peeling stress. It does tend to slightly reduce the shearing stress near the flange vertex. Figure 41 details the interface peeling and shearing stresses for both the baseline and the "short web" configurations. Evident from the figure is that shortening the web leads to a significant reduction in both the peeling and shearing stresses. At the high pressure, the peeling stress is essentially zero, while the shearing stress, although reduced, is still measurable. Since the softer stiffener configuration resulting from the short web leads to lower bending gradients in the flange termination region, the reduction in the peeling stress is somewhat expected.

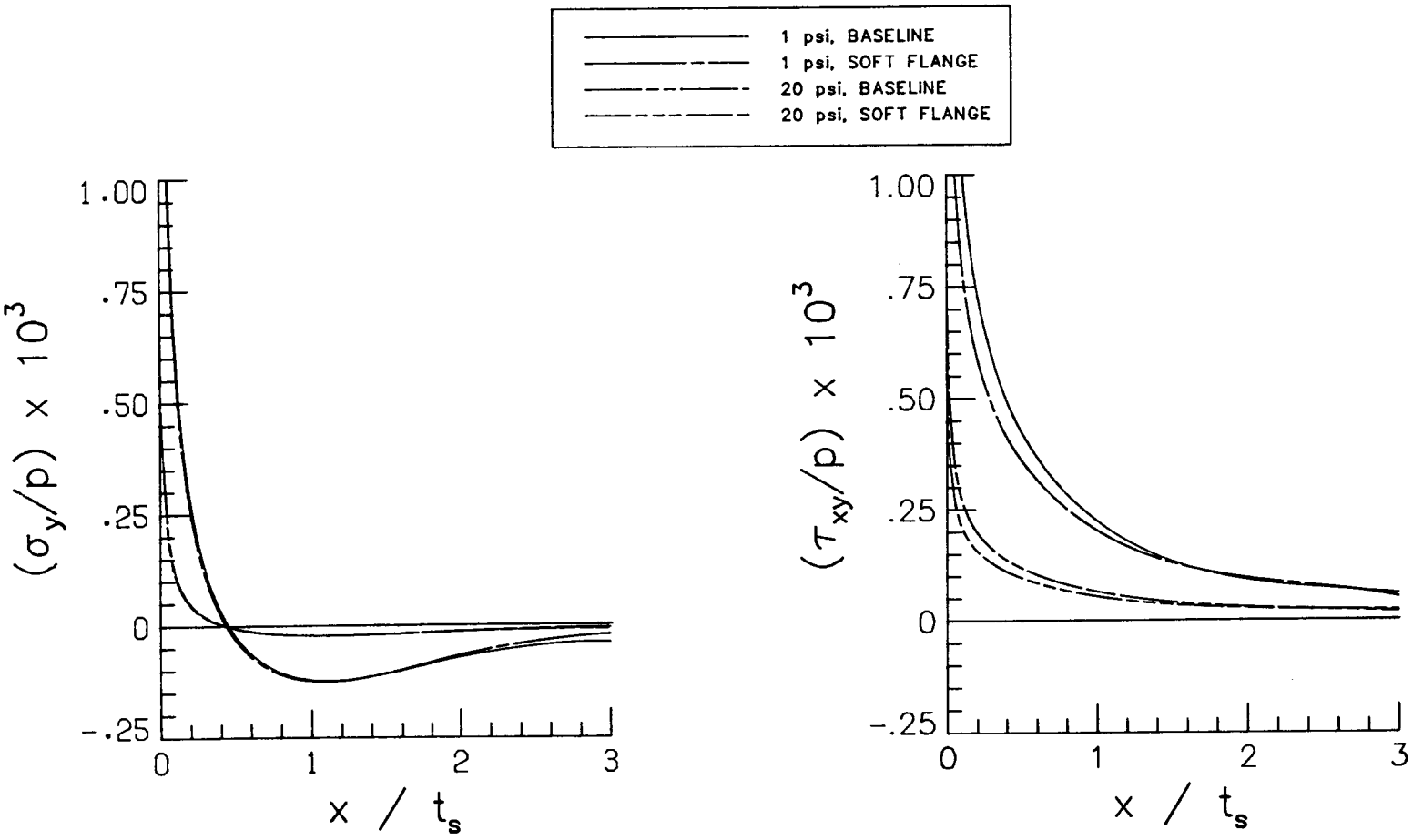

Figure 40. Influence of Softening the Flange on the Skin-Stiffener Interface Peeling, σ_y, and Shearing, τ_{xy}, Stresses.

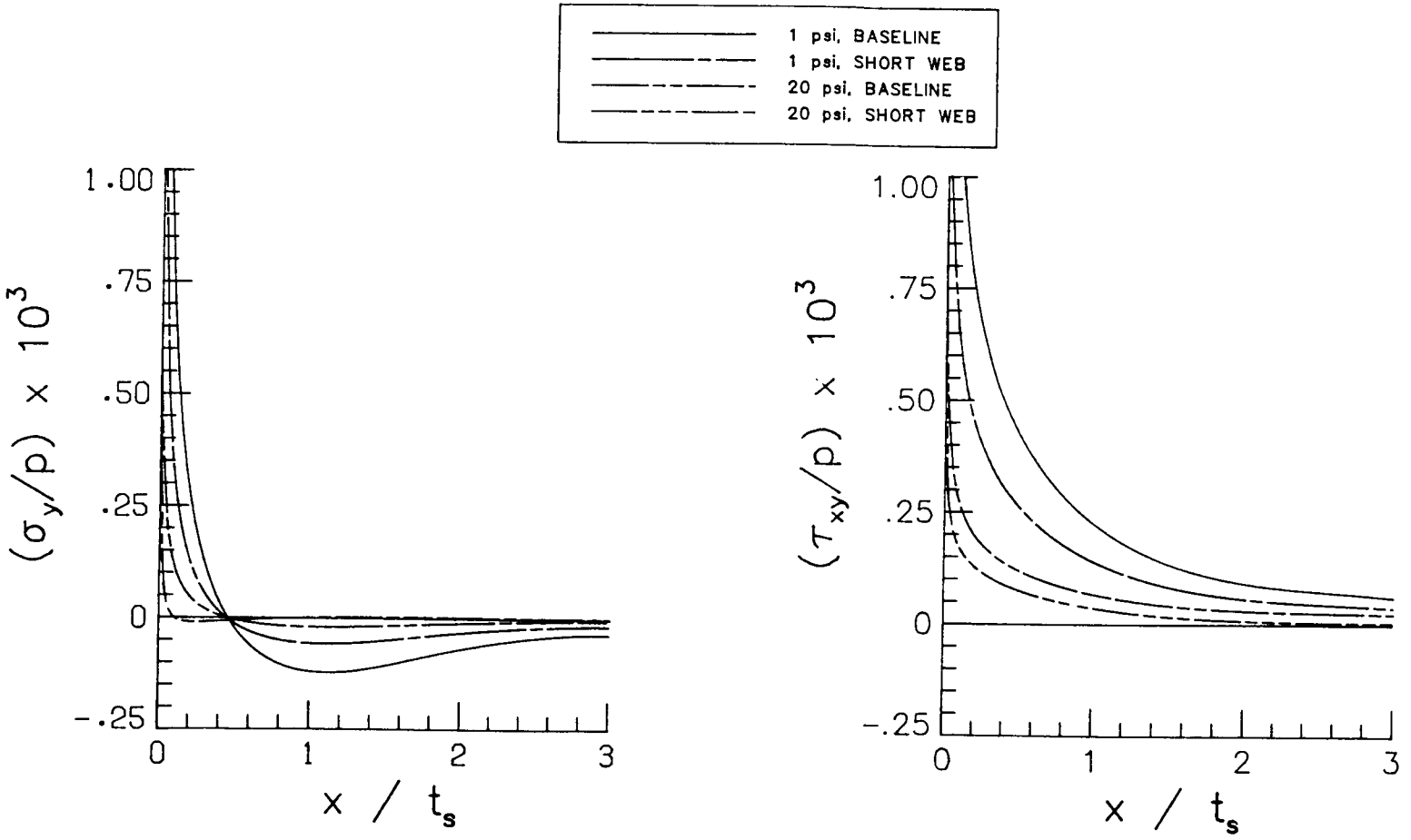

Figure 41. Influence of Shortening the Web on the Skin-Stiffener Interface Peeling, σ_y, and Shearing, τ_{xy}, Stresses.

Figure 42 illustrates the character of the peeling and shearing stresses for the baseline and "tapered flange" stiffener configurations. Tapering the flange seems to have a considerable effect on the interface peeling stress distribution. At both low and high pressures it appears that tapering tends to distribute the stress as a tensile stress over a larger portion of the skin-stiffener interface, rather than having a stress reversal accompanied by a steep gradient. This, in turn, may reduce the separation tendency of this particular stiffener design. Tapering of the flange seems to have a smaller influence on the interface shearing stress distribution. In general it tends to slightly increase τ_{xy} for both low and high pressure levels. Figure 43 demonstrates the influence of thickening the flange on the skin-stiffener peeling and shearing interface stresses. Generally speaking, thickening the flange tends to increase the interface peeling stress, increasing the gradient near the flange terminus and increasing the reversal away from this point. On the other hand, thickening the flange has a mixed effect on shearing stress. At high pressure the shear stress increases, while at low pressure the shear stress increases or decreases, depending on spatial location.

Figure 44 delineates the effect of softening and tapering the flange at the same time. An examination of Figure 42 and Figure 44 reveals that the peeling stress distributions for the tapered flange configuration and for the soft and tapered flange configuration are very similar. However, in the latter case the stresses appear to be lower, reflecting the influence of the combined changes to the baseline case. The shearing stress distribution seems to be lower, as compared to the baseline design, near the vertex and slightly higher away from the vertex.

Figure 45 displays a comparison between the baseline configuration and one for which the flange was thickened and tapered. If the results of Figure 45 are evaluated in the context of the results of Figure 43, it may be concluded that tapering the thick flange improves the distribution of the peeling stress along the interface, but has a smaller effect on the shearing stress distribution.

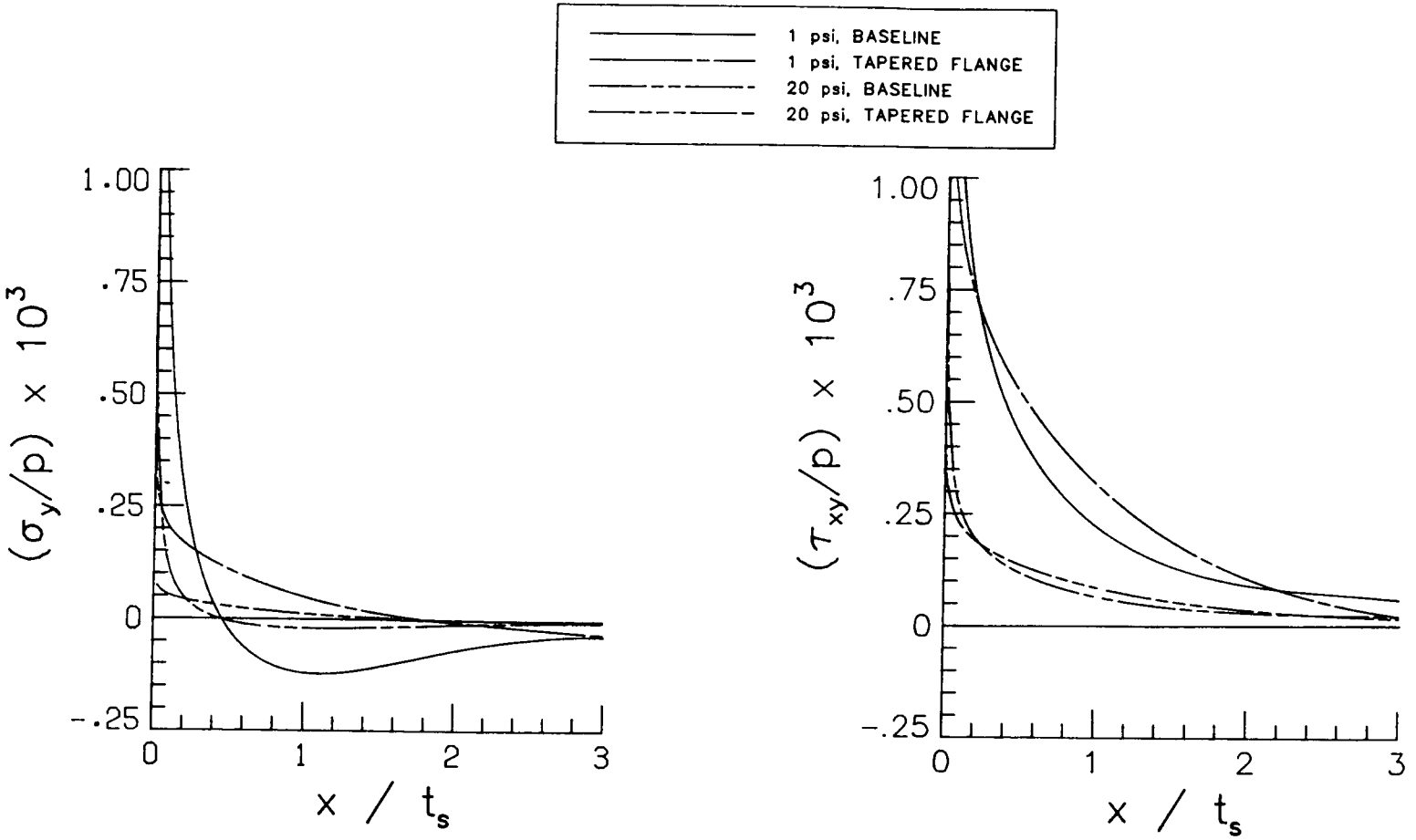

Figure 42. Influence of Flange Tapering on the Skin-Stiffener Interface Peeling, σ_y, and Shearing, τ_{xy}, Stresses.

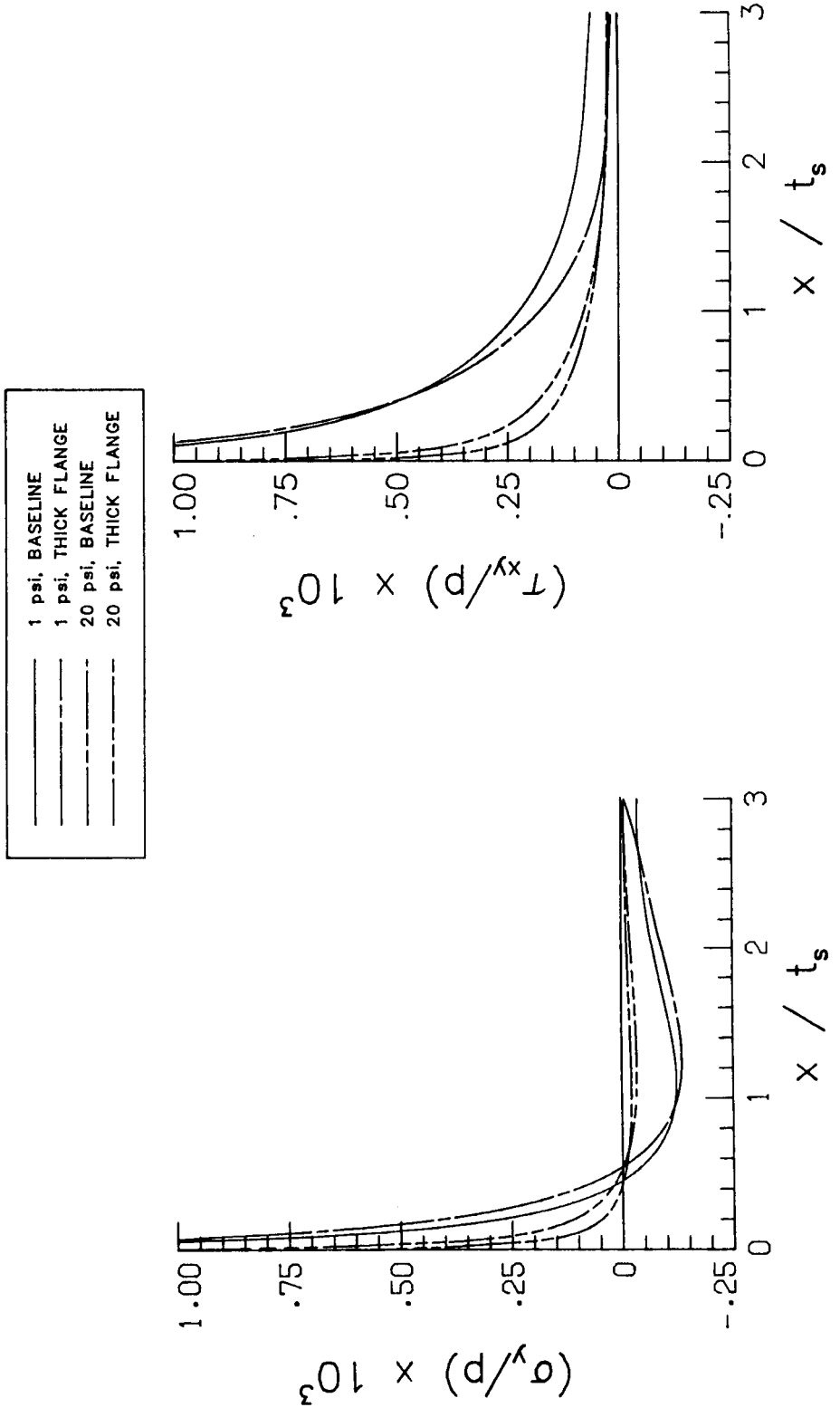

Figure 43. Influence of Thickening the Flange on the Skin-Stiffener Interface Peeling, σ_y, and Shearing, τ_{xy}, Stresses.

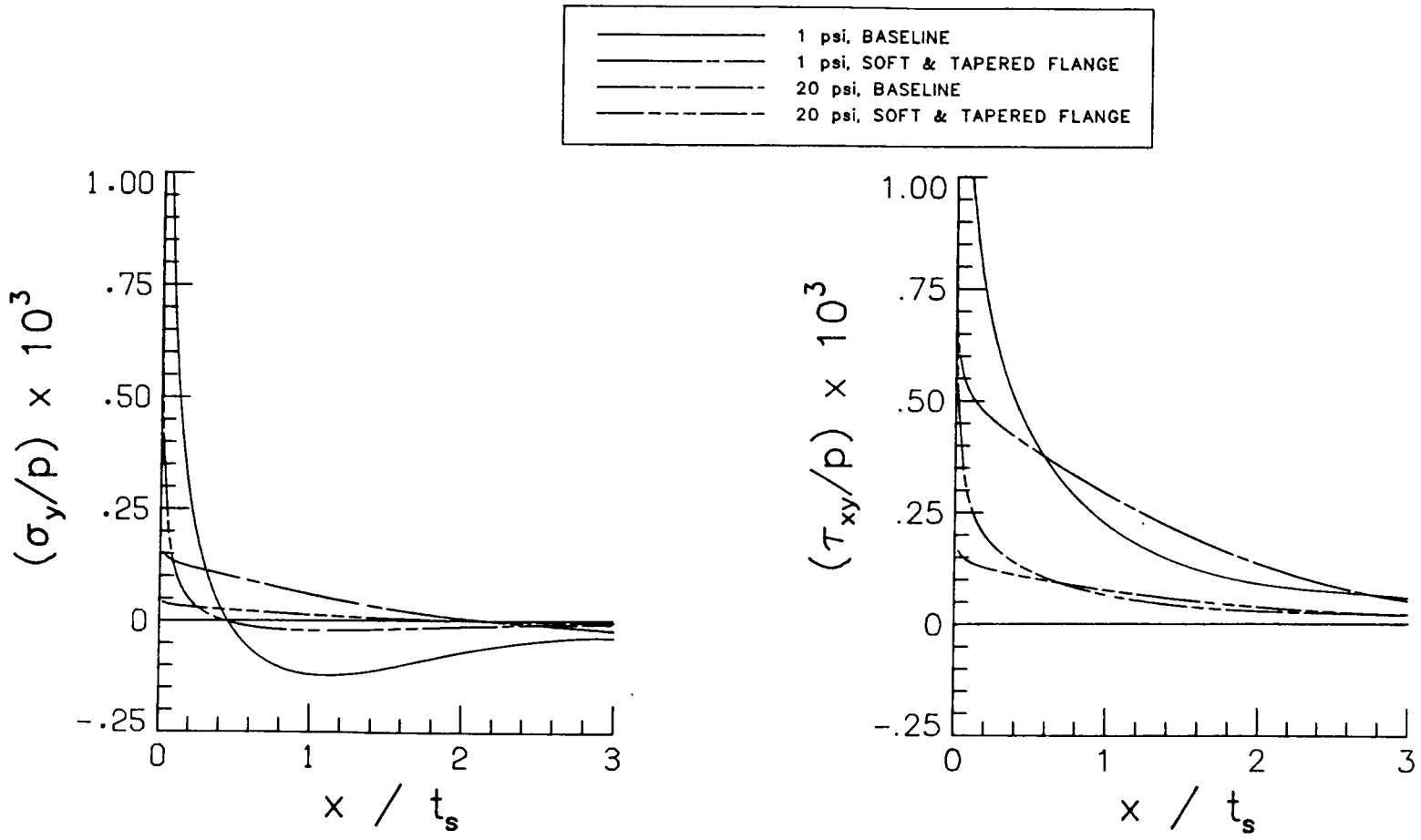

Figure 44. Influence of Softening and Tapering the Flange on the Skin-Stiffener Interface Peeling, σ_y, and Shearing, τ_{xy}, Stresses.

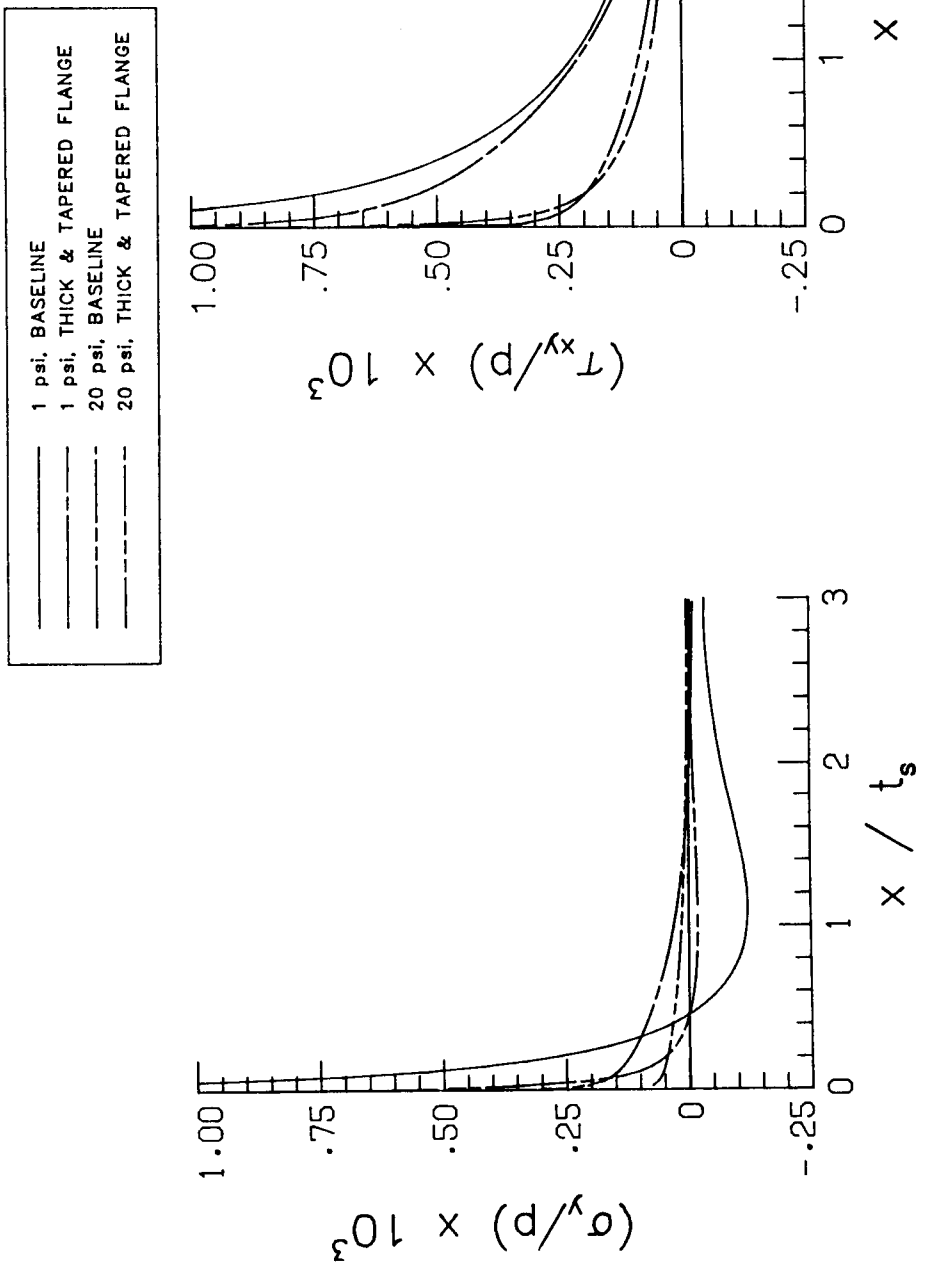

Figure 45. Influence of Thickening and Tapering the Flange on the Skin-Stiffener Interface Peeling, σ_y, and Shearing, τ_{xy}, Stresses.

Figure 46 depicts the influence of both thickening and softening the flange on the peeling and shearing interface stresses. Again, if one examines the results of Figure 46 in light of the data which were presented in Figure 43, it appears that softening the thick flange has little influence on the state of interface stresses as compared to the "thick flange" design. Therefore, the discussion offered for Figure 43 is also relevant for Figure 46. These results are also consistent with the results of Figure 40, where the baseline stiffener configuration was evaluated relative to a "soft flange" stiffener design of the same geometry. Finally, Figure 47 demonstrates the effect of thickening, softening, and tapering the flange on skin-stiffener interface peeling and shearing stresses. The following observations are made in connection with Figure 47: Softening the tapered thick flange does little to change the peeling stress distribution in the local region (compare Figure 45 with Figure 47). However, tapering the soft thick flange does substantially reduce the peel stress (compare Figure 46 with Figure 47). Finally, tapering the soft thick flange substantially reduces τ_{xy}. Based on the results of Figure 47 and the other figures, it can be stated that the single most important influence on the interface stresses is flange tapering. Softening the flange and reducing the thickness have considerably less influence.

At this point it is of interest to determined if the use of a single substructural analysis is sufficient for obtaining a local elasticity solution for both 90° and 15° flange termination angles. In section 2.6 it was shown that for the 90° and 45° flange termination angles, the local elasticity solution could be obtained from one substructural (or global) finite-element analysis for either 90° or 45° flange termination angles. However, some concern was raised as to whether these results are applicable for a very shallow flange termination angle. The results illustrated in Figure 48 provide insight into this. Figure 48 replicates the previous study of the 45° and 90° flange termination angles (Figures 18 and 19) but considers 15° and 90° angles instead. In Figure 48 the the pressure loaded stiffened plate and clamped boundary conditions used in the above parameter study are considered. The two stress components of interest, σ_y and τ_{xy}, are illustrated. The solid line in each portion of the figure represents the local

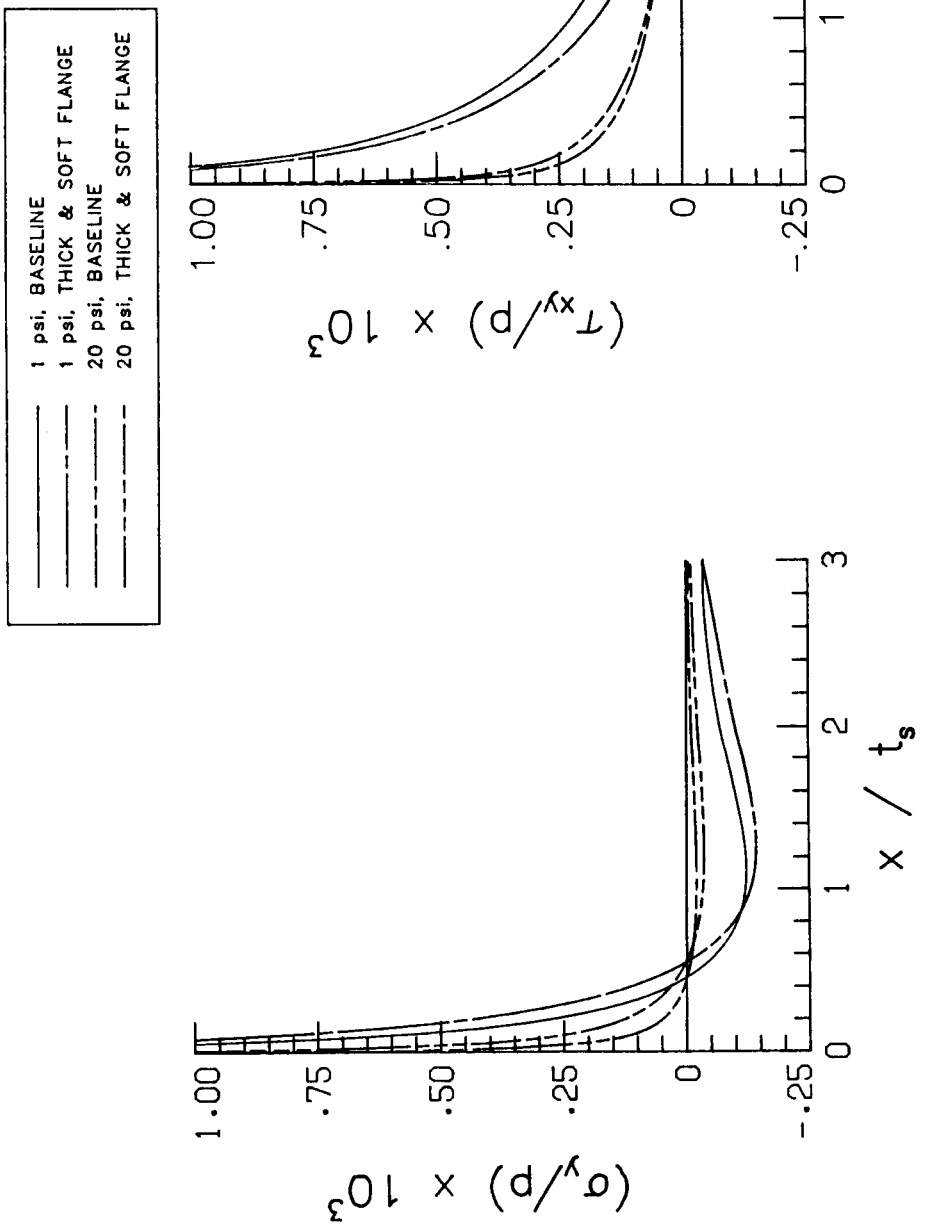

Figure 46. Influence of Thickening and Softening the Flange on the Skin-Stiffener Interface Peeling, σ_y, and Shearing, τ_{xy}, Stresses.

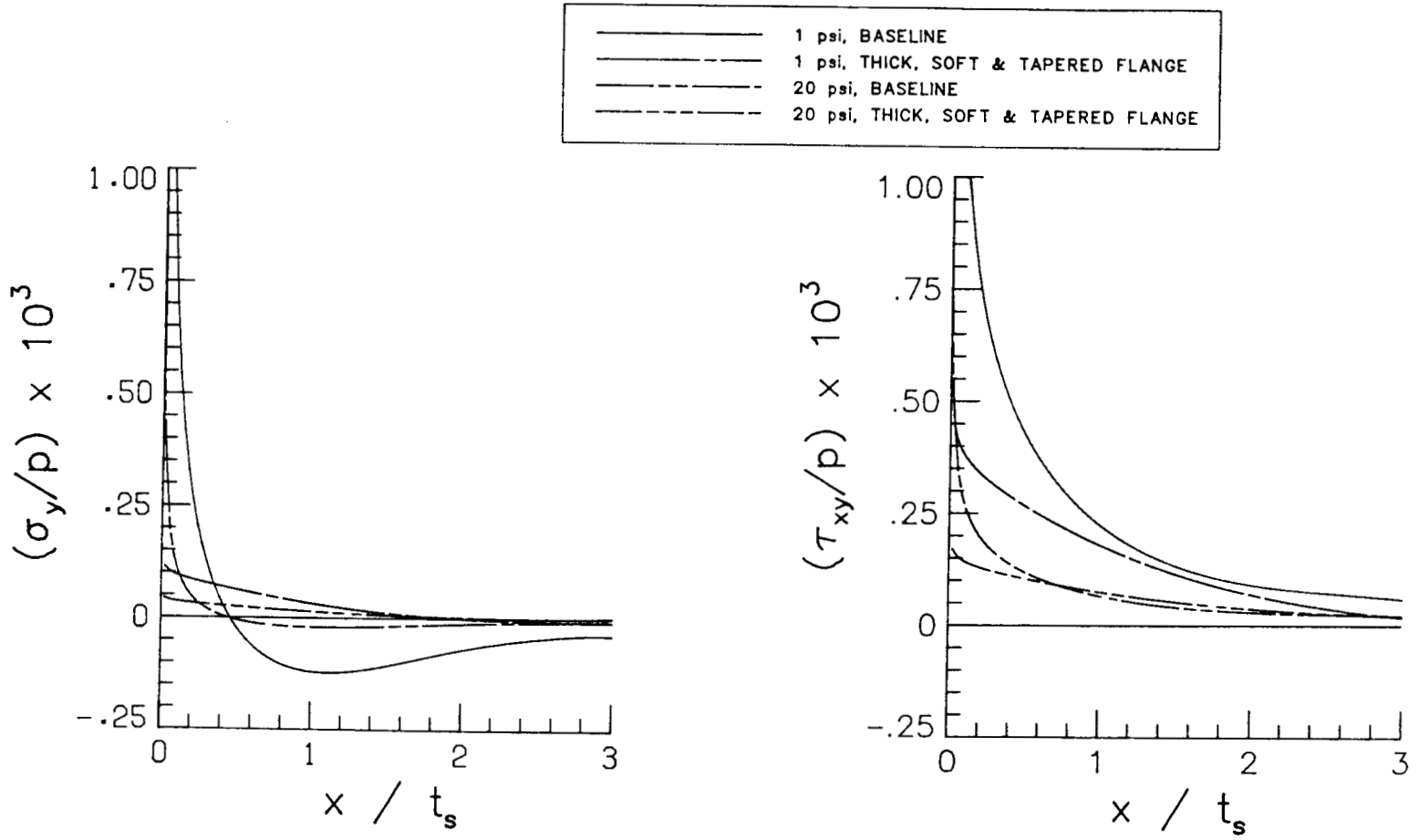

Figure 47. Influence of Thickening, Softening, and Tapering the Flange on the Skin-Stiffener Interface Peeling and Shearing Stresses.

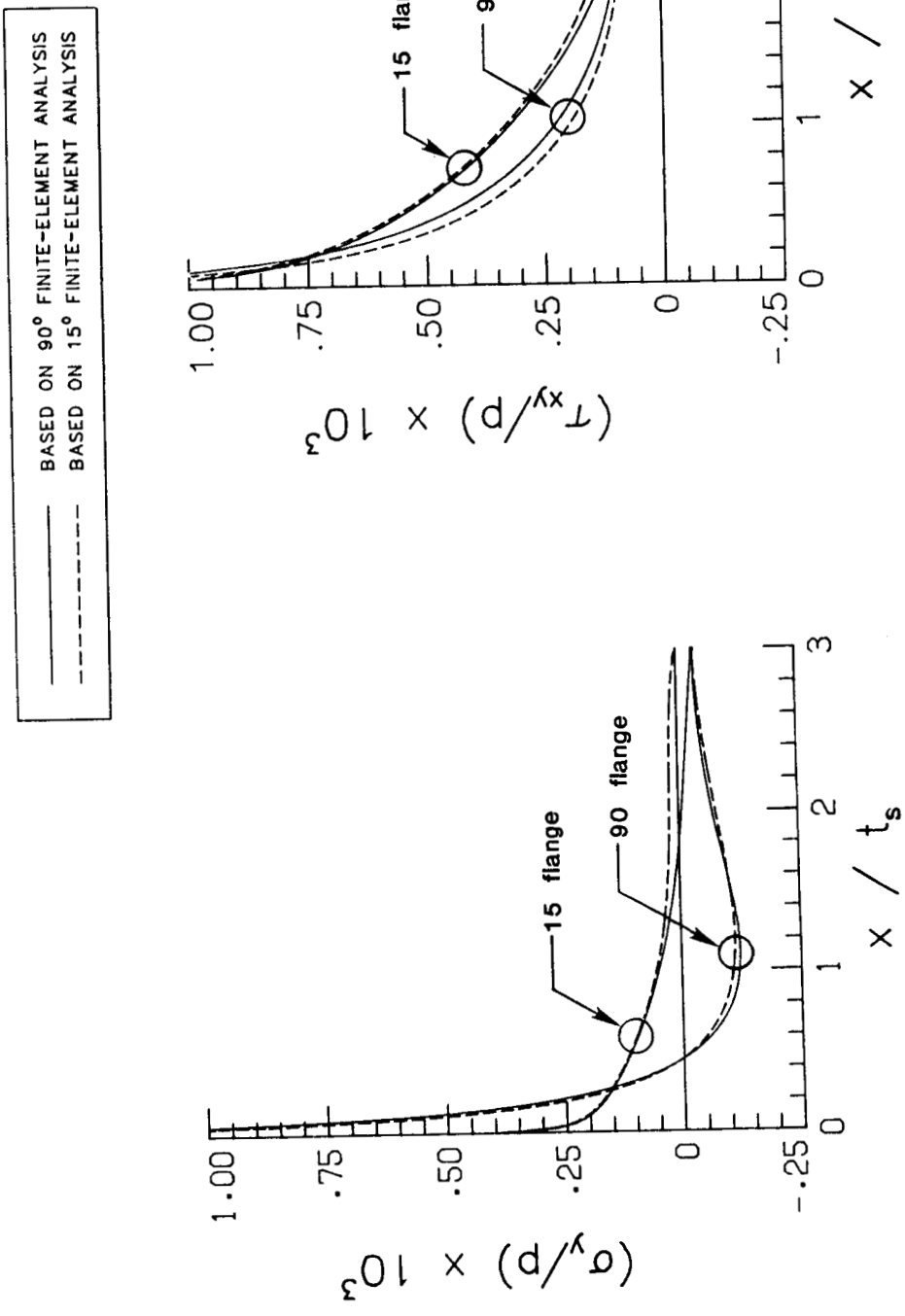

Figure 48. Skin-Stiffener Interface Peeling and Shearing Stresses for 90° and 15° Flange Termination Angles.

elasticity solution obtained from the collocation of stress data from the 90° flange termination angle substructure finite-element analysis. On each portion of the figure there are two solid line relations; one illustrates the local elasticity solution for a 90° flange, and the other illustrates the solution for a 15° flange. These curves are labeled "90° flange" and "15° flange", respectively. Similarly, the dashed lines on each portion of the figure represent the local elasticity solution obtained from the collocation of stress data from the 15° flange termination angle substructure finite-element analysis. There are two dashed line relations on each portion of the figure; one representing the local elasticity solution for the 90° flange, the other representing the local elasticity solution for the 15° flange. If the two curves which are labeled "90° flange" (i.e., the dashed and the solid lines) coincide, it is possible to use either the 90° or 15° finite-element analysis results to produce the same 90° flange elasticity solution. Similarly, if the two curves labeled "15° flange" coincide, the use of either 90° or 15° flange geometry finite-element analysis results to produce a 15° flange elasticity solution is justified. In general, the results of Figure 48 indicate that the level of agreement between the dashed and the solid lines for the same local elasticity solution produced by two different substructural analyses is not as good as the one observed in Figures 18 and 19. From a stiffener failure analysis point of view (discussed in the next section) the results of Figure 48 may be close enough. The worsening in agreement between the two approaches is directly related to the shallow flange termination angle, 15°. It is reasonable to expect that at very shallow flange termination angles, modeling the flange tapered portion in the substructural analysis is important. In addition, the results of Figures 18 and 19 are based on a linear analysis, whereas the present results are based on a geometrically nonlinear analysis. It is possible that the interaction between geometry and flange-skin interface response are more significant in the nonlinear range.

Lastly, a significant point of interest is the out-of-plane deformations observed in the various stiffened plate configurations. Figure 49 illustrates the plate deformation v at the center ($z=0$) as a function of transverse distance, x, for four stiffener configurations. These configurations

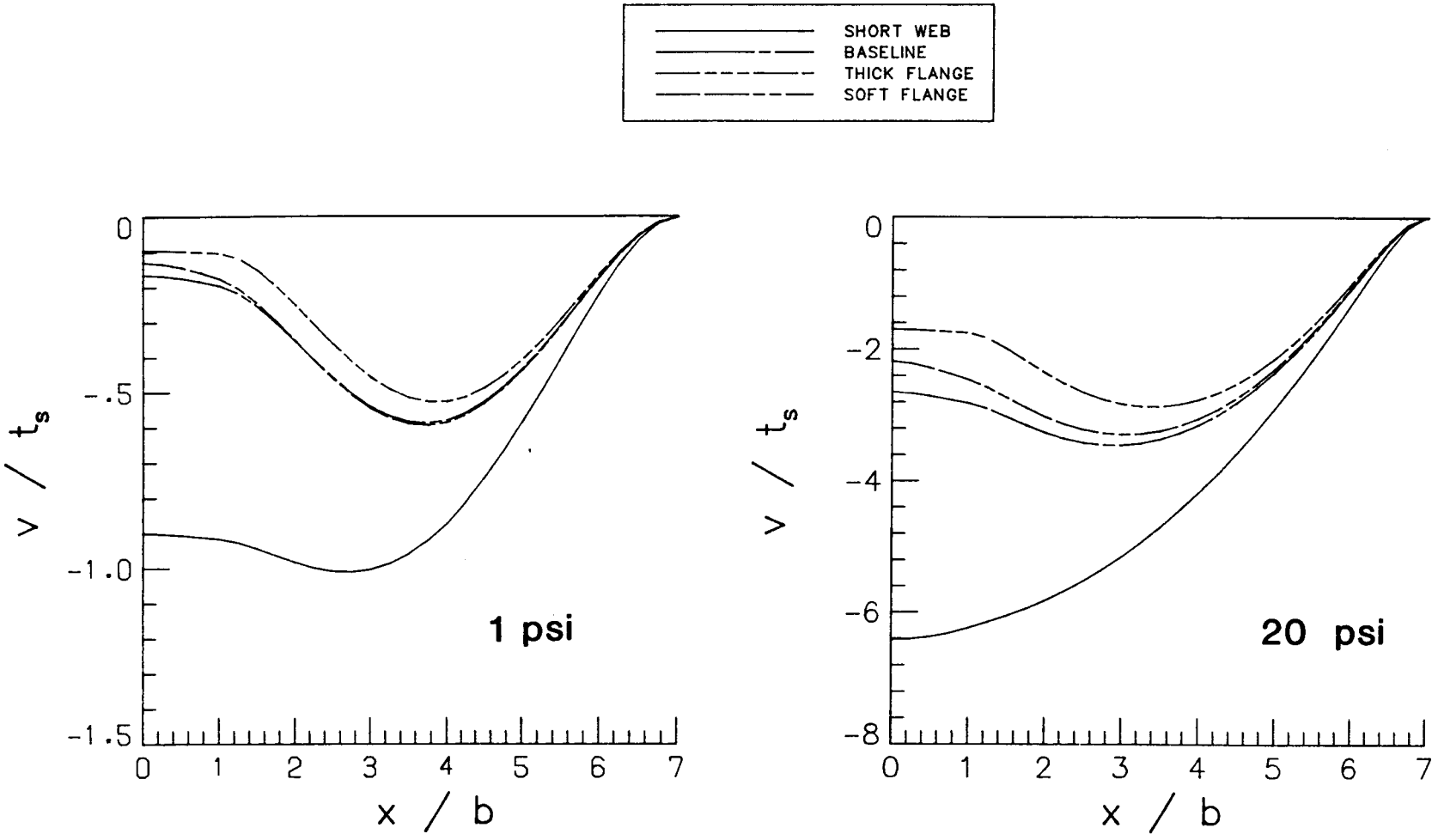

Figure 49. Out-of-Plane Deformation Response of the Various Stiffened-Plate Configurations (Plotted at z=0).

are: the baseline case, the short web case, the thick flange case, and the soft flange case. The figure demonstrates some important aspects of skin-stiffener interaction. Initially, at low pressure levels, all skin-stiffener configurations show a pillowing effect. At high pressure level, the short web stiffener configuration does not pillow. The other 3 stiffener configurations, however, exhibit pillowing at high pressure levels. However, there are differences among these three cases. The thicker flange stiffener geometry results in nearly a rigid body translation downward at the flange, i.e., v in the flange is practically independent of x. The soft flange, on the other hand, bends, its downward deflection increasing with increasing x. The baseline case represents a deformation characteristic between these two extremes. It should also be noted that the plate with the soft flange deflects less than the plate with the baseline flange. This is a consequence of the fact that in the soft flange configuration the 90° fibers in the baseline flange are converted into 0° fibers. Since it is assumed that the flange and web are of the same laminate, the switching of the 90° fibers to 0° fibers stiffens the web, thereby decreasing the overall deflection of the plate.

4.2.2 Stiffener Design Performance Evaluation

In the above, the influence of stiffener design parameters on skin stiffener interaction have been examined from a qualitative point of view. In the following section, these effects are studied quantitatively. Interest here is in presenting numerical values by which a particular skin-stiffener design may be judged in terms of its tendency to experience skin-stiffener separation failure. The results are presented relative to the baseline configuration. In the results to be presented, two stress parameters are used, the stress eigenfactor (SEF), mentioned previously, and the average stress factor (ASF).

The peeling, K_y, and shearing, K_{xy} stress eigenfactors, were defined by eq. 70.a and 70.b, respectively. In the present investigation the SEF concept is used as a measure of the severity in interaction between the stiffener and the skin, rather than as a failure criteria. A stiffener design which leads to a high SEF, relative to a baseline configuration, will be judged as having more tendency to separate. Similarly, a stiffener configuration which produces a lower SEF, relative to a baseline design, will be judged as having less tendency to separate. For example, if tapering the flange of the baseline configuration leads to lowering the SEF, then reducing the stiffener termination angle will be judged as a design improvement for the stiffener. Here care must be taken in evaluating the results. Changing one stiffener parameter my lead to a reduction in K_y but an increase in K_{xy}, or vice versa. This raises the question of which SEF is more significant in the initiation of skin stiffener separation K_y or K_{xy}. Here it can only be said that epoxy resins and adhesives usually exhibit higher shearing strength relative to peeling strength. Therefore, it is reasonable to speculate that K_y will be more important in determining the tendency for skin stiffener separation.

While the concept of a stress eigenfactor has been used successfully in the field of fracture mechanics (i.e., stress intensity factor) in isotropic materials as a parameter by which the initiation of crack growth and fracture can be determined, this concept has proven to be less useful in composite materials. This may be related to the heterogeneity of the material and the complex nature of crack propagation. In the skin-stiffener separation initiation context, there is no evidence for the existence of crack at the flange terminus prior to failure. Therefore, the use of the average stress factor in determining skin-stiffener interface strength may be more appropriate. For the present problem, the average stress factors are defined by;

$$S_y = \frac{1}{a_o} \sum_{i=1}^{n} \int_0^{a_o} \sigma_y (x, 0, ; \lambda_i) \, dx \quad , \qquad [71.a]$$

$$S_{xy} = \frac{1}{a_o} \sum_{i=1}^{n} \int_0^{a_o} \tau_{xy} (x, 0, ; \lambda_i) \, dx \quad , \qquad [71.b]$$

where λ_i is the i'th eigenvalue in the truncated eigenfunction expansion. The parameter a_o is the distance of integration along the flange interface from the flange terminus. Failure is based on critical values for S_y^{cr} and S_{xy}^{cr} for a particular material. These must be determined experimentally. The average stress criteria was first proposed for use in composite structure applications in [45]. In that study the criteria was applied to the calculation of laminates strength which contained holes and notches. More recently this concept was used in the investigation of the onset of delamination in composite laminates [46]. In that study the average stress criteria produced fairly good agreement with experimental results. The investigators postulated that the onset of delamination was strictly controlled by interlaminar transverse strength and therefore used S_y only. The integration length was taken as $\frac{a_o}{t_l} = 1$ (t_l being the lamina thickness) and S_y^{cr} was equal to the transverse strength of the composite. Due to the lack of experimental data, the average stress criteria in the present investigation is used as an additional parameter by which the different stiffener designs are evaluated. It is anticipated that both the SEF and the ASF will produce qualitatively similar results.

Finally, it is recognized that skin-stiffener designs cannot be judged solely by their tendency to separate. Therefore, in addition to the stress parameters, the maximum skin and the center-of-plate out-of-plane deformation are given. This is to point out that a particular stiffener design may lead to a 50% reduction in K_y and K_{xy} but an increase of 2 to 3 times in the out-of-plane deflection. Such designs would be desirable from the skin-stiffener separation stand point, but may be unacceptable from the structural deformation point of view.

Table 3 presents quantitative data relevant to the stiffener parametric study. The data given in the table is based on a 1 and a 20 psi pressure nonlinear analysis. The first column lists the stiffener configurations by their nicknames. The second column gives the two pressure levels. Columns 3 and 4 give the peeling and shearing stress eigenfactors, K_y and K_{xy}. Columns 5 and 6 provide the peeling and shearing average stress factors, S_y and S_{xy}, for an integration distance of $a_o/t_s = 0.0625$. This value of a_o corresponds to one lamina thickness for the materials considered here. Finally, columns 7 and 8 list values for the maximum skin and the center-

Table 3. Stiffener Parametric Study Results.

Stiffener Configuration	Pressure (psi)	K_y	K_{xy}	S_y	S_{xy}	v_s	v_f
B. Soft Flange	1	1.047	0.820	0.929	0.748	1.011	0.786
	20	1.043	0.816	0.924	0.747	0.954	0.825
C. Short Web	1	0.573	0.573	0.533	0.594	1.726	5.462
	20	0.510	0.510	0.244	0.590	1.494	2.423
D. Tapered Flange	1	0.607	4.075	0.172	0.639	1.000	1.000
	20	0.673	4.153	0.210	0.662	1.000	1.000
E. Thick Flange	1	1.161	1.161	1.221	1.116	0.896	0.576
	20	1.522	1.522	1.683	1.423	0.830	0.641
F. Soft & Tapered Flange	1	0.511	3.487	0.100	0.343	1.011	0.786
	20	0.628	3.975	0.126	0.367	0.954	0.825
G. Thick & Tapered Flange	1	0.464	3.112	0.128	0.482	0.896	0.576
	20	0.690	4.630	0.216	0.679	0.830	0.641
H. Thick & Soft Flange	1	1.322	1.035	1.259	0.897	0.893	0.449
	20	1.769	1.384	1.789	1.168	0.797	0.514
I. Thick, Soft, & Tapered Flange	1	0.416	2.634	0.074	0.257	0.893	0.449
	20	0.645	4.083	0.129	0.376	0.797	0.514

of-plate out-of-plane deflections, v_s and v_f, respectively. All values which are given in Table 3 are normalized by the values calculated for the baseline configuration. Table 3 presents an enormous amount of data that can be compared in ways that are too numerous to be done here. However, two types of comparisons can be done, namely comparison resulting from softening, tapering, and thickening the baseline flange, and softening and tapering the thick flange. These comparisons will be made in the following paragraphs.

Examination of the SEF data lead to the following observations: softening the flange (i.e., reducing the transverse modulus E_x) tends to increase K_y, in both the baseline and thick flanges. This increase is more significant in the thick flange, as can be seen by a comparison between the SEF for the "thick flange" and the "thick and soft flange" configurations. On the other hand, softening the flange leads to a reduction in K_{xy} in both the baseline and thick flanges. For the soft flange, the reduction is 20% relative to the baseline case. Shortening the web, to half the height of the baseline configuration, results in drastic a decrease in both the peeling and shearing stress eigenfactors. Though not as dramatic, tapering the flange leads to a 30% or more reduction in K_y in the baseline case. For the thick flange configuration tapering leads to even greater reduction in K_y. However, this same design change leads to large increases in K_{xy} Thickening the flange brings about an increase of up to 50% in both K_y and K_{xy} at 20 psi pressure. This increase happens even though the values of the engineering constants are the same for the two flanges (see Appendix D). Softening the tapered flange helps reduce K_y and K_{xy} by a moderate amount. This reduction amounts about 15% decrease in K_y and K_{xy}, respectively, for the thick flange at 20 psi pressure. A smaller decrease is observed at a lower pressure and for the baseline flange configuration. On the other hand, tapering the soft flange substantially reduce K_y in both the baseline and thick flanges configurations. This design change brings about a 50% reduction in K_y, for the baseline flange at both 1 and 20 psi pressure. The same design change leads to about 65% reduction in K_y at 1 and 20 psi pressure in the thick flange configuration. However, tapering the soft flange leads to a drastic increase in the shearing stress eigenfactor in both the baseline and thick

flange configurations. This increase is similar in magnitude to the increase due to tapering alone. Based on the SEF data presented, the following general comments can be made: (a) Softening the flange leads to slight increases in K_y and moderate decreases in K_{xy}; (b) Tapering the flange brings about a drastic reduction in K_y but a substantial increase in K_{xy}; (c) Thickening the flange leads to up to a 50% increase in K_y and K_{xy}; and (d) Shortening the web heights to half the baseline web height results in nearly 50% reduction in both K_y and K_{xy}.

The average stress factor produces results which, for the most part, are consistent with the SEF data. However, there are some inconsistencies.These are discussed next. The ASF, unlike the SEF, indicates that softening the flange leads to slight decrease in peel tendency. However, the difference between the two measures is quite small, 5% increase in K_y verses 8% decrease in S_y. Another inconsistency relates to the values of K_{xy} and S_{xy} for the "thick & soft flange" configuration at 1 psi pressure. For this configuration K_{xy} is 4% higher than the baseline design, whereas S_{xy} is 10% lower. However, it should be noted that softening the thick flange produces the same trend in both the SEF and the ASF. That is, both K_y and S_y increase due to softening, whereas K_{xy} and S_{xy} decrease due to softening. Finally, in the SEF calculation, tapering the flange leads to an increase of 3 to 4 times in K_{xy} relative to the baseline configuration. The ASF shows a decrease in S_{xy} relative to the baseline stiffener design. As a matter of fact, all the stiffener configurations except the "thick flange" and the "thick & soft flange" designs produce S_{xy} which is smaller than the baseline case. These results are consistent with the observations made in Figure 40 through Figure 47. The average stress, of course, will depend on the distance of integration, a_o. For example, if the "tapered flange" configuration, Figure 42, is considered, it is obvious that extending the integration distance to, say, $a_o/t_s = 1$ would result in different values for both S_y and S_{xy}. This is what makes the SEF so useful in evaluating the effects of various stiffener parameters on skin stiffener interaction. The SEF is independent of any objective parameter such as a_o. On the other hand, the ASF may be useful in determining the skin stiffener separation failure initiation. This can only be achieved with experimentally determined value for S_y^{cr} and S_{xy}^{cr}.

Finally, an examination of the out-of-plane deflections for the various stiffener designs shows that, relative to the baseline case, all configurations, except for the "short web" design, give the same or smaller out-of-plane deflections for the center-of-plate and the skin. Although the "short web" stiffener design leads to a substantial reduction in both the peeling and shearing stresses in the local region, it results in a large increase in the out-of-plane deflections.

In summary, if the stress data is considered together with the out-of-plane deflections, it may concluded that: (a) If a thick flange is used to increase structural rigidity, tapering and softening the flange will substantially reduce the risk of premature skin-stiffener separation; (b) Softening the flange (i.e., putting more 0° fibers in the z direction) leads to a decrease in the center-of-plate out-of-plane deflection but a relatively small gain as far as interface stresses are concerned; and (c) Tapering the flange results in a small or nonexistent effect on the out-of-plane deformation but substantially reduces the risk of premature skin-stiffener separation.

This concludes the quantitative evaluation of the performance of stiffener design parameters. In the next chapter some conclusions are put forth and recommendations for future research, as related to skin-stiffener interaction, are discussed.

5. Conclusion and Recommendations

5.1 Concluding remarks

In the following chapter, the work conducted in the present study is summarized. In addition, some recommendations for future research are highlighted.

As stated in the introduction, the objective of the investigation was to develop an analytical method by which skin-stiffener interface stresses could be accurately calculated. Particular attention was given to the flange termination region, a region where the stresses are high due to geometric and material discontinuity associated with this locality. Moreover, the stresses in this region are generally difficult to compute and so extra attention was given to this area of the interface. Furthermore, since stiffened panels are most commonly designed to operate at the postbuckling range, the analysis had to incorporate geometrically nonlinear effects. Considering the above, the following objectives were set:

(a) The analytical model should accurately represent the state of stress near the point of geometric and material discontinuity.

(b) The analysis should include geometric nonlinearities.

(c) The procedure should be applicable to general stiffened composite panels.

(d) The model should be sensitive to various skin and stiffener design parameters, such as stiffener geometry, and stiffener/skin material architecture.

The method developed addressed all of the above objectives. In Chapter 2 the first objective was addressed. This led to the development of a local-global analysis procedure, later called the local-substructure analysis procedure. The developments in this chapter were for geometrically linear analyses. The local elasticity analysis was based on the eigenvalue expansion of the stress function. The eigenvalue expansion was applicable in the flange termination region and as a result, the stresses were known to within a set of arbitrary, but unknown, coefficients which were associated with the eigenvalues. For a particular skin-stiffener problem, these coefficients were determined from the stresses obtained from a combination of a global finite-element analysis of the entire skin-stiffener cross-section and a collocation scheme. Once these constants were known, the stresses in the localized region could be uniquely determined. The local elasticity solution provided a rigorous solution which accurately characterized the material and geometric discontinuities associated with the flange termination region. Away from this region the global finite-element analysis produced accurate skin-stiffener interface stresses. The last part of Chapter 2 was devoted to the study of convergence and accuracy of the local elasticity solution. The accuracy issue was investigated by comparing the local elasticity solution with finite-element results for which the mesh was refined twice. The use of finite elements for comparison was due to the lack of another analysis of this particular problem. In general, it was found that the local elasticity solution scheme produced a very accurate interface stress representation in the flange termination region. Convergence of the local elasticity solution was studied by varying the number of eigenvalues in the truncated eigenvalue expansion, and by varying the number of the collocation points on the local region boundary. Generally, it was found that the use of 10 to 15 eigenvalues, in

the eigenvalue expansion, and 100 collocation points resulted in a converged local elasticity solution.

In Chapter 3 the second and third objectives were addressed. In the first part of the chapter the local elasticity solution was extended to include geometrically nonlinear effects. Here the condition of small strains but finite rotations was assumed. It was shown that under these conditions, in a local region which undergoes spatially uniform rotations, the local elasticity solution procedure developed in Chapter 2 was valid, provided it was applied in the deformed body configuration. This approach was applied to an actual stiffened composite plate structure where both geometrically linear and nonlinear analyses were considered. The analysis of the entire structure consisted of three steps: a structure analysis, a substructural analysis, and a local elasticity analysis. First a structural level analysis of the entire stiffened plate was conducted using finite-element plate elements. Next, a typical cross-section region in the stiffened plate structure was isolated and a three dimensional finite-element analysis of the cross-section was performed. Finally, the stresses from the substructural analysis were coupled with a boundary collocation scheme to produce a rigorous elasticity solution in the flange termination region.

Finally, in Chapter 4 both the third and the fourth objectives were addressed. In this chapter the influence of geometric nonlinearities on skin-stiffener interface stresses was evaluated. The interest here was focused on determining what error would be encountered if a geometrically linear, rather than a geometrically nonlinear analysis was used in the computation of skin-stiffener interface stresses. In general, it was found that in flexible stiffened skin structures, which exhibit out-of-plane deformations on the order of magnitude of 2 to 4 times the skin thickness, geometrically nonlinear effects in the calculation of interface stresses are very important. That is, the use of geometrically linear analysis, rather then nonlinear analysis, can lead to considerable error in the computed interface stresses. In the last part of the chapter the influence of stiffener design parameters on the skin-stiffener interface stresses was studied. Both geometric and material stiffener parameters were considered. The stiffener

parametric study included eight different stiffener configurations. In general, it was found that the local elasticity analysis was sensitive to the various stiffener design changes and provided very useful information by which these designs could be evaluated against a baseline stiffener configuration. The findings suggest that tapering and softening the flange simultaneously tends to reduce interface peeling stress in the local flange termination region. However, these same design modifications tend to increase the shearing stress in this locality. Since it is believed that the stiffener separation failure is strongly related to the state of peeling stress at the flange termination region, the use of flange tapering and softening may prove beneficiary in this respect. Finally, use was made of the peeling and shearing stress eigenfactors (SEF) in evaluating the performance of the various stiffener designs against a baseline configuration. Another stress parameter used was the average stress factor (ASF). Both the SIF and the ASF could be calculated in a closed form from the truncated eigenvalue expansion elasticity solution.

As summarized above, all the objectives were addressed by the method developed in this study. The results demonstrated that this analytical tool is accurate and sensitive in solving skin-stiffener interface stress problems in actual stiffened composite skin aircraft structures.

5.2 Recommendations for future research

The method developed produced accurate and useful skin-stiffener interface stress calculations for stiffened composite skin aircraft structures. However, the analytical model was based on certain assumptions which restricted its application to the most general skin-stiffener interface problems. In this section recommendations are made related to the capability enhancement of the current model to a more general one. Other recommendations are related to analysis cost reduction, and to analytical and experimental correlation of stiffener

separation predictions. The recommendations are divided into two categories, one which relates to analytical development and the other is related to experimental considerations.

5.2.1 Analytical Recommendations

(a) In the present investigation the skin and stiffener were restricted to symmetric balanced laminates. This, in conjunction with the integrated laminate properties assumption, led to orthotropic material constitutive relations. As a result, material stretching and bending and/or twisting coupling effects were ignored. For most stiffened composite skin aircraft structures such a simplification is justified. However, there are some cases in which the use of unbalanced or unsymmetric laminates for the skin and/or the stiffener is desirable. Hence, to render the present analytical tool more general, the local elasticity solution should be extended to include more general material constitutive law. It should be noted that for more general material characteristics, the two stress functions, F(x,y) and Ψ(x,y) are coupled. However, in general, the solution approach is the same (see refs. 21 and 22). In that regard, it should be mentioned that for the cases studied here, τ_{yz} and τ_{xz} were identically zero.

(b) In the present investigation it was assumed that the stress components did not vary with z. This restriction is justified for most instances over short distance in the z direction where the local elasticity solution is applied. However, there are some cases in which the stresses, and in particular σ_z , do vary rapidly with z. In such cases the local elasticity solution can be modified to include a linear variation in σ_z with z (see ref. 22). The solution procedure to such a case is similar to the one presented here.

(c) Finally, in the present analysis procedure use was made of the substructural analysis of the skin-stiffener cross-section. The primary function of this step was to generate the boundary conditions for the local elasticity analysis, as well as for the computation of skin-

stiffener stresses outside of the local region. If the sole purpose of this step is only to generate boundary conditions, it would be advantageous from a cost standpoint to eliminate this step. One way by which the above may be achieved is by using laminated plate theory to compute the stresses on the local region boundaries using the inplane loading from the structural analysis. By doing so the local elasticity analysis can be incorporated as a post-processor in a structural analysis program.

5.2.2 Experimental Recommendations

(a) The lack of experimental data makes it impossible to evaluate the usefulness of the present analytical approach in determining the initiation of skin-stiffener separation failure. Therefore, it is recommended that stiffener-skin specimens configurations will be tested to failure under various loading conditions to obtain skin-stiffener interface strength, S_y^{cr} and S_{xy}^{cr}.

(b) Once critical values of the failure parameters are known, they can be used as input to make analytical failure predictions of actual skin-stiffener structures. For example, using the experimental devise describe in [10] for testing single stiffener pate configuration subjected to uniform transverse pressure, a comparison can be made between analytical prediction and experimental results.

6. References

1. Starnes, J.H., Jr. and Knight, N.F., Jr., " Postbuckling behavior of selected flat stiffened graphite-epoxy panels loaded in compression," AIAA Paper No. 82-0777, presented at the AIAA/ASME/ASCE/AHS 23rd SDM Conference, 1982.

2. Knight, N.F, Jr and Starnes, J.H., Jr., " Postbuckling behavior of selected curved stiffened graphite-epoxy panels loaded in compression," AIAA Paper No. 85-0768, presented at the AIAA/ASME/ASCE/AHS 26th SDM Conference, 1985.

3. Knight, N.F., Jr. and Stroud, W.J., "Computational structural mechanics: A new activity at the NASA Langley Research Center," NASA TM 87612, Sept. 1985.

4. Lotts, C.G., Green, W.H., McCleary, S.L., Knight, N.F., Jr., Paulson, S.S., and Gillian, R.E., " Introduction to the Computational Structural Mechanics Testbed,", NASA TM 89096, September 1987.

5. Wang, J.T.S. and Biggers, S.B., " Skin/stiffener interface stresses in composite stiffened panels," NASA Contract Report 172261, 1984.

6. Goland, M. and Reissner, " The stresses in cemented joints," J. of App. Mech. , 1, 1 (1944) p. A-17.

7. Yuceoglu, U. and Updike, D.P., " Stress analysis of bonded plates and joints," J. Eng. Mech. Div. , 106, (1980) p. 37.

8. Williams, J.H., Jr., " Stresses in adhesive between dissimilar adherents, " J. Adhesion , 7, (1975) p. 97.

9. Delale, F., Erdogan, F., and Aydinoglu, M.N., " Stresses in adhesively bonded joints: A closed-form solution," J. of Composite Materials , 15, (1981) p. 249.

10. Loup, D.C., Hyer, M.W. and Starnes, J.H., Jr., " Stiffened skin interaction in pressure loaded composite panels," AIAA Paper No. 86-0917, presented at the AIAA/ASME/ASCE/AHS 27th SDM Conference.

11. Williams, M.L, " Stress singularity resulting from various boundary conditions in angular corner of plates in extension," J. of App. Mech., 19, 4 (1952) p. 526.

12. Gross, B., Srawley, J.E. and Brown, W.F., " Stress intensity factors for single edge notch tension specimen by boundary collocation of stress function," NASA TN D-2395 1964.

13. Gross, B. and Srawley, J.E., " Stress intensity factors for three points bend specimen by boundary collocation," NASA TN D-3092 1965.

14. Gross, B. and Srawley, J.E., " Stress intensity factors by boundary collocation method for single-edge-notch specimens subjected to splitting forces," NASA TN D-3295 1966.

15. Gross, B. and Srawley, J.E., " Stress intensity factors for crackline-loaded edge-crack specimens," NASA TN D-3820 1967.

16. Gross, B. and Mendelson, A. " Plane elastostatic analysis of v-notched plates," Int. J. of Fracture Mech. , 8 (1972) p. 267.

17. Carpenter, W.C., "Calculation of fracture mechanics parameters for general corner," Int. J. of Fracture Mech. , 24 (1984) p. 45.

18. N.I., Muskhelishvili, Some Basic Problems of the Theory of Elasticity, 4th edn., Noordhoff International Publishing, Leyden, 1975.

19. Williams, W.L., " The stress around a fault or crack in dissimilar media, " Bull. Seism. Soc. Am. , 49, 2 (1959) p. 199.

20. Bogy, D.B., " Two edge-bonded elastic wedges of different materials and wedge angles under surface traction, " J. of App. Mech. , 38, 2 (1971) p. 377.

21. Wang, S.S. and Choi, I., " Boundary layer effects in composite laminates: Part I - Free edge Stresses, " J. App. Mech. , 49 (1982) p. 541.

22. S.G., Lekhnitskii, Theory of Elasticity of an Anisotropic Body, Holden-Day, San Francisco, 1963.

23. Wang, S.S. and Choi, I., " Boundary layer effects in composite laminates: Part II - Free edge stresses, " J. App. Mech. , 49 (1982) p. 549.

24. Wang, S.S., Elasticity solution for a class of composite laminate problems with stress singularity, In Mechanics of Composite Materials , Edited by, Z., Hashin and C.T., Herakovich, Pergamon Press, NY, 1982.

25. Delale, F., " Stress singularity in bonded anisotropic materials," Int. J. Solids Structures , 20, 1 (1984) p. 31.

26. Ting, T.C.T., and Chou S.C., " Edge singularities in anisotropic composites, " Int. J. Solids Structures , 17, 1 (1981) p. 1057.

27. Bogy, D.B., " The plane solution for anisotropic elastic wedge under normal and shear loading, " J. of App. Mech. , 39, 4 (1972) p. 1103.

28. Carpenter, W.C., " A collocation procedure for determining fracture mechanics parameters at a corners, " Int. J. of Fracture , 24 (1984) p. 255.

29. L.E., Hulbert, The Numerical Solution of Two-Dimensional Problems of the Theory of Elasticity, Ohio State University, Eng. Exper. Station, Bull. 198, Columbus Ohio.

30. Carpenter, W.C., " The eigenvector solution for general corner of finite opening crack with further studies on the collocation procedure, " Int. J. of Fracture , 27 (1985) p. 36.

31. Sinclair, B.G., Okajima, M. and Griffin, J.H., " Path independent integrals for computing stress intensity factors at sharp notches in elastic plate, " Int. J. of Num. Meth. in Engg. , 20 (1984) p. 999.

32. Wang, S.S. and Yuan, F.G., " A hybrid finite element approach to composite laminate elasticity problems with singularities, " J. of App. Mech. , 50, 4 (1983) p. 1.

33. Jones, R. and Callinan, R.J., " On the use of special crack tip elements in cracked elastic sheets, " Int. J. of Fracture , 13 (1977) p. 51.

34. The International Mathematics Subroutine Library, ZANLYT Subroutine, IMSL, INC. Houston, Texas.

35. Muller, D.E., " Method for solving algebraic equations using an automatic computer, " Math. Tables and Comput. , 10 (1956) p. 208.

36. The International Mathematics Subroutine Library, ZSCNT Subroutine, IMSL, INC. Houston, Texas.

37. G., Dahlquist and A., Bjorck, Numerical Methods, Prentice-Hall, Englewood Cliffs, New Jersey, 1974, pp. 196-201.

38. J.N., Reddy, An Introduction to the Finite Element Method, McGraw-Hill Book Co., N.Y., 1984.

39. Tong, P. and Pian, T.H.H., " The convergence of finite element method in solving linear elastic problems, " Int. J. Solids Structures , 3 (1967) p. 865.

40. W.D., Whetstone, EAL Engineering Analysis Language Reference Manual, Engineering Information Systems, Inc., San Jose, California, 1979.

41. V.V., Novozhilov, Foundations of the Nonlinear Theory of Elasticity, Graylock Press, Rochester, N.Y., 1953.

42. Pian, T.H.H., " Derivation of element stiffness matrices by assumed stress distributions, " AIAA J. , 2, 7 (1964) p. 1333.

43. Tasi, S.W. Composite Design 1986 , Thinks Composites, 1986, Dayton, Ohio.

44. Curry, J.M., Johnson, E.R., and Starnes, Jr., J.H., " Effect of ply drop-off on the strength of graphite-epoxy laminate," Virginia Tech Center for Composite Materials and Structures Report CCMS-86-07 and College of Engineering Report VPI-E-86-27, Blacksburg, Dec. 1986.

45. Whitney, J.M. and Nuismer, R.J., " Stress fracture criteria for laminated composite containing stress concentrations," J. of Composite Materials , 8, (1974), p. 253.

46. Kin, R.Y. and Soni, R., "Experimental and analytical studies on the onset of delamination in laminated composites," J. of Composite Materials , 18, (1984), p. 70.

Appendix A. Material Constitutive Relations

A.1 Transformation Relations

The geometric relations between the lamina principal 1-2-3 coordinates system and the laminate x-y-z system are depicted in Figure A.1. The principal lamina 1-2-3 material coordinates correspond to the transverse, normal, and longitudinal to the fiber directions respectively. The angle φ measures the angle between the 3 and z axis, a positive rotation corresponding to rotation of the fiber from the z axis to the x axis. The well known lamina constitutive relations in the 1-2-3 system are written as follows:

$$\begin{Bmatrix} \varepsilon_1 \\ \varepsilon_2 \\ \varepsilon_3 \\ \gamma_{23} \\ \gamma_{13} \\ \gamma_{12} \end{Bmatrix} = \begin{bmatrix} S_{11} & S_{12} & S_{13} & 0 & 0 & 0 \\ S_{21} & S_{22} & S_{23} & 0 & 0 & 0 \\ S_{31} & S_{32} & S_{33} & 0 & 0 & 0 \\ 0 & 0 & 0 & S_{44} & 0 & 0 \\ 0 & 0 & 0 & 0 & S_{55} & 0 \\ 0 & 0 & 0 & 0 & 0 & S_{66} \end{bmatrix} \begin{Bmatrix} \sigma_1 \\ \sigma_2 \\ \sigma_3 \\ \tau_{23} \\ \tau_{13} \\ \tau_{12} \end{Bmatrix}, \qquad [A.1]$$

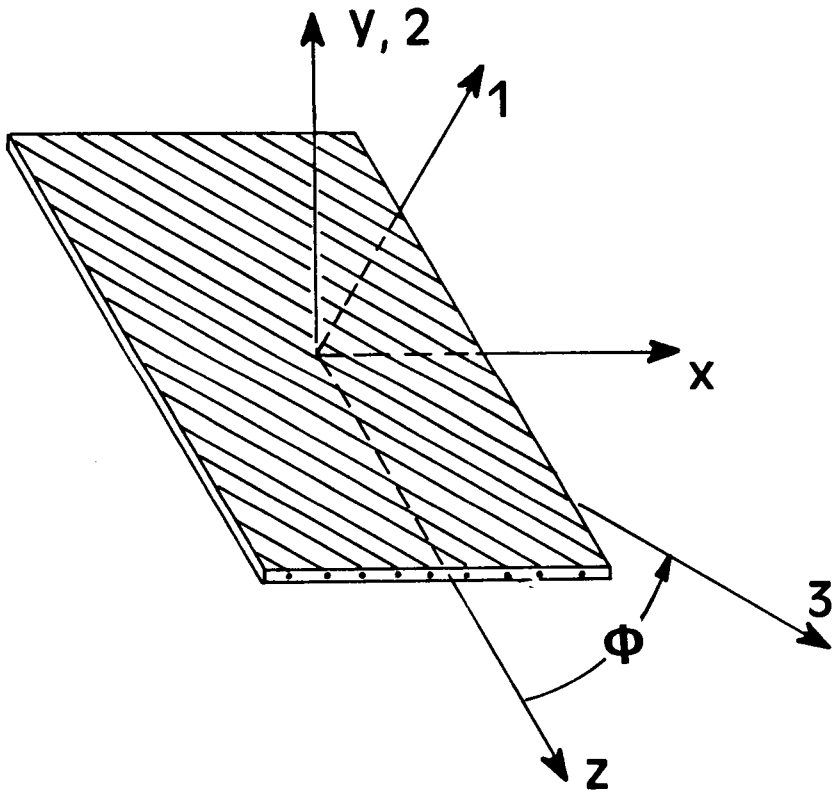

Figure A.1. Lamina and Laminate Material Coordinates Nomenclature.

where,

$$S_{ii} = \frac{1}{E_i} \quad , \quad i = 1,2,3 \quad ,$$

$$S_{ij} = \frac{\nu_{ij}}{E_j} \quad , \quad i, j = 1,2,3 \quad , \quad i \neq j \quad ,$$

$$S_{44} = \frac{1}{G_{23}} \quad , \quad S_{55} = \frac{1}{G_{13}} \quad , \quad S_{66} = \frac{1}{G_{12}} \quad ,$$

and, $S_{ij} = S_{ji}$. In inverted form the lamina constitutive relation in the 1-2-3 system takes the following form;

$$\begin{Bmatrix} \sigma_1 \\ \sigma_2 \\ \sigma_3 \\ \tau_{23} \\ \tau_{13} \\ \tau_{12} \end{Bmatrix} = \begin{bmatrix} C_{11} & C_{12} & C_{13} & 0 & 0 & 0 \\ C_{12} & C_{22} & C_{23} & 0 & 0 & 0 \\ C_{13} & C_{23} & C_{33} & 0 & 0 & 0 \\ 0 & 0 & 0 & C_{44} & 0 & 0 \\ 0 & 0 & 0 & 0 & C_{55} & 0 \\ 0 & 0 & 0 & 0 & 0 & C_{66} \end{bmatrix} \begin{Bmatrix} \varepsilon_1 \\ \varepsilon_2 \\ \varepsilon_3 \\ \gamma_{23} \\ \gamma_{13} \\ \gamma_{12} \end{Bmatrix} , \qquad [A.2]$$

where,

$$C_{11} = \frac{S_{22} S_{33} - S_{23}^2}{S} \quad , \quad C_{23} = \frac{S_{12} S_{13} - S_{23} S_{11}}{S} \quad ,$$

$$C_{22} = \frac{S_{11} S_{33} - S_{13}^2}{S} \quad , \quad C_{13} = \frac{S_{12} S_{23} - S_{13} S_{22}}{S} \quad ,$$

$$C_{33} = \frac{S_{11} S_{22} - S_{12}^2}{S} \quad , \quad C_{12} = \frac{S_{13} S_{23} - S_{12} S_{33}}{S} \quad ,$$

$$C_{ii} = \frac{1}{S_{ii}} \quad , \quad i = 4,5,6 \quad ,$$

and,

$$S = S_{11} S_{22} S_{33} - S_{11} s_{23}^2 - S_{22} S_{13}^2 - S_{33} S_{12}^2 + 2 S_{12} S_{13} S_{23} \quad .$$

The transformation of the stresses and the strains from the 1-2-3 coordinate system to the x-y-z system leads to;

$$\vec{\sigma}_1 = [T_1] \vec{\sigma}_x \quad , \qquad [A.3.a]$$

$$\vec{\varepsilon}_1 = [T_2] \vec{\varepsilon}_x \quad . \qquad [A.3.b]$$

The transformation matrices for the stresses, $[T_1]$ and $[T_2]$, are given by;

$$[T_1] = \begin{bmatrix} m^2 & 0 & n^2 & 0 & -2mn & 0 \\ 0 & 1 & 0 & 0 & 0 & 0 \\ n^2 & 0 & m^2 & 0 & 2mn & 0 \\ 0 & 0 & 0 & m & 0 & n \\ mn & 0 & -mn & 0 & (m^2 - n^2) & 0 \\ 0 & 0 & 0 & -n & 0 & m \end{bmatrix} \qquad [A.4.a]$$

and,

$$[T_2] = \begin{bmatrix} m^2 & 0 & n^2 & 0 & -mn & 0 \\ 0 & 1 & 0 & 0 & 0 & 0 \\ n^2 & 0 & m^2 & 0 & mn & 0 \\ 0 & 0 & 0 & m & 0 & n \\ 2mn & 0 & -2mn & 0 & (m^2 - n^2) & 0 \\ 0 & 0 & 0 & -n & 0 & m \end{bmatrix} \qquad [A.4.b]$$

Combining eqs. A.1 through eq. A.4, the lamina constitutive relations in the x-y-z coordinates system my be written as;

$$\vec{\varepsilon}_x = [\bar{S}]\,\vec{\sigma}_x \quad , \qquad [A.5.a]$$

$$\vec{\sigma}_x = [\bar{C}]\,\vec{\varepsilon}_x \quad . \qquad [A.5.b]$$

The coefficients in the compliance matrix, $[\bar{S}]$, are

$$\bar{S}_{11} = m^4 S_{11} + m^2 n^2 (2 S_{13} + S_{55}) + n^4 S_{33} \quad ,$$

$$\bar{S}_{12} = \bar{S}_{21} = m^2 S_{12} + n^2 S_{23} \quad ,$$

$$\bar{S}_{13} = \bar{S}_{31} = (m^4 + n^4) S_{13} + m^2 n^2 (S_{11} + S_{33} - S_{55}) \quad ,$$

$$\bar{S}_{15} = \bar{S}_{51} = m^3 n (2 S_{13} - 2 S_{11} + S_{55}) + m n^3 (2 S_{33} - 2 S_{13} - S_{55}) \quad ,$$

$$\bar{S}_{22} = S_{22} \quad ,$$

$$\bar{S}_{23} = \bar{S}_{32} = n^2 S_{12} + m^2 S_{23} \quad ,$$

$$\bar{S}_{25} = \bar{S}_{52} = 2 m n (S_{23} - S_{12}) \quad ,$$

$$\bar{S}_{33} = n^4 S_{11} + m^2 n^2 (2 S_{13} + S_{55}) + m^4 S_{33} \quad ,$$

$$\bar{S}_{35} = \bar{S}_{53} = m^3 n (2 S_{33} - 2 S_{13} - S_{55}) + m n^3 (2 S_{13} - 2 S_{11} + S_{55}) \quad ,$$

$$\bar{S}_{44} = m^2 S_{44} + n^2 S_{66} \quad ,$$

$$\bar{S}_{46} = \bar{S}_{64} = m n (S_{44} - S_{66}) \quad ,$$

$$\bar{S}_{55} = 2 m^2 n^2 (2 S_{33} - 2 S_{11} - 4 S_{13} - S_{55}) + (m^4 + n^4) S_5 \quad ,$$

$$\bar{S}_{66} = n^2 S_{44} + m^2 S_{55} \quad ,$$

and all other coefficients are zero. The coefficients in the lamina stiffness matrix, $[\bar{C}]$ are given as;

$$\bar{C}_{11} = m^4 C_{11} + m^2 n^2 (C_{13} + 2 C_{55}) + n^4 C_{33} \quad ,$$

$$\bar{C}_{12} = \bar{C}_{21} = m^2 C_{12} + n^2 C_{23} \quad ,$$

$$\bar{C}_{13} = \bar{C}_{31} = (m^4 + n^4) C_{13} + m^2 n^2 (C_{11} + C_{33} - 4 C_{55}) \quad ,$$

$$\bar{C}_{15} = \bar{C}_{51} = m^3 n (C_{13} - C_{11}) + m n^3 (C_{33} - C_{13}) \quad ,$$

$$\bar{C}_{22} = C_{22} \quad ,$$

$$\bar{C}_{23} = \bar{C}_{32} = n^2 C_{12} + m^2 C_{23} \quad ,$$

$$\bar{C}_{25} = \bar{C}_{52} = m n (C_{23} - C_{12}) \quad ,$$

$$\bar{C}_{33} = n^4 C_{11} + 2 m^2 n^2 (C_{13} + 2 C_{55}) + m^4 C_{33} \quad ,$$

$$\bar{C}_{35} = \bar{C}_{53} = m\,n^3\,(C_{13} - C_{11}) + m^3\,n\,(C_{33} - C_{13}) - 2\,m\,n\,(m^2 - n^2)\,C_{55} \quad ,$$

$$\bar{C}_{44} = m^2\,C_{44} + n^2\,C_{66} \quad ,$$

$$\bar{C}_{46} = \bar{C}_{64} = m\,n\,(C_{44} - C_{66}) \quad ,$$

$$\bar{C}_{55} = 2\,m^2\,n^2\,(C_{33} + C_{11} - 2\,C_{13} - 2\,C_{55}) + (m^4 + n^4)\,C_{55} \quad ,$$

$$\bar{C}_{66} = n^2\,C_{44} + m^2\,C_{66} \quad ,$$

and all other coefficients are zero.

A.2 Integrated Material Properties

The integrated laminate properties are obtained by smearing the individual lamina properties throughout the thickness of the laminate. This is achieved by defining an average stress through the laminate thickness, h, i.e.,

$$\vec{\bar{\sigma}}_x = \frac{1}{h} \int_{-1/h}^{1/h} \vec{\sigma}_x \, dy \quad . \qquad [A.6]$$

Substitution of eq. A.5.a into eq. A.6 leads to the laminate constitutive relations:

$$\begin{Bmatrix} \sigma_x \\ \sigma_y \\ \sigma_z \\ \tau_{yz} \\ \tau_{xz} \\ \tau_{xy} \end{Bmatrix} = \begin{bmatrix} A_{11} & A_{12} & A_{13} & 0 & 0 & 0 \\ A_{21} & A_{22} & A_{23} & 0 & 0 & 0 \\ A_{31} & A_{32} & A_{33} & 0 & 0 & 0 \\ 0 & 0 & 0 & A_{44} & 0 & 0 \\ 0 & 0 & 0 & 0 & A_{55} & 0 \\ 0 & 0 & 0 & 0 & 0 & A_{66} \end{bmatrix} \begin{Bmatrix} \varepsilon_x \\ \varepsilon_y \\ \varepsilon_z \\ \gamma_{yz} \\ \gamma_{xz} \\ \gamma_{xy} \end{Bmatrix} , \qquad [A.7.a]$$

where the overbar is dropped from the stresses for convenience. The laminate stiffness components A_{ij} are given by,

$$A_{ij} = \frac{1}{h} \sum_{k=1}^{n} \bar{C}_{ij} \, (y_k - y_{k-1}) \quad , \qquad [A.7.b]$$

n being the number of laminae and y_k and y_{k-1} are defined in the same manner as in classical laminate theory (CLT). In inverted form,

$$\begin{Bmatrix} \varepsilon_x \\ \varepsilon_y \\ \varepsilon_z \\ \gamma_{yz} \\ \gamma_{xz} \\ \gamma_{xy} \end{Bmatrix} = \begin{bmatrix} a_{11} & a_{12} & a_{13} & 0 & 0 & 0 \\ a_{12} & a_{22} & a_{23} & 0 & 0 & 0 \\ a_{13} & a_{23} & a_{33} & 0 & 0 & 0 \\ 0 & 0 & 0 & a_{44} & 0 & 0 \\ 0 & 0 & 0 & 0 & a_{55} & 0 \\ 0 & 0 & 0 & 0 & 0 & a_{66} \end{bmatrix} \begin{Bmatrix} \sigma_x \\ \sigma_y \\ \sigma_z \\ \tau_{yz} \\ \tau_{xz} \\ \tau_{xy} \end{Bmatrix} . \qquad [A.8]$$

It should be noted that although each individual lamina is considered to be anisotropic, the laminate constitutive law is that of orthotropic material. The coefficients of the laminate compliance matrix , a_{ij}, are given by;

$$a_{11} = \frac{A_{22} A_{33} - A_{23}^2}{A} \quad , \quad a_{23} = \frac{A_{12} A_{13} - A_{23} A_{11}}{A} \quad ,$$

$$a_{22} = \frac{A_{11} A_{33} - A_{13}^2}{A} \quad , \quad a_{13} = \frac{A_{12} A_{23} - A_{13} A_{22}}{A} \quad ,$$

$$a_{33} = \frac{A_{11} A_{22} - A_{12}^2}{A} \quad , \quad a_{12} = \frac{A_{13} A_{23} - A_{12} A_{33}}{A} \quad ,$$

$$a_{ii} = \frac{1}{A_{ii}} \quad , \quad i = 4,5,6 \quad ,$$

were,

$$A = A_{11} A_{22} A_{33} - A_{11} A_{23}^2 - A_{22} A_{13}^2 - A_{33} A_{12}^2 + 2 A_{12} A_{13} A_{23} \quad .$$

Appendix B. The Eigenvalue Problem

The eigenvalue problem for λ and δ is developed in this appendix for a general bimaterial composite wedge depicted by Figure B.1. The traction-free wedge boundaries are located by the angles α_1 and α_2 in material 1 and 2, respectively.

B.1 The δ Eigenvalue Problem

The set of equations which form the eigenvalue problem for δ is written symbolically as,

$$[\, Q(\alpha_1, \alpha_2; \delta)\,]\,\vec{D} \;=\; 0 \quad , \qquad [B.1]$$

where the coefficients q_{ij} are given by,

$$q_{11} = (\cos\alpha_1 + i\,\upsilon^{(1)} \sin\alpha_1)^{\delta+1} \quad , \quad q_{12} = (\cos\alpha_1 - i\,\upsilon^{(1)} \sin\alpha_1)^{\delta+1} \quad ,$$

$$q_{13} = q_{14} = q_{21} = q_{22} = 0 \quad ,$$

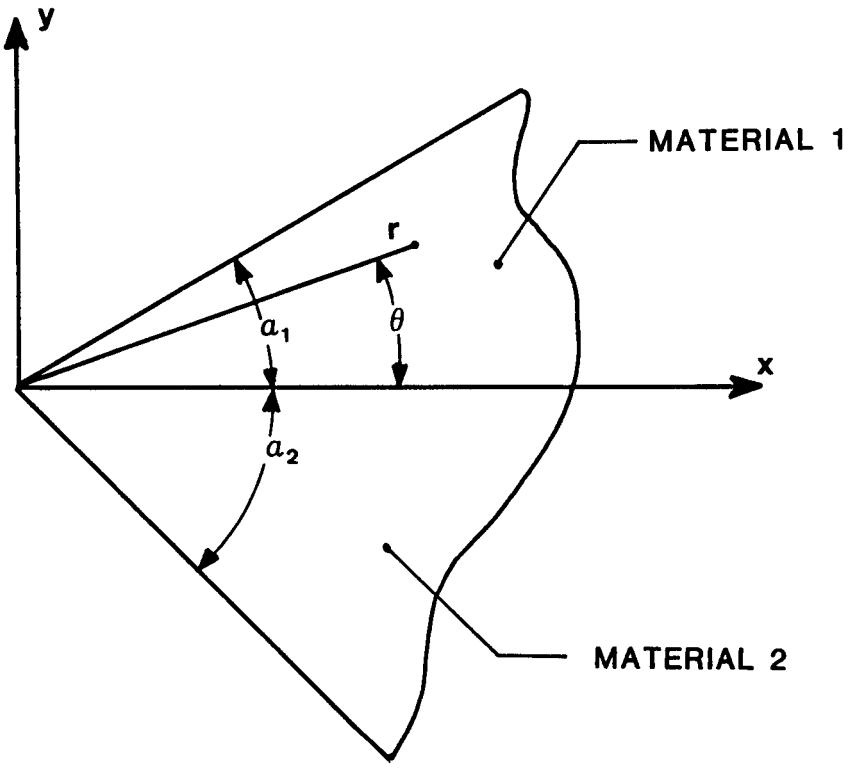

Figure B.1. General Bimaterial Composite Wedge Geometry.

$$q_{23} = (\cos\alpha_2 - i\upsilon^{(2)}\sin\alpha_2)^{\delta+1} \ , \ q_{24} = (\cos\alpha_2 + i\upsilon^{(2)}\sin\alpha_2)^{\delta+1} \ ,$$

$$q_{31} = q_{32} = 1 \ , \ q_{33} = q_{34} = -1 \ ,$$

$$q_{41} = -q_{42} = \eta^{(1)} \ , \ q_{43} = -q_{44} = \eta^{(2)} \ .$$

with,

$$\upsilon^{(k)} = \sqrt{\frac{\beta_{44}^{(k)}}{\beta_{55}^{(k)}}} \quad , \quad k = 1,2 \ ,$$

and,

$$\eta^{(k)} = i\sqrt{\beta_{44}^{(k)}\,\beta_{55}^{(k)}} \quad , \quad k = 1,2 \ .$$

The eigenvector , $\vec{D}$, is given by,

$$\vec{D} = \begin{Bmatrix} \vec{D}^{(1)} \\ \vec{D}^{(2)} \end{Bmatrix} \ , \qquad [B.2]$$

where the two eigenvectors, $\vec{D}^{(1)}$ and $\vec{D}^{(2)}$ are related to material 1 and 2, respectively. Due to the boundary conditions, the two vectors are related by an equation of the form

$$\begin{bmatrix} 1 & 1 \\ \eta^{(1)} & -\eta^{(1)} \end{bmatrix} \vec{D}^{(1)} = \begin{bmatrix} 1 & 1 \\ \eta^{(2)} & -\eta^{(2)} \end{bmatrix} \vec{D}^{(2)} \ , \qquad [B.3.a]$$

leading to,

$$\vec{D}^{(2)} = \frac{1}{2\eta^{(2)}} \begin{bmatrix} (\eta^{(2)} + \eta^{(1)}) & (\eta^{(2)} - \eta^{(1)}) \\ (\eta^{(2)} - \eta^{(1)}) & (\eta^{(2)} + \eta^{(1)}) \end{bmatrix} \vec{D}^{(1)} \ . \qquad [B.3.b]$$

The reduced eigenvalue problem takes the form,

$$[\, J(\alpha_1, \alpha_2; \delta)\,]\,\vec{D}^{(1)} = 0 \quad , \qquad [B.4]$$

where,

$$j_{11} = (\cos\alpha_1 + i\,\upsilon^{(1)} \sin\alpha_1)^{\delta+1} \quad , \quad j_{12} = (\cos\alpha_1 - i\,\upsilon^{(1)} \sin\alpha_1)^{\delta+1} \quad ,$$

$$j_{21} = \frac{1}{2\,\eta^{(2)}}\,[\,(\eta^{(2)} + \eta^{(1)})(\cos\alpha_2 - i\,\upsilon^{(2)} \sin\alpha_2)^{\delta+1} + (\eta^{(2)} - \eta^{(1)})(\cos\alpha_2 + i\,\upsilon^{(2)} \sin\alpha_2)^{\delta+1}\,] \quad ,$$

$$j_{22} = \frac{1}{2\,\eta^{(2)}}\,[\,(\eta^{(2)} - \eta^{(1)})(\cos\alpha_2 - i\,\upsilon^{(2)} \sin\alpha_2)^{\delta+1} + (\eta^{(2)} + \eta^{(1)})(\cos\alpha_2 + i\,\upsilon^{(2)} \sin\alpha_2)^{\delta+1}\,] \quad ,$$

B.2 The λ Eigenvalue Problem

The eigenvalue problem associated with λ is written symbolically as,

$$[\, A(\alpha_1, \alpha_2; \lambda)\,]\,\vec{C} = 0 \quad , \qquad [B.5]$$

where,

$$a_{1k} = (\cos\alpha_1 + \mu_k^{(1)} \sin\alpha_1)^{(\lambda+2)} \quad , \quad a_{1(k+4)} = 0 \quad ,$$

$$a_{2k} = (\mu_k^{(1)} \cos\alpha_1 - \sin\alpha_1)(\cos\alpha_1 + \mu_k^{(1)} \sin\alpha_1)^{(\lambda+1)} \quad , \quad a_{2(k+4)} = 0 \quad ,$$

$$a_{3k} = 0 \quad , \quad a_{3(k+4)} = (\cos\alpha_2 - \mu_k^{(2)} \sin\alpha_2)^{(\lambda+2)} \quad ,$$

$$a_{4k} = 0 \quad , \quad a_{4(k+)} = (\mu_k^{(2)} \cos\alpha_2 + \sin\alpha_2)(\cos\alpha_2 - \mu_k^{(2)} \sin\alpha_2)^{(\lambda+1)} \quad ,$$

$$a_{5k} = 1 \quad , \quad a_{5(k+4)} = -1 \quad ,$$

$$a_{6k} = \mu_k^{(1)} \quad , \quad a_{6(k+4)} = -\mu_k^{(2)} \quad ,$$

$$a_{7k} = p_k^{(1)} \quad , \quad a_{7(k+4)} = -p_k^{(2)} \quad ,$$

$$a_{8k} = q_k^{(1)} \quad , \quad a_{8(k+4)} = -q_k^{(2)} \quad ,$$

where k = 1,2,3,4, and p_k and q_k are defined by

$$p_k = \beta_{11}\,\mu_k^2 + \beta_{12} \quad ,$$

$$q_k = \beta_{12}\mu_k + \frac{\beta_{22}}{\mu_k} \quad .$$

In addition, μ_k has one of four unique value given by the characteristic equation

$$\beta_{22} + (2\beta_{12} + \beta_{66})\mu_k^2 + \beta_{11}\mu_k^4 = 0 \quad .$$

Such roots do exist and they are always complex or imaginary.

The eigenvector $\vec{C}$ is define by,

$$\vec{C} = \begin{Bmatrix} \vec{C}^{(1)} \\ \vec{C}^{(2)} \end{Bmatrix} \quad , \qquad [B.6]$$

where, the $\vec{C}^{(1)}$ and $\vec{C}^{(2)}$ are two vectors associated with material 1 and 2, respectively. Due to the boundary conditions, the two vectors are related by an equation of the form

$$[E^{(1)}]\vec{C}^{(1)} = [E^{(2)}]\vec{C}^{(2)} \quad , \qquad [B.7]$$

where,

$$e_{1k}^{(i)} = 1 \ , \ e_{2k}^{(i)} = \mu_k^{(i)} \ , \ e_{3k}^{(i)} = p_k^{(i)} \ , \ e_{4k}^{(i)} = q_k^{(i)} \ , i = 1,2 \ , k = 1,2,3,4 \quad .$$

The relation between the two vectors is then given by,

$$\vec{C^{(2)}} = [T]\vec{C^{(1)}} \quad , \qquad [B.8]$$

where,

$$[T] = [E^{(2)}]^{-1}[E^{(1)}] \quad ,$$

is the vector transformation matrix. This leads to the reduced eigenvalue problem associated with $\vec{C}^{(1)}$ only. The problem may be written as

$$[\, H(\alpha_1, \alpha_2; \lambda)\,]\,\vec{C}^{(1)} = 0 \quad , \qquad [B.9]$$

where,

$$h_{ij} = a_{ij} \quad , i = 1,2 \; , j = 1,2,3,4 \quad ,$$

$$h_{ij} = \sum_{k=1}^{4} a_{i(k+4)}\, t_{kj} \quad , i = 3,4 \; , j = 1,2,3,4 \quad ,$$

where t_{kj} are the elements of the transformation matrix [T].

B.3 Eigenvector Representation

The eigenvectors $\vec{D}_n$ and $\vec{C}_n$ associated with the n^{th} eigenvalue, given by eqs. B.2 and B.6, respectively, are of arbitrary magnitude. To eliminate some of the arbitrariness the vectors are normalized according to the following procedure. Letting $D_{n1}^{(1)} = D_n(\frac{1}{\sqrt{2}}, \frac{1}{\sqrt{2}})$ leads to,

$$\vec{D}_n^{(1)} = D_n \begin{Bmatrix} d_{n1}^{(1)} \\ d_{n2}^{(1)} \end{Bmatrix} \quad , \qquad [B.10]$$

where,

$$d_{n1}^{(1)} = \frac{1}{\sqrt{2}} + i\frac{1}{\sqrt{2}} \quad ,$$

$$d_{n2}^{(1)} = \frac{D_{n2}^{(1)}}{D_n} \quad ,$$

and D_n is an arbitrary constant, $D_n = d_n + i\,d'_n$. If δ is real, then the normalization of the vector $\vec{D}_n^{(1)}$ is achieved by letting $d_{n1}^{(1)} = 1.0$ and $D_n = d_n$. The eigenvector associated with material 2, $\vec{D}_n^{(2)}$, is obtained from the vector transformation eq. B.3.b.

In a similar manner letting,

$$C_{n1}^{(1)} = C_n \left(\frac{1}{\sqrt{2}}, \frac{1}{\sqrt{2}}\right) ,$$

leads to,

$$\vec{C}_n^{(1)} = C_n \begin{Bmatrix} c_{n1}^{(1)} \\ c_{n2}^{(1)} \\ c_{n3}^{(1)} \\ c_{n4}^{(1)} \end{Bmatrix} , \qquad [B.11]$$

where,

$$c_{n1}^{(1)} = \frac{1}{\sqrt{2}} + i\frac{1}{\sqrt{2}}$$

$$c_{nl}^{(1)} = \frac{C_{nl}^{(1)}}{C_n} , \qquad l = 2,3,4 ,$$

and C_n is an arbitrary complex constant, $C_n = c_n + i\,c'_n$. As before, if λ is real, then $c_{n1}^{(1)} = 1.0$ and $C_n = c_n$ is a real constant. The eigenvector $\vec{C}_n^{(2)}$ associated with material 2 is obtained via the vector transformation eq. B.8.

The unknown coefficients $d_{n2}^{(1)}$ and $c_{nl}^{(1)}$, $l = 2,3,4$ are obtained by eqs. B.4 and B.9, respectively, by eliminating the first row and first column from matrix [J] and [H], respectively. Thus, for both δ and λ there is one complex undetermined coefficient associated with each eigenvalue.

B.4 Eigenfunction Expansion Representation

The eigenfunction expansion representation of $F^{(\bullet)}(x,y)$ and $\Psi^{(\bullet)}(x,y)$ will differ depending on whether the δ and λ are real or complex. As noted before, if δ and λ are complex they will occur in complex conjugate pairs. In the following section the proper functional form for a real and complex eigenvalue is discussed. Only detailed development for $F^{(\bullet)}(x,y)$ is shown since the form for $\Psi^{(\bullet)}(x,y)$ is identical.

Real Eigenvalue

For a real eigenvalue ,

$$\lambda = \gamma \text{ (real)} \quad .$$

The stresses associated with $F^{(\bullet)}(x,y)$ can be written as,

$$\sigma_i = \sum_{k=1}^{2} (A_k G_{ik} + A_{k+2} \overline{G}_{ik}) \quad , \qquad i = x,y,xy \quad , \qquad [B.12]$$

where,

$$A_k = a_k + i\, a'_k$$

$$G_{ik} = g_{ik} + i\, g'_{ik}$$

and $\overline{G}_{ik}$ is the conjugate of G_{ik}. In addition g_{ik} and g'_{ik} are unique functions of r and θ., as shown next. Considering σ_y for example,

$$\sigma_y = \sum_{k=}^{4} A_k Z_k^{\lambda} \quad . \qquad [B.13]$$

By making the following substitutions;

$$x = r \cos\theta \ , \quad y = r \sin\theta \ , \qquad [B.14.a]$$

$$Z = x + \mu y = r\rho e^{i\psi} \ , \qquad [B.14.b]$$

where,

$$\mu = \alpha \pm i\beta \ ,$$

$$\rho^2 = (\cos\theta + \alpha \sin\theta)^2 + \beta^2 \sin^2\theta \ , \qquad [B.14.c]$$

$$\tan\psi = \frac{\beta \sin\theta}{\cos\theta + \alpha \sin\theta} \ , \qquad [B.14.d]$$

σ_y becomes

$$\sigma_y = A_1 G_{y1} + A_2 G_{y2} + A_3 \overline{G}_{y1} + A_4 \overline{G}_{y2} \ . \qquad [B.15]$$

In the above

$$G_{y1} = (r\rho_1)^\gamma [\cos(\gamma\psi_1) + i \sin(\gamma\psi_1)] \ , \qquad [B.16.a]$$

$$G_{y2} = (r\rho_2)^\gamma [\cos(\gamma\psi_2) + i \sin(\gamma\psi_2)] \ . \qquad [B.16.b]$$

As noted earlier, μ always occurs in a complex conjugates pairs, that is,

$$\mu_1 = \alpha_1 + i\beta_1 \ , \quad \mu_2 = \alpha_2 + i\beta_2 \ , \qquad [B.17.a]$$

$$\mu_3 = \alpha_1 - i\beta_1 \ , \quad \mu_4 = \alpha_2 - i\beta_2 \ . \qquad [B.17.b]$$

Similar results can be obtained for the other stress components. Expansion of eq. B.12 leads to,

$$\sigma_i = \sum_{k=1}^{2} [(a_k + a_{k+2}) g_{ik} + (a'_{k+2} - a'_k) g'_{ik}] \qquad [B.18]$$

$$+ \; i\,[\,(a'_k \; + \; a'_{k+2})\, g_{ik} \; + \; (a_k \; - \; a_{k+2})\, g'_{ik}\,] \; .$$

However, since σ_i must be a real quantity and g_{ik} and g'_{ik} are unique functions of r and θ, setting the imaginary part of σ_i to zero leads to,

$$a'_{k+2} \; = \; - \; a'_k \; , \qquad a_{k+2} \; = \; a_k \; ,$$

that is $A_{k+2} \; = \; \overline{A}_k$. Next the coefficients are redefined,

$$c_k \; = \; a_k \; + \; a_{k+2} \; = \; 2\, a_k$$

$$c_{k+2} \; = \; a'_{k+2} \; - \; a'_k \; = \; - \; 2\, a'_k \; .$$

It follows that the stresses can be written as,

$$\sigma_i \; = \; \sum_{k=1}^{2} \; [\; c_k \, \mathrm{Re}\,(G_{ik}) \; + \; c_{k+2} \, \mathrm{Im}\,(G_{ik})\;] \; , \quad i \; = \; x,y,xy \; , \qquad [B.19]$$

with c_k, (k = 1,2,3,4) being real constants.

Complex Eigenvalue

As was previously stated, if λ is complex it will occur in complex conjugate pairs, i.e.,

$$\lambda \; = \; \gamma \; + \; i\,\varphi \; , \quad \overline{\lambda} \; = \; \gamma \; - \; i\,\varphi \; .$$

The stresses associated with $F^{(e)}\,(x,y)$, for a pair of complex conjugate eigenvalue, will take the following form;

$$\sigma_i \; = \; \sum_{k=1}^{4} \; A_k \, G_{ik} \; + \; \sum_{k=1}^{4} \; B_k \, \overline{G}_{ik} \; , \qquad i \; = \; x,y,xy \; , \qquad [B.20]$$

with A_k and B_k being arbitrary complex constants, $A_k = a_k + i\,a'_k$ and $B_k = b_k + i\,b'_k$. The function $\overline{G}_{ik}$ associated with $\overline{\lambda}$ is the conjugate of the function $G_{ik} \; = \; g_{ik} \; + \; i\,g'_{ik}$ associated

with λ . In addition, g_{ik} and g'_{ik} are unique functions of r and θ, as shown next. Considering σ_y again for λ and $\bar{\lambda}$ in the most general form becomes,

$$\sigma_y = \sum_{k=1}^{4} A_k Z_k^{\lambda} + \sum_{k=1}^{4} B_k Z_k^{\bar{\lambda}} \quad , \qquad [B.21]$$

where for complex eigenvalues, using relations B.14.a and B.14.b,

$$Z_k^{\lambda} = (r\rho_k)^{\gamma} e^{-\psi_k \varphi} [\cos \eta_k + i \sin \eta_k] \quad , \qquad [B.22.a]$$

$$Z_k^{\bar{\lambda}} = (r\rho_k)^{\gamma} e^{\psi_k \varphi} [\cos \eta'_k + i \sin \eta'_k] \quad , \qquad [B.22.b]$$

where,

$$\eta_k = \gamma \psi_k + \varphi \ln(r\rho_k) \quad ,$$

$$\eta'_k = \gamma \psi_k - \varphi \ln(r\rho_k) \quad .$$

Considering eqs. B.14 and B.17 and substituting eq. B.22 into eq. B.21, σ_y may be written as,

$$\sigma_y = A_1 f_1 + A_2 f_2 + A_3 f_3 + A_4 f_4 + A_5 f_5 + A_6 f_6 + A_7 f_7 + A_8 f_8 \quad , \quad [B.23]$$

where, f_i , $i = 1,2,...,8$ are complex functions. Next, it can be shown that f_7 is the conjugate of f_1 (i.e., $f_7 = \bar{f}_1$) where,

$$f_1 = (r\rho_1)^{\gamma} e^{\psi_1 \varphi} \{\cos [\gamma \psi_1 + \varphi \ln(r\rho_1)] + i \sin [\gamma \psi_1 + \varphi \ln(r\rho_1)]\} \quad .$$

Similarly, $f_8 = \bar{f}_2$, $f_5 = \bar{f}_3$, and $f_6 = \bar{f}_4$. Since the numbering of the functions and coefficients is arbitrary, eq. B.23 can be written in the form of eq. B.20, where,

$$G_{y1} = f_1 \ , \quad G_{y2} = f_2 \ , \quad G_{y3} = f_3 \ , \quad G_{y4} = f_4$$

$$\bar{G}_{y1} = \bar{f}_1 \ , \quad \bar{G}_{y2} = \bar{f}_2 \ , \quad \bar{G}_{y3} = \bar{f}_3 \ , \quad \bar{G}_{y4} = \bar{f}_4 \quad .$$

Similar results can be obtained for the other stress components. Expansion of eq. B.20 leads to the following result;

$$\sigma_i = \sum_{k=1}^{4} [(a_k + b_k) g_{ik} + (b'_k - a'_k) g'_{ik}]$$

$$+ i[(a'_k + b'_k) g_{ik} + (a_k - b_k) g'_{ik}] . \qquad [B.24]$$

However, since σ_i must be a real quantity and g_{ik} and g'_{ik} are unique functions of r and θ. Setting the imaginary part of σ_i to zero leads to,

$$b'_k = - a'_k , \quad b_k = a_k ,$$

i.e., $B_k = \overline{A}_k$. Renaming the constants as,

$$c_k = a_k + b_k = 2 b_k ,$$

$$c'_k = b'_k - a'_k = 2 b'_k ,$$

leads to the following eigenfunction expansion of stress,

$$\sigma_i = \sum_{k=1}^{4} c_k \, Re(G_{ik}) + \sum_{k=1}^{4} c'_k \, Im(G_{ik}) , \quad , \quad i = x,y,xy , \qquad [B.25]$$

where c_k and c'_k are two unknown real constants. It should be noted that the above representation of stresses leads to the classical stress formulation arising from a complex stress function. For example,

$$\sigma_x = 2 Re\left[\sum_{k=1}^{4} C_k \frac{\partial^2 F}{\partial y^2} \right] , \quad \text{etc...}$$

with C_k being an arbitrary complex constant.

Based on the above discussion and the one given in the previous section, the general form of the stress functions $F^{(\bullet)}(x,y)$ and $\Psi^{(\bullet)}(x,y)$ can be written.

Real Eigenvalue

For real n^{th} eigenvalue, the two stress functions $F^{(\bullet)}(x,y)$ and $\Psi^{(\bullet)}(x,y)$ are given by,

$$F^{(\bullet)}(x,y) = \sum_{n=1}^{\infty} \frac{c_n}{(\lambda_n + 1)(\lambda_n + 2)} \{ \mathrm{Re}\left[\sum_{k=1}^{2} c_{nk} Z_k^{(\lambda_n + 2)} \right] + \mathrm{Im}\left[c_{n(k+2)} Z_k^{(\lambda_n + 2)} \right] \} , \qquad [B.26]$$

$$\Psi^{(\bullet)}(x,y) = \sum_{n=1}^{\infty} \frac{d_n}{(\delta_n + 1)} \{ \mathrm{Re}\left[d_{n1} \bar{Z}_1^{(\delta_n + 1)} \right] + \mathrm{Im}\left[d_{n2} \bar{Z}_k^{(\delta_n + 1)} \right] \} , \qquad [B.27]$$

with c_n and d_n being arbitrary real constants and c_{nk}, $(k = 1,2,3,4)$ and d_{nk}, $(k = 1,2)$ known quantities of the normalized n^{th} eigenvector (see section B.2).

Complex Eigenvalues

If the n^{th} eigenvalue is complex, the two stress functions are given by,

$$F^{(\bullet)}(x,y) = \sum_{n=1}^{\infty} \{ c_n \, \mathrm{Re}\left[\sum_{k=1}^{4} c_{nk} \frac{Z_k^{(\lambda_n + 2)}}{(\lambda_n + 1)(\lambda_n + 2)} \right] + c'_n \, \mathrm{Im}\left[\sum_{k=1}^{4} c_{nk} \frac{Z_k^{(\lambda_n + 2)}}{(\lambda_n + 1)(\lambda_n + 2)} \right] \} , \qquad [B.28]$$

$$\Psi^{(\bullet)}(x,y) = \sum_{n=1}^{\infty} \{ d_n \, \mathrm{Re}\left[\sum_{k=1}^{2} d_{nk} \frac{\bar{Z}_k^{(\delta_n + 2)}}{(\delta_n + 1)} \right]$$

$$+ \; d'_n \, \mathrm{Im} \left[\sum_{k=1}^{2} d_{nk} \frac{\bar{Z}_k^{(\delta_n + 1)}}{(\delta_n + 1)} \right] \Big\} \quad , \qquad [B.29]$$

with c_n, c'_n, d_n and d'_n being arbitrary real constants and c_{nk}, (k = 1,2,3,4) and d_{nk}, (k = 1,2) being known quantities of the normalized n^{th} eigenvectors. With the functional form for $F^{(\bullet)}(x,y)$ and $\Psi^{(\bullet)}(x,y)$ known, the eigenfunction expansion for both stresses and displacements can be determined.

Appendix C. Finite-Element Formulation

C.1 PE2D Finite-Element Formulation

In this appendix the PE2D finite-element program is described in greater detail. This program is based on the elasticity equations which govern an elastic body for which the stresses do not vary along it's generator (the z axis). Such a condition is referred to as the a generalized plane deformation.

The finite-element program is based on the displacement formulation approach and it is derived from the total potential energy function, Π_p,

$$\Pi_p = \frac{1}{2} \int_V \vec{\varepsilon}_x^T \vec{\sigma}_x \, dV - \int_A \mathbf{u}^T \mathbf{t} \, dA \quad , \qquad [C.1]$$

The first term corresponds to the body's total strain energy, the second to the work done by the external force, t. The work done by the body forces is neglected. The generalized plane deformation finite-element model is based on the displacement field for homogeneous

anisotropic body for which the stress do not vary with z for this situation. The displacement functions u, v, and w have the following form:

$$u = -\frac{B_1 a_{33}}{2} z^2 - B_4 y z + U(x,y) + \omega_2 z - \omega_3 y + u_o \ , \qquad [C.2.a]$$

$$v = -\frac{B_2 a_{33}}{2} z^2 + B_4 x z + V(x,y) + \omega_3 x - \omega_1 z + v_o \ , \qquad [C.2.b]$$

$$w = (B_1 x + B_2 y + B_3)\, a_{33} z + W(x,y) + \omega_1 y - \omega_2 x + w_o \ , \qquad [C.2.c]$$

where B_i, $i = 1,2,3,4$, are arbitrary constants of integration, ω_i, $i = 1,2,3$ are rigid body rotations, and u_o, v_o and w_o are rigid body translations. In addition, U(x,y), V(x,y) and W(x,y) are unknown displacement functions which depend on x and y only. This displacement field can be written in vectorial form as,

$$\mathbf{u} = \mathbf{u_o} + \mathbf{U} \ , \qquad [C.3]$$

where,

$$\mathbf{u_o^T} = \{u_o(x,y,z) \ ; \ v_o(x,y,z) \ ; \ w_o(x,y,z)\} \ ; \ ,$$

$$\mathbf{U^T} = \{U(x,y) \ ; \ V(x,y) \ ; \ W(x,y)\} \ ,$$

and,

$$u_o(x,y,z) = -\frac{B_1 a_{33}}{2} z^2 - B_4 y z \ ,$$

$$v_o(x,y,z) = -\frac{B_2 a_{33}}{2} z^2 + B_4 x z \ ,$$

$$w_o(x,y,z) = (B_1 x + B_2 y + B_3) a_{33} z \quad .$$

The terms associated with the rigid body rotation and translation are omitted. It may be shown that the unknown constants B_i, $i = 1,2,3,4$, are related to the body's kinematic end conditions, i.e.,

$$B_3 = \frac{e_o}{a_{33}} \quad , \quad B_2 = \frac{\kappa_z}{a_{33}} \quad , \quad B_4 = -\frac{\kappa_{xz}}{2} \quad .$$

In the stiffened-skin structural context, e_o and κ_z are the axial extension and curvature in the z direction, and κ_{xz} is the twist curvature about the z axis. The coefficient B_1 relates to the in-plane twist about the y-axis and is of no consequence in the structure considered here and is therefore set to zero. The strain vector, $\vec{\varepsilon}_x$ is given by,

$$\vec{\varepsilon}_x = \vec{E} + \vec{\varepsilon}_o \quad , \qquad [C.4.a]$$

where,

$$\vec{\varepsilon}_x^T = \{\varepsilon_x \; ; \; \varepsilon_y \; ; \; \varepsilon_z \; ; \; \gamma_{yz} \; ; \; \gamma_{xz} \; ; \; \gamma_{xy}\} \quad , \qquad [C.4.b]$$

$$\vec{E}^T = \{\frac{\partial U}{\partial x} \; ; \; \frac{\partial V}{\partial y} \; ; \; 0 \; ; \; \frac{\partial W}{\partial y} \; ; \; \frac{\partial W}{\partial x} \; ; \; \frac{\partial U}{\partial y} + \frac{\partial V}{\partial x}\} \quad , \qquad [C.4.c]$$

and,

$$\vec{\varepsilon}_o^T = \{0 \; ; \; 0 \; ; \; (e_o + \kappa_z y) \; ; \; -\frac{\kappa_{xz}}{2} x \; ; \; \frac{\kappa_{xz}}{2} y \; ; \; 0\} \quad . \qquad [C.4.d]$$

Next, the laminate constitutive law may be written in a reduced form as,

$$\vec{\bar{\varepsilon}}_x = \begin{Bmatrix} \frac{\partial U}{\partial x} - \varepsilon_x^o \\ \frac{\partial V}{\partial y} - \varepsilon_y^o \\ \frac{\partial W}{\partial y} - \gamma_{yz}^o \\ \frac{\partial W}{\partial x} - \gamma_{xz}^o \\ \frac{\partial U}{\partial y} + \frac{\partial V}{\partial x} \end{Bmatrix} = \begin{bmatrix} \beta_{11} & \beta_{12} & 0 & 0 & 0 \\ \beta_{12} & \beta_{22} & 0 & 0 & 0 \\ 0 & 0 & \beta_{44} & 0 & 0 \\ 0 & 0 & 0 & \beta_{55} & 0 \\ 0 & 0 & 0 & 0 & \beta_{66} \end{bmatrix} \begin{Bmatrix} \sigma_x \\ \sigma_y \\ \gamma_{yz} \\ \gamma_{xz} \\ \gamma_{xy} \end{Bmatrix}, \qquad [C.5]$$

where,

$$\varepsilon_x^o = \frac{a_{13}}{a_{33}}(e_o + \kappa_z y) \; ; \quad \varepsilon_y^o = \frac{a_{23}}{a_{33}}(e_o + \kappa_z y) \quad ,$$

$$\gamma_{yz}^o = \frac{\kappa_{xz}}{2} x \; ; \quad \gamma_{xz}^o = -\frac{\kappa_{xz}}{2} y \quad ,$$

and,

$$\beta_{ij} = a_{ij} - \frac{a_{i3}\, a_{j3}}{a_{33}} \quad , \qquad i,j = 1,2,4,5,6 \quad .$$

Notice that $\vec{E}$ and $\vec{\varepsilon}_o$ are modified by condensing σ_z out (i.e., the reduced compliance form). In inverted form eq. C.5 will be referred to by,

$$\vec{\sigma}_x = [Q]\, \vec{\bar{\varepsilon}}_x \quad , \qquad [C.6]$$

where, $[Q] = [\beta]^{-1}$

Considering eqs. C.1 and C.5 it may be concluded that the problem associated with U(x,y) and V(x,y) is decoupled from the problem which involves W(x,y). In addition, since U, V, and W are functions which depend on x and y alone, only a two-dimensional finite-element model is required. Considering eqs. C.3, C.5 and C.6 the total potential energy for a typical element of thickness t^e in the z direction becomes,

$$\Pi_p^e = \frac{t^e}{2}\int_{A^\bullet} \vec{E}^T Q \vec{E}\, dA - t^e \int_{A^\bullet} \vec{E}^T Q \vec{\varepsilon}_o\, dA + \frac{t^e}{2}\int_{A^\bullet} \frac{(e_o + \kappa_z y)^2}{a_{33}}\, dA +$$

$$\frac{t^e}{2}\int_{A^\bullet} \vec{\varepsilon}_o^T Q \vec{\varepsilon}_o\, dA - t^e \int_{S_\sigma^\bullet} U^T t\, dS - t^e \int_{S_\sigma^\bullet} u_o^T t\, dS \quad , \qquad [C.7]$$

where $A^\bullet$ is the element surface area in the x-y plane and $S_\sigma^\bullet$ is the part of the element boundary on which external traction forces are acting. In the displacement formulation finite-element program, the unknown displacement functions, U(x,y), V(x,y), and W(x,y) are approximated using a Lagrangian interpolation functions,

$$U(x,y) = \sum_{i=1}^{n} u_i \psi_i(x,y) \quad , \qquad [C.8.a]$$

$$V(x,y) = \sum_{i=1}^{n} v_i \psi_i(x,y) \quad , \qquad [C.8.b]$$

$$W(x,y) = \sum_{i=1}^{n} w_i \psi_i(x,y) \quad , \qquad [C.8.c]$$

where, u_i, v_i and w_i are the generalized nodal displacements and ψ_i are the two-dimensional Lagrangian interpolation function. The interpolation functions ψ_i assume different forms, depending on the type of element used. In the present investigation two types of element were used; the 8-node rectangular and the 6-node triangular isoparametric elements. The interpolation functions for these elements have the following form;

8-Node Isoparametric Element Interpolation Functions

$$\psi_1(\xi,\eta) = -\frac{1}{4}(1-\xi)(1-\eta)(\xi+\eta+1) \quad , \qquad [C.9.a]$$

$$\psi_2(\xi,\eta) = \frac{1}{4}(1+\xi)(1-\eta)(\xi-\eta-1) \quad , \qquad [C.9.b]$$

$$\psi_3(\xi,\eta) = \frac{1}{4}(1+\xi)(1+\eta)(\xi+\eta-1) \quad , \qquad [C.9.c]$$

$$\psi_4(\xi,\eta) = \frac{1}{4}(1-\xi)(1+\eta)(\eta-\xi-1) \quad , \qquad [C.9.d]$$

$$\psi_5(\xi,\eta) = \frac{1}{2}(1-\xi^2)(1-\eta) \quad , \qquad [C.9.e]$$

$$\psi_6(\xi,\eta) = \frac{1}{2}(1-\eta^2)(1+\xi) \quad , \qquad [C.9.f]$$

$$\psi_7(\xi,\eta) = \frac{1}{2}(1-\xi^2)(1+\eta) \quad , \qquad [C.9.g]$$

$$\psi_8(\xi,\eta) = \frac{1}{2}(1-\eta^2)(1-\xi) \quad , \qquad [C.9.h]$$

6-Node Isoparametric Element Interpolation Functions

$$\psi_1(\xi,\eta) = (1-\xi-\eta)(1-2\xi-2\eta) \quad , \qquad [C.10.a]$$

$$\psi_2(\xi,\eta) = \xi(2\xi-1) \quad , \qquad [C.10.b]$$

$$\psi_3(\xi,\eta) = \eta(2\eta-1) \quad , \qquad [C.10.c]$$

$$\psi_4(\xi,\eta) = 4\xi(1-\xi-\eta) \quad , \qquad [C.10.d]$$

$$\psi_5(\xi,\eta) = 4\xi\eta \quad , \qquad [C.10.e]$$

$$\psi_6(\xi,\eta) = 4\eta(1-\xi-\eta) \quad , \qquad [C.10.f]$$

where the elements nodal numbering and natural coordinates system are shown in Figure C.1. Substitution of eqs. C.8 into eq. C.4.b leads to

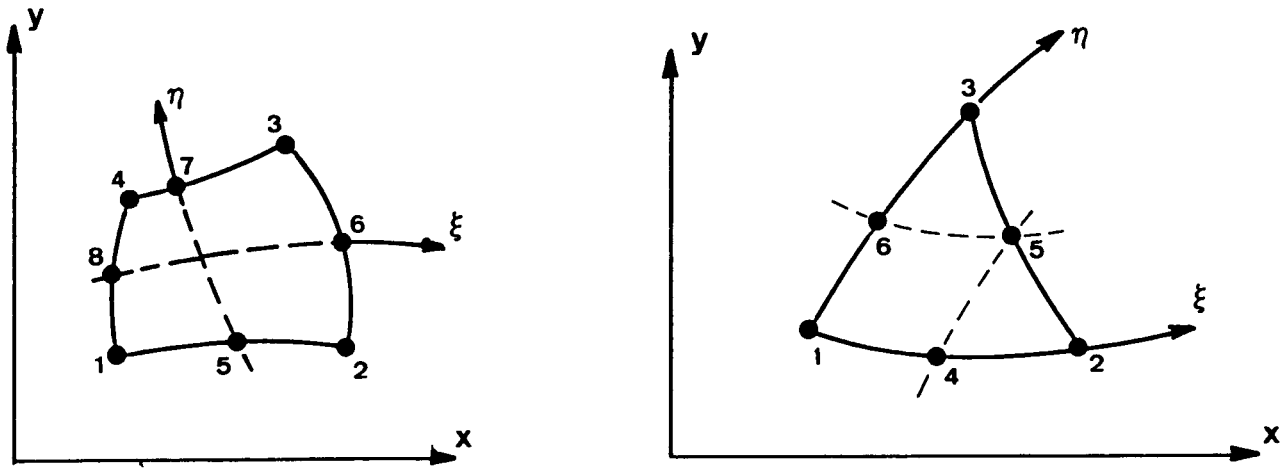

(a) 8-node rectangular element

(b) 6-node triangular element

Figure C.1. Two-Dimensional Isoparametric Elements Coordinates System.

$$\vec{E} = \mathbf{B}\,\mathbf{q} \quad , \qquad [C.11]$$

where,

$$\mathbf{q} = [u_i \quad v_i \quad w_i] \quad , \quad i = 1,2,\ldots,n$$

are the nodal displacements. The matrix **B** is given by,

$$\mathbf{B} = [B_1 \quad B_2 \quad \ldots \quad B_n] \quad , \qquad [C.12]$$

where,

$$B_i = \begin{bmatrix} \frac{\partial \psi_i}{\partial x} & 0 & 0 \\ 0 & \frac{\partial \psi_i}{\partial y} & 0 \\ 0 & 0 & \frac{\partial \psi_i}{\partial y} \\ 0 & 0 & \frac{\partial \psi_i}{\partial x} \\ \frac{\partial \psi_i}{\partial y} & \frac{\partial \psi_i}{\partial x} & 0 \end{bmatrix} \quad , i = 1,2,\ldots,n \quad .$$

Finally, substituting eqs. C.2, C.8, and C.9 into eq. C.7 and minimizing the total potential energy for a typical element,

$$\frac{\partial \Pi_p^e}{\partial q_i} = \left[t^e \int_{A^e} \mathbf{B}^T Q\, \mathbf{B}\, dA \right] \mathbf{q} - t^e \int_{A^e} \mathbf{B}^T Q \vec{\varepsilon}_o\, dA$$

$$- t^e \int_{S_\sigma^e} \Psi^T \mathbf{t}\, dS = 0 \quad . \qquad [C.13]$$

Next if only the solution for U and V are considered, the above integral equations may be cast into a set of simultaneous equations in a matrix form

$$\begin{bmatrix} k^{11} & k^{12} \\ k^{21} & k^{22} \end{bmatrix} \mathbf{q} = \begin{Bmatrix} F^1 \\ F^2 \end{Bmatrix} , \qquad [C.14.a]$$

or in the more common form,

$$[k]\,\mathbf{q} \;=\; \mathbf{F} \quad . \qquad [C.14.b]$$

The components of the stiffness matrix, [k] and force vector, **F** are given as follows:

$$k_{ij}^{11} \;=\; t^e \int_{A^e} \left[Q_{11} \frac{\partial \psi_i}{\partial x} \frac{\partial \psi_j}{\partial x} \;+\; Q_{66} \frac{\partial \psi_i}{\partial y} \frac{\partial \psi_j}{\partial y} \right] dx\, dy \quad , \qquad [C.15.a]$$

$$k_{ij}^{12} \;=\; k_{ij}^{21} \;=\; t^e \int_{A^e} \left[Q_{12} \frac{\partial \psi_i}{\partial x} \frac{\partial \psi_j}{\partial y} \;+\; Q_{66} \frac{\partial \psi_i}{\partial y} \frac{\partial \psi_j}{\partial x} \right] dx\, dy \quad , \qquad [C.15.b]$$

$$k_{ij}^{22} \;=\; t^e \int_{A^e} \left[Q_{66} \frac{\partial \psi_i}{\partial x} \frac{\partial \psi_j}{\partial x} \;+\; Q_{22} \frac{\partial \psi_i}{\partial y} \frac{\partial \psi_j}{\partial y} \right] dx\, dy \quad , \qquad [C.15.c]$$

$$F_i^1 \;=\; t^e \int_{A^e} \frac{(e_o \;+\; \kappa_z\, y)}{a_{33}} \left[Q_{11}\, a_{13} \;+\; Q_{12}\, a_{23} \right] \frac{\partial \psi_i}{\partial x}\, dx\, dy \qquad [C.15.d]$$

$$+ \;\; t^e \int_{S_\sigma^e} \psi_i\, t_x\, ds \quad ,$$

$$F_i^2 \;=\; t^e \int_{A^e} \frac{(e_o \;+\; \kappa_z\, y)}{a_{33}} \left[Q_{12}\, a_{13} \;+\; Q_{22}\, a_{23} \right] \frac{\partial \psi_i}{\partial y}\, dx\, dy \qquad [C.15.e]$$

$$+ \;\; t^e \int_{S_\sigma^e} \psi_i\, t_y\, ds \quad , \qquad i,j = 1,2,\ldots,n \quad .$$

Using the interpolation functions, eqs. C.9 and C.10, the elements stiffness matrices and force vectors in eqs. C.15.a through C.15.e can be evaluated numerically. Once [k] and **F** are known the solution for **q** can be obtained.

C.2 EAL Finite-Element Program

The EAL finite-element program is based on hybrid element formulation. In the displacement formulation finite-element approach, the element stiffness matrices are derived using the principle of minimum potential energy. Whereas, in the hybrid finite-element formulation the element stiffness matrix are derived using the complementary energy principle given by,

$$\Pi_c = \frac{1}{2} \int_V \vec{\sigma}^T C \vec{\sigma} \, dV - \int_A \mathbf{u}^T \mathbf{t} \, dA \quad , \qquad [C.16]$$

where the work done by the body forces were neglected. In eq. C.16, C is the material stiffness matrix, **u** is the displacement vector, and **t** is the surface traction vector. In the hybrid element formulation the stresses are written in terms of generalized stress coefficients,

$$\vec{\sigma} = P \mathbf{b} \quad , \qquad [C.17]$$

where,

$$\mathbf{b}^T = [b_1 \;\; b_2 \;\; \ldots \;\; b_n] \quad ,$$

and P is a matrix which depends on position and is chosen in such a way so that $\vec{\sigma}$ satisfies the stress equilibrium equations identically. Using eq. C.17 the body internal strain energy becomes,

$$\Phi = \frac{1}{2} \mathbf{b}^T \{ \int_V P^T C P \, dV \} \mathbf{b} \quad . \qquad [C.18]$$

Next the displacements are written in terms of the element generalized nodal displacements,

$$\mathbf{u} = L \mathbf{q} \quad , \qquad [C.19]$$

where L is a function of position and insures inter-element compatibility. In addition, the surface tractions may be related to the body stresses by,

$$\mathbf{t} = R\mathbf{b} \quad , \qquad [C.20]$$

where R is a function of the boundary position. Upon substitution of eqs. C.18 through C.20 into eq. C.16 the total complementary energy becomes,

$$\Pi_c = \frac{1}{2}\mathbf{b}^T H \mathbf{b} - \mathbf{b}^T T \mathbf{q} \quad , \qquad [C.21]$$

where,

$$H = \int_V P^T C P \, dV \quad ,$$

$$T = \int_A R^T L \, dA \quad .$$

The next step involves the minimization of Π_c with respect to the generalized stress coefficients, b_i,

$$\frac{\partial \Pi_c}{\partial b_i} = 0 \quad ,$$

leading to a relation between **b** and **q**,

$$\mathbf{b} = H^{-1} T \mathbf{q} \quad .$$

From which the element stiffness matrix is calculated,

$$[k_c] = T^T H^{-1} T \quad .$$

The solution to the finite-element problem is obtained in the standard form, i.e.,

$$[k]\,\mathbf{q} = \mathbf{F} \quad ,$$

except that $[k]$ is replaced by $[k_c]$. If $[\bar{k}]$ is the stiffness matrix of perfectly conforming elements, than $[k_c]$ approaches $[\bar{k}]$ from the soft side. Whereas, $[k]$, as derived from the displacement formulation finite-element, approaches $[\bar{k}]$ from the stiff side.

EAL - E43 and E33 Elements

The E43 and E33 are the 4-node rectangular and 3-node triangular plate elements. Each node of these elements has 5 degrees of freedom (dof) consisting of two rotation and three displacement components. The element formulation is based on the assumed stress resultant polynomials which satisfy the following plate equilibrium equations;

$$\frac{\partial Q_x}{\partial x} + \frac{\partial Q_y}{\partial y} + q = 0 \quad ,$$

$$\frac{\partial M_x}{\partial x} - \frac{\partial M_{xy}}{\partial y} = Q_x \quad ,$$

$$-\frac{\partial M_{xy}}{\partial x} + \frac{\partial M_y}{\partial y} = Q_y \quad ,$$

$$\frac{\partial^2 M_x}{\partial x^2} + 2\frac{\partial^2 M_{xy}}{\partial x \partial y} + \frac{\partial^2 M_y}{\partial y^2} + q = 0 \quad ,$$

where q is applied uniform transverse load. All symbol and coordinate nomenclature are those common to the theory of plates. The stress resultant polynomials which satisfy the above equations have the following form;

E33 Element

$$N_x = b_3 \ , \quad N_y = b_2 \ , \quad N_{xy} = b_1 \ ,$$

$$\begin{Bmatrix} M_x \\ M_y \\ M_{xy} \\ Q_x \\ Q_y \end{Bmatrix} = \begin{bmatrix} b_4 & b_9 & b_7 \\ b_5 & b_8 & b_{10} \\ b_6 & 0 & 0 \\ b_9 & 0 & 0 \\ b_{10} & 0 & 0 \end{bmatrix} \begin{Bmatrix} 1 \\ x \\ y \end{Bmatrix} .$$

E44 Element

$$N_x = b_3 + b_4 y \ , \quad N_y = b_2 + b_5 x \ , \quad N_{xy} = b_1 \ ,$$

$$\begin{Bmatrix} M_x \\ M_y \\ M_{xy} \\ Q_x \\ Q_y \end{Bmatrix} = \begin{bmatrix} b_5 & b_{11} & b_9 & b_{15} \\ b_7 & b_{10} & b_{12} & b_{16} \\ b_8 & b_{14} & b_{13} & b_{17} \\ b_{11} - b_{13} & -b_{17} & b_{15} & 0 \\ b_{12} - b_{14} & b_{16} & -b_{17} & 0 \end{bmatrix} \begin{Bmatrix} 1 \\ x \\ y \\ xy \end{Bmatrix} .$$

where,

$$b_{17} = \frac{p}{2} \ .$$

The plate constitutive relations for composite materials are given by,

$$\begin{Bmatrix} \underline{N} \\ \underline{M} \end{Bmatrix} = \left[\begin{array}{c|c} A & B \\ \hline B & D \end{array}\right] \begin{Bmatrix} \underline{\epsilon} \\ \underline{\kappa} \end{Bmatrix} .$$

EAL - S61 and S81 Solid Elements

The S61 and S81 are 6-nodes, pentahedron, and 8-nodes, hexahedron, solid elements. Each node of these elements has 3 degrees of freedom, u, v, and w. For these elements the assumed stress polynomials have the following form;

$$\sigma_x = b_1 + b_7 y + b_8 z + b_{16} yz \quad ,$$

$$\sigma_y = b_2 + b_9 x + b_{10} z + b_{17} xz \quad ,$$

$$\sigma_z = b_3 + b_{11} x + b_{12} y + b_{18} xy \quad ,$$

$$\tau_{yz} = b_5 + b_{14} x \quad ,$$

$$\tau_{xz} = b_6 + b_{15} y \quad ,$$

$$\tau_{xy} = b_4 + b_{13} z \quad ,$$

These set of assumed stress polynomials satisfy the stress equilibrium equations three-dimensional elastic body. The element constitutive law assumes the most general anisotropic form,

$$\vec{\varepsilon}_x = [\bar{S}]\vec{\sigma}_x \quad ,$$

where $[\bar{S}]$ is a fully populated matrix.

Appendix D. Material Properties and Eigenvalue Data

The material properties used in the current investigation are representative of materials used by the aircraft industry. Though not representing any particular material, they are used here to demonstrate the analytical model. The lamina principal material properties are,

$$E_1 = E_2 = 2.1 \text{ Msi} , \quad E_3 = 20.0 \text{ Msi} ,$$

$$G_{31} = G_{32} = G_{12} = 0.85 \text{ Msi} ,$$

$$\nu_{31} = \nu_{32} = \nu_{12} = 0.21 ,$$

with the 1, 2, and 3 being the transverse, thickness, and fiber-direction respectively. The integrated laminate material properties are obtained by smearing the individual lamina properties through the thickness of the laminate. Table D.1 lists the engineering constants for the different laminates used in the investigation. In the study, two sets of skin-stiffener material system combinations were used. In both of these combinations the skin laminate was always main-

Table D.1. Laminate Material Properties.

Laminate	E_x (Msi)	E_y (Msi)	E_z (Msi)	G_{yz} (Msi)	G_{xz} (Msi)	G_{xy} (Msi)	ν_{zy}	ν_{zx}	ν_{xy}
Flange - $(\pm 45/0/90)_s$	8.05	2.16	8.05	0.85	3.09	0.85	0.164	0.303	0.164
Flange - $(\pm 45/0/90_2/0/\pm 45)_s$	8.05	2.16	8.05	0.85	3.09	0.85	0.164	0.303	0.164
Flange - $(\pm 45/0_2)_s$	3.83	2.15	11.71	0.85	3.09	0.85	0.107	0.614	0.176
Flange - $(\pm 45/0_4/\pm 45)_s$	3.83	2.15	11.71	0.85	3.09	0.85	0.107	0.614	0.176
Skin - $(\pm 45/90_2)_s$	11.71	2.15	3.83	0.85	3.09	0.85	0.176	0.201	0.107

tained at $(\pm 45/90_2)_s$. The stiffener flange laminate layup varied. The following four stiffener flange laminates were used: 1. $(\pm 45/0/90)_s$; 2. $(\pm 45/0/90_2/0/ \pm 45)_s$; 3. $(\pm 45/0_2)_s$; and 4. $(\pm 45/0_4/ \pm 45)_s$. In the stiffener parametric study context, laminate 1 is the baseline stiffener flange configuration, laminate 2 is the "thick flange", laminate 3 is the "soft flange", and laminate 4 is the "thick & soft flange" configuration. From Table D.1 it is clear that the combination of the skin laminate with either the first or the second flange laminate (i.e., laminate 1 or 2) will produce the same set of eigenvalues for a given flange termination angle. This material system combination is referred to as combination no. 1. The same is true for skin-stiffener material combination which use flange laminates 3 or 4. This material system combination is referred to as combination no. 2. The eigenvalues for these two material system combinations and for three flange termination angles are given in Table D.2 and D.3, respectively.

Finally, the adhesive layer material properties used to produce the results in section 2.6 were taken from Delale and Egdogan[1] and are listed below;

$$E = 0.445 \text{ Msi} \quad ,$$

$$G = 0.165 \text{ Msi} \quad .$$

---

[1] Delale, F., Erdogan, F., and Aydinoglu, M.N., " Stresses in adhesively bonded joints: A closed-form solution," J. of Composite Materials , 15, (1981) p. 249.

Table D.2. The First 20 Eigenvalues for Material System Combination no. 1.

Eigenvalue	90 ° Flange		45 ° Flange		15 ° Flange	
	Re(λ)	Im(λ)	Re(λ)	Im(λ)	Re(λ)	Im(λ)
1	-0.43635	0.00000	-0.33411	0.00000	-0.18647	0.00000
2	-0.09732	0.00000	0.20747	0.00000	0.58520	0.00000
3	0.61127	0.26408	0.88915	0.23501	1.03013	0.00000
4	1.23723	0.38177	1.68653	0.37310	1.28906	0.00000
5	1.94566	0.45946	2.39937	0.50504	2.03561	0.16068
6	2.58078	0.73989	3.12576	0.50552	2.93357	0.22638
7	3.07138	0.61304	3.98603	0.52509	3.84062	0.27325
8	3.98901	0.59118	4.95811	0.61955	4.73755	0.32159
9	4.27070	1.47640	5.09652	1.38249	5.60553	0.36268
10	5.00272	0.60228	6.01345	0.60947	6.45256	0.36802
11	5.87719	2.27038	7.00237	0.59576	7.31696	0.34336
12	5.99945	0.60041	7.73200	2.81970	8.20417	0.32526
13	7.00012	0.60094	7.99798	0.60051	9.09758	0.32891
14	7.48417	3.06507	9.00007	0.60162	9.98873	0.35149
15	7.99998	0.60083	10.00025	0.60075	10.88040	0.38847
16	9.00001	0.60085	10.37200	4.25700	11.77590	0.44442
17	9.09114	3.85980	11.00000	0.60100	12.66080	0.53195
18	10.00000	0.60085	11.99993	0.60077	13.47630	0.63359
19	10.69810	4.65425	12.99998	0.60088	14.24980	0.61996
20	11.00000	0.60085	13.00001	0.60085	15.12560	0.55368

Table D.3. The First 20 Eigenvalues for Material System Combination no. 2.

Eigenvalue	90 ° Flange		45 ° Flange		15 ° Flange	
	Re(λ)	Im(λ)	Re(λ)	Im(λ)	Re(λ)	Im(λ)
1	-0.42024	0.00000	-0.27723	0.00000	-0.11114	0.00000
2	-0.07317	0.00000	0.22778	0.00000	0.73478	0.00000
3	0.63623	0.24273	0.91197	0.18021	1.01358	0.00000
4	1.21914	0.32693	1.78361	0.29720	1.46261	0.00000
5	1.98135	0.33022	2.50825	0.55798	2.08113	0.10420
6	2.69141	0.76485	3.10038	0.43477	2.97851	0.17005
7	3.02855	0.43438	4.10158	0.35625	3.91688	0.19526
8	3.99588	0.38796	4.97308	0.38015	4.87046	0.22625
9	4.51536	1.39626	5.74319	1.54774	5.82954	0.27332
10	5.00189	0.40167	5.99659	0.41568	6.78840	0.35112
11	5.99948	0.39660	7.01177	0.39736	7.71570	0.51128
12	6.30526	2.01340	8.00106	0.39226	8.36755	0.62900
13	7.00021	0.39820	8.94969	2.70220	9.18464	0.43118
14	7.99995	0.39763	8.99789	0.39820	10.13980	0.34095
15	8.09300	2.62978	10.00080	0.39917	11.10160	0.30039
16	9.00004	0.39781	11.00080	0.39739	12.06210	0.28511
17	9.88043	3.24169	11.99970	0.39745	13.01910	0.28893
18	10.00000	0.39774	12.16796	3.87703	13.96960	0.31197
19	11.00000	0.39776	12.99989	0.39795	14.90740	0.35938
20	11.66780	3.86264	14.00010	0.39784	15.81540	0.44262

BIBLIOGRAPHIC DATA SHEET	1. Report No. CCMS-87-17; VPI-E-87-32	2.	3. Recipient's Accession No.

4. Title and Subtitle

CALCULATION OF SKIN-STIFFENER INTERFACE STRESSES IN STIFFENED COMPOSITE PANELS

5. Report Date December 1987

6.

7. Author(s)

D. Cohen and M. W. Hyer

8. Performing Organization Rept. No. VPI-E-87-32

9. Performing Organization Name and Address

Virginia Polytechnic Institute & State University
Dept of Engineering Science & Mechanics
Blacksburg, Virginia 24061

10. Project/Task/Work Unit No.

11. Contract/Grant No. NAG 1-343

12. Sponsoring Organization Name and Address

Structural Mechanics Branch
National Aeronautics & Space Administration
Langley Research Center
Hampton, Virginia 23665

13. Type of Report & Period Covered

14.

15. Supplementary Notes

16. Abstracts

A method for computing the skin-stiffener interface stresses in stiffened composite panels is developed. Both geometrically linear and nonlinear analyses are considered. Particular attention is given to the flange termination region where stresses are expected to exhibit unbounded characteristics. The method is based on a finite-element analysis and an elasticity solution. The finite-element analysis is standard, while the elasticity solution is based on an eigenvalue expansion of the stress functions. The eigenvalue expansion is assumed to be valid in the local flange termination region and is coupled with the finite-element analysis using collocation of stresses on the local region boundaries. Accuracy and convergence of the local elasticity solution are assessed using a geometrically linear analysis. Using this analysis procedure, the influence of geometric nonlinearities and stiffener parameters on the skin-stiffener interface stresses is evaluated.

17. Key Words and Document Analysis. 17a. Descriptors

geometrically nonlinear, peeling stress, shearing stress, flange termination region, singular stresses, eigenvalue expansion, stress functions, stiffened panels

17b. Identifiers/Open-Ended Terms

17c. COSATI Field/Group

18. Availability Statement	19. Security Class (This Report)	21. No. of Pages
unlimited	UNCLASSIFIED	191
	20. Security Class (This Page) UNCLASSIFIED	22. Price

VIRGINIA TECH CENTER FOR COMPOSITE MATERIALS AND STRUCTURES

The Center for Composite Materials and Structures is a coordinating organization for research and educational activity at Virginia Tech. The Center was formed in 1982 to encourage and promote continued advances in composite materials and composite structures. Those advances will be made from the base of individual accomplishments of the forty members who represent ten different departments in two colleges.

The Center functions through an Administrative Board which is elected yearly and a Director who is elected for a three-year term. The general purposes of the Center include:

- collection and dissemination of information about composites activities at Virginia Tech,
- contact point for other organizations and individuals,
- mechanism for collective educational and research pursuits,
- forum and agency for internal interactions at Virginia Tech.

The Center for Composite Materials and Structures is supported by a vigorous program of activity at Virginia Tech that has developed since 1963. Research expenditures for investigation of composite materials and structures total well over seven million dollars with yearly expenditures presently approximating two million dollars.

Research is conducted in a wide variety of areas including design and analysis of composite materials and composite structures, chemistry of materials and surfaces, characterization of material properties, development of new material systems, and relations between damage and response of composites. Extensive laboratories are available for mechanical testing, nondestructive testing and evaluation, stress analysis, polymer synthesis and characterization, material surface characterization, component fabrication, and other specialties.

Educational activities include eight formal courses offered at the undergraduate and graduate levels dealing with the physics, chemistry, mechanics, and design of composite materials and structures. As of 1984, some 43 Doctoral and 53 Master's students have completed graduate programs and several hundred Bachelor-level students have been trained in various aspects of composite materials and structures. A significant number of graduates are now active in industry and government.

Various Center faculty are internationally recognized for their leadership in composite materials and composite structures through books, lectures, workshops, professional society activities, and research papers.

MEMBERS OF THE CENTER

Aerospace and Ocean Engineering
- Raphael T. Haftka
- Eric R. Johnson
- Rakesh K. Kapania

Chemical Engineering
- Donald G. Baird

Chemistry
- John G. Dillard
- James E. McGrath
- Thomas C. Ward
- James P. Wightman

Civil Engineering
- R. M. Barker

Electrical Engineering
- Ioannis M. Besieris
- Richard O. Claus

Engineering Science and Mechanics
- Hal F. Brinson
- Robert Czarnek
- David Dillard
- Norman E. Dowling
- John C. Duke, Jr.
- Daniel Frederick
- O. Hayden Griffin, Jr.
- Zafer Gurdal
- Robert A. Heller
- Edmund G. Henneke, II
- Michael W. Hyer
- Robert M. Jones
- Liviu Librescu
- Alfred C. Loos
- Don H. Morris
- John Morton
- Ali H. Nayfeh
- Marek Pindera
- Daniel Post
- J. N. Reddy
- Kenneth L. Reifsnider
- C. W. Smith
- Wayne W. Stinchcomb
- Surot Thangjitham

Industrial Engineering and Operations Research
- Joel A. Nachlas

Materials Engineering
- D. P. H. Hasselman
- Robert E. Swanson

Mathematics
- Werner E. Kohler

Mechanical Engineering
- Charles E. Knight
- John B. Kosmatka
- J. Robert Mahan
- Craig A. Rogers
- Curtis H. Stern

Inquiries should be directed to:

Center for Composite Materials and Structures
College of Engineering
Virginia Tech
Blacksburg, VA 24061
Phone: (703) 961-4969

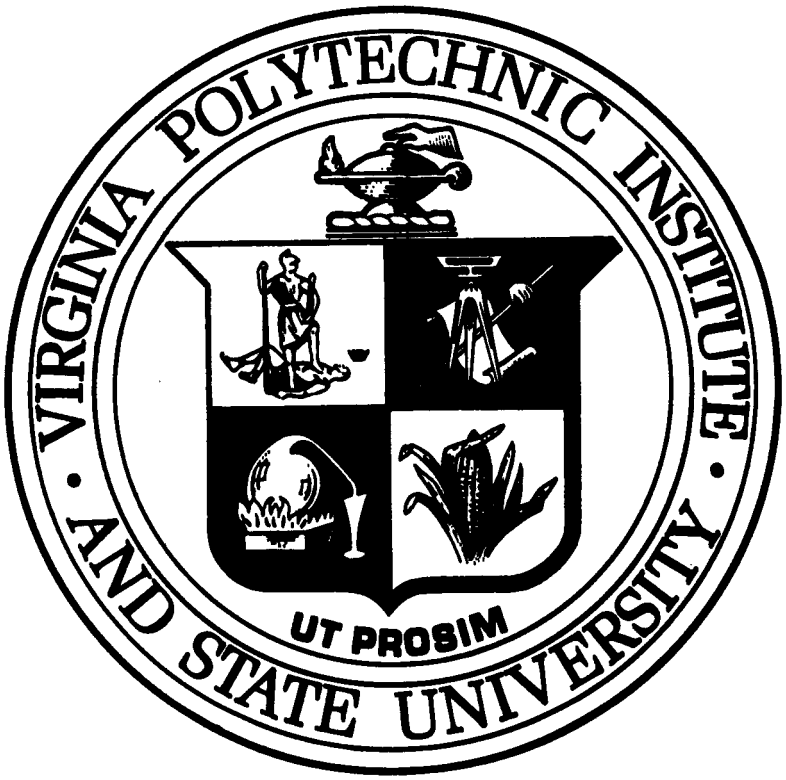
VIRGINIA POLYTECHNIC INSTITUTE
AND STATE UNIVERSITY
UT PROSIM